THERMOMECHANICAL MODELING AND BRITTLE INTERFACE CHARACTERIZATION FOR ON-CHIP FLUIDIC COOLER IN MICROELECTRONIC PACKAGES

A Dissertation
Presented to
The Academic Faculty

by

David Casey Woodrum

In Partial Fulfillment
of the Requirements for the Degree
Doctor of Philosophy in the
George W. Woodruff School of Mechanical Engineering

Georgia Institute of Technology
May 2020

THERMOMECHANICAL MODELING AND BRITTLE INTERFACE CHARACTERIZATION FOR ON-CHIP FLUIDIC COOLER IN MICROELECTRONIC PACKAGES

Approved by:

Dr. Suresh K. Sitaraman, Advisor
School of Mechanical Engineering
Georgia Institute of Technology

Dr. Peter A. Kottke
School of Mechanical Engineering
Georgia Institute of Technology

Dr. Muhannad S. Bakir
School of Electrical and Computer Engineering *Georgia Institute of Technology*

Dr. Shuman Xia
School of Mechanical Engineering
Georgia Institute of Technology

Dr. Yogendra K. Joshi
School of Mechanical Engineering
Georgia Institute of Technology

Dr. Ross K. Wilcoxon
Rockwell Collins-United Technologies Corporation

Date Approved: December 6, 2019

To my Friends, Family, and Mentors

ACKNOWLEDGEMENTS

During my studies at Georgia Tech, I have grown and developed through experiences in many disciplines, not all of which are related to my research endeavors. I am thankful to many for the opportunities I have been able to take advantage of at Georgia Tech.

My successful pursuit of higher education has come in large part from the great efforts of my parents, Tom and Jody Woodrum, and I would like to thank them for all the positive support they have provided. I cannot ask for better parents or for better mentors in life.

I would also like to thank my advisor Dr. Suresh Sitaraman. I am very grateful I am for his sustained guidance, patience, and flexibility during my studies. I greatly appreciate Dr. Sitaraman's ability to treat each and every student as a special individual on a unique path, while encouraging growth through goal-oriented research.

I thank Dr. Muhannad Bakir, Dr. Yogendra Joshi, Dr. Peter Kottke, Dr. Shuman Xia, and Dr. Ross Wilcoxon for serving on my committee. Their input has aided me in improving the quality of my work and helped me to grow as a researcher. I would also like to acknowledge the Defense Advanced Research Projects Agency for financial support of projects related to my research, particularly both the ICECool Fundamentals and Applications programs.

To my friends, I am also extremely thankful for the experiences and memories I have made during my stay at Georgia Tech while living in Atlanta. I appreciate all the memorable distractions and the valuable support over the years.

TABLE OF CONTENTS

LIST OF TABLES

LIST OF FIGURES

LIST OF SYMBOLS AND ABBREVIATIONS

TSV	Through-silicon via
FPGA	Field Programmable Gate Array
SEM	Scanning Electron Microscope
E	Modulus of Elasticity
G	Energy Release Rate
CPC	Chevron Pressure Cavity
W_e	Work done (External)
U	Total Energy
p	Pressure
V	Volume
σ	Stress
ε	Strain
ν	Poisson's ratio
Δ	Delta (incremental change)

SUMMARY

The overall goal of this work is to develop a reliable microfluidic architecture for high heat-flux microelectronic applications by experimentally characterizing glass-silicon interface. This is achieved through an innovative technique and by employing numerical simulations and analytical models to ensure that the interface will not crack or delaminate under given pressure and temperature conditions. This work also aims to examine microfluidic architectures of different generations and designs to achieve its goal. Thus, the first objective of this work is to perform a thermomechanical analysis of a high-pressure, two-phase microfluidic cooler using numerical models. The next objective is to develop a reliable microfluidic architecture with an appropriate pin-fin configuration. This requires characterizing and understanding the failure modes through analysis of various generations of prototype thermal test vehicles for high-pressure two-phase cooling. These models underscored the significance of understanding the failure mode of the silicon-glass interface and provide context for the third and fourth objectives. The third objective involves analyzing the mechanical behavior of the silicon-glass interface through using pin fin optimization models to design thermal test vehicles as well as experimental pressure test devices. These models and resulting devices work in tandem with the experimental methodology of objective fourth. The fourth and final objective is to develop an innovative experimental test technique for evaluating the mechanical performance of a silicon-glass interface. By using a pressurized cavity to apply load on the silicon-glass interface, this test more accurately mimics the conditions of a high-pressure microfluidic cooler than existing test techniques for evaluating brittle interfaces.

CHAPTER 1. INTRODUCTION

As power demands for microelectronic devices continue to rise, new techniques for heat dissipation require innovative fabrication solutions such as on-chip cooling methods. The mechanical reliability of these high-powered, high-pressure systems is particularly sensitive to the interfacial strengths within the microelectronic architectures. Ongoing cutting-edge research focuses on on-chip cooling methodologies and involves utilizing thermal test vehicles with high-pressure coolant pumped through microchannels to dissipate heat fluxes exceeding 1 kW/cm^2. In one method the microchannels are etched directly into a silicon wafer and then capped by a second wafer possibly made of silicon or, alternatively, Pyrex glass. When fluid flows through the flow channels of the system, internal pressures can exceed 2000 kPa. These high pressures are required to sustain saturation conditions for two-phase flow of high-pressure coolants, such as R134a, within microchannels. The use of two-phase convective cooling offers the advantage of exploiting extremely high heat transfer coefficient as well as coolant latent and sensible heat to remove the target heat flux rate. Overall system failure due to cracking of the brittle materials is of particular interest given the potential for catastrophic crack propagation at these pressure levels.

This work identifies mechanical concerns in on-chip microfluidic coolers, provides a methodology for developing reliable high-pressure cooler designs, and presents a novel Chevron Pressure Cavity test technique for characterizing critical material interfaces in microfluidic architectures.

Ongoing challenges for microfluidic device engineering exist in all related disciplines: thermal, fluidic, electrical, fabrication, mechanical, and materials. The included objectives of this work focus first on a high-powered theoretical microfluidic cooler. The next objective outlines an approach taken to characterize the mechanical performance of various generations of prototype thermal test vehicles for high-pressure two-phase cooling. These generations are shown in Figure 1.1. The models of objectives two and three underscore the significance of understanding the failure mode of the silicon-glass interface providing context for the fourth objectives. These models aid in developing test devices for the experimental test setup of Objective 4. By using a pressurized cavity to apply load on the silicon-glass interface, this test more accurately mimics the working conditions of a high-pressure microfluidic cooler than existing test techniques for evaluating brittle interfaces. This test technique, the Chevron Pressure Cavity test, utilizes devices similar to those in Figure 1.2. By satisfying these four objectives, the work provides methods for testing and modeling that characterize the mechanical behavior and reliability of the high-pressure microfluidic system.

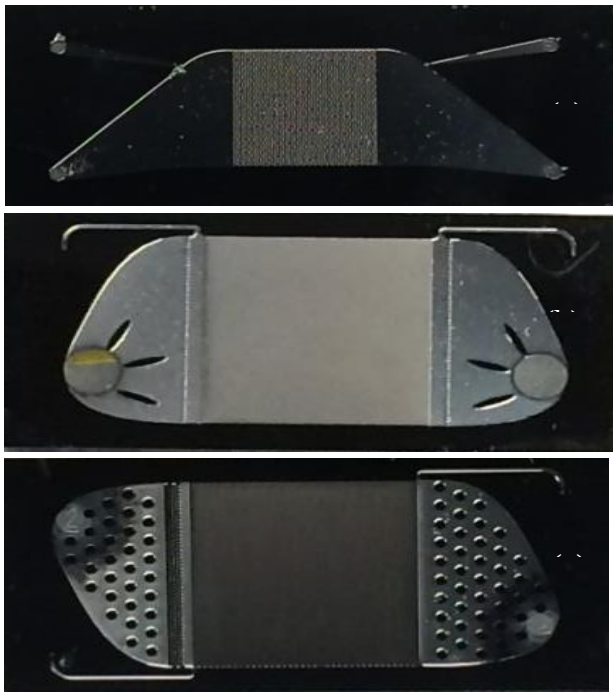

Figure 1.1 – Generation 1, generation 2, and generation 3 (top to bottom)

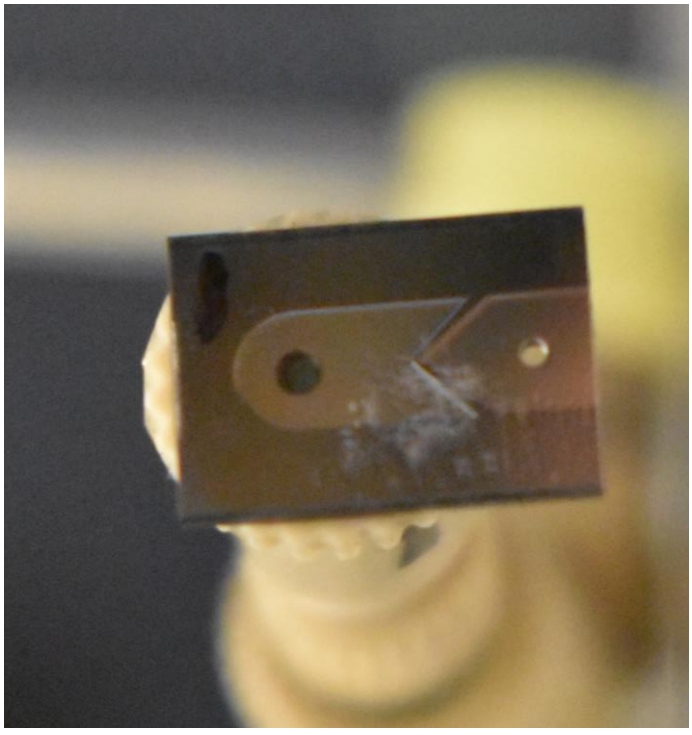

Figure 1.2 – Example device used in novel Chevron Pressure Cavity test

CHAPTER 2. BACKGROUND AND MOTIVATION

2.1 Motivation and Need for Next Generation Cooling Technologies

New and innovative approaches to heat management are required to meet the requirements for next generation computing machines that have higher heat densities in stacked architectures. A steady increase in performance and stacking of devices resulted in a rapid increase in power usage and power densities for devices from 1970 to the late 2000's, a trend which has continued onward toward 2020 [1-3]. Figure 2.1 illustrates the increase in power and power density over time as well as other metrics for top end devices. With the increased implementation of stacked devices, removing heat from high density locations is an even greater problem than once thought. In a 2017 yearly report for "International Roadmap for Devices and Systems," in affiliation with the Institute of Electrical and Electronics Engineers, many engineers agree that thermal issues in stacked devices are long-term problems for microelectronics devices [2]. Though normally electrical performance dominates the discussion, it is clear that thermal management is a growing area of concern and requires more consideration during all design phases. Future microfluidic cooling designs will require complete and concurrent efforts from electrical, thermal-fluid, and mechanical engineering disciplines.

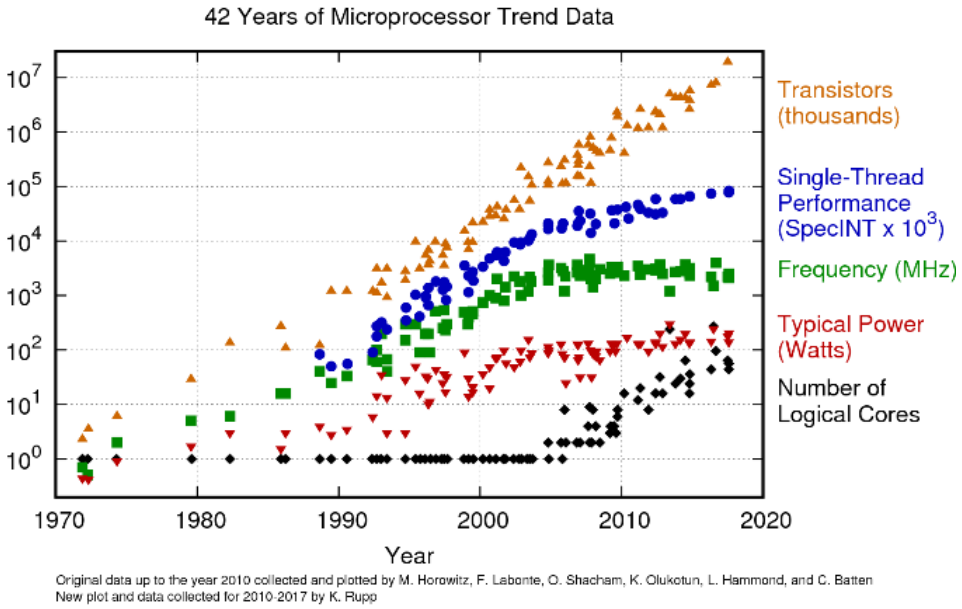

Figure 2.1 – Key metrics for top of the line microprocessors since 1970. Original data up to the year 2010 collected and plotted by M. Horowitz, et. al.; new plot and data collected for 2010-2017 and plotted by K. Rupp [3].

Stacked 3-D and 2.5-D packages are increasing in dominance for many types of system architectures. This presents additional challenges for providing direct targeted cooling solutions that can remove heat from multiple layers in a stack efficiently. Non-uniform system heating can also exacerbate thermal management problems. Figure 2.2 illustrates a possible heat generation map, showing that, while some regions may have relatively benign heat densities, hot spot locations experience significantly higher heat densities. Transitioning from more common cooling apparatuses, such as metal heat sinks and heat pipes, to liquid cooling for high heat fluxes is one likely path for mainstream thermal management, but in the end may be hindered by the cost of implementation. The relative cost comparison shown in Figure 2.3 underscores this additional barrier to widespread adoption of high-end microfluidic cooling solutions [4].

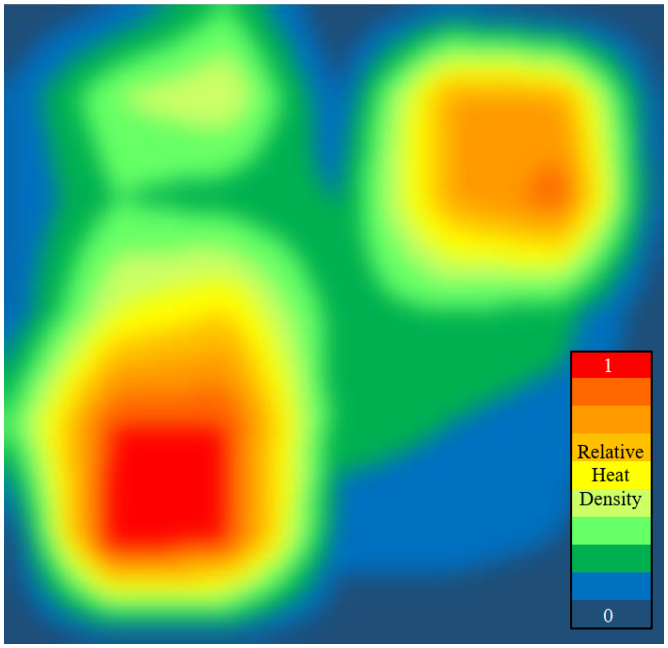

Figure 2.2 – Example non-uniform heat map for microprocessor

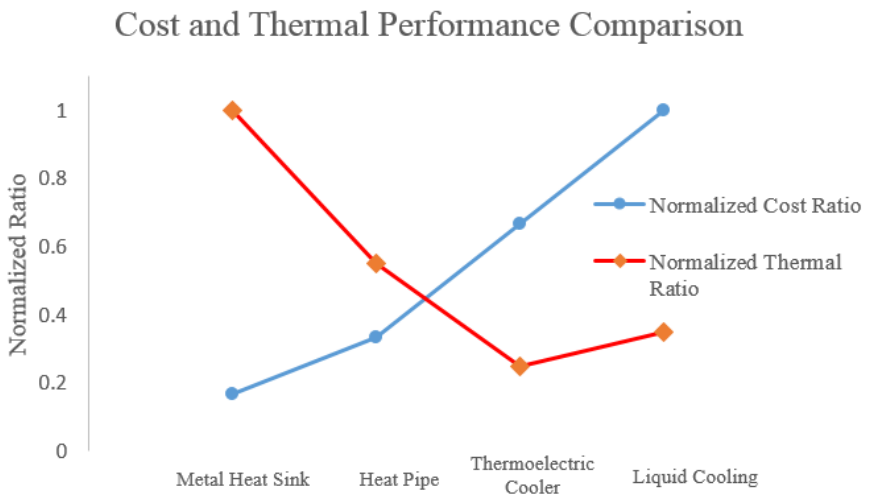

Figure 2.3 – Comparison of cost ratio to thermal resistance ratio for thermal management designs. Original data source: Mahajan, R., Chiu, C., and Chrysler, G. [4].

2.2 Air Cooling versus On-Chip Cooling Architectures

The trend to move away from a basic heat spreader and heat sink is grounded in a few limitations of this design. A basic heat sink, shown in Figure 2.4, suffers from larger distances between heat source locations and heat rejection points relative to aspiring on-chip cooling solutions. Additionally, when restricted to air cooling, heat removal in these designs are limited by the thermal conductivity and specific heat of air.

While designs for pressurized microfluidic coolers vary greatly in architecture, they do tend to share some characteristics since their primary goal is to improve upon the heat removal of existing systems. This results in optimization of the flow space architecture for increased surface area for heat transfer from solid to fluid. Figure 2.5 and Figure 2.6 demonstrate two designs for stacked microfluidic cooling [5]. The first design shows one method in which the fluid flows through the chips that are to be cooled, while the second design allows for fluid flow within the microchannels in the chips as well as through an interposer. A third design in Figure 2.7 further illustrates this stacked architecture as well as details for the interconnections between each chip in the stack [6].

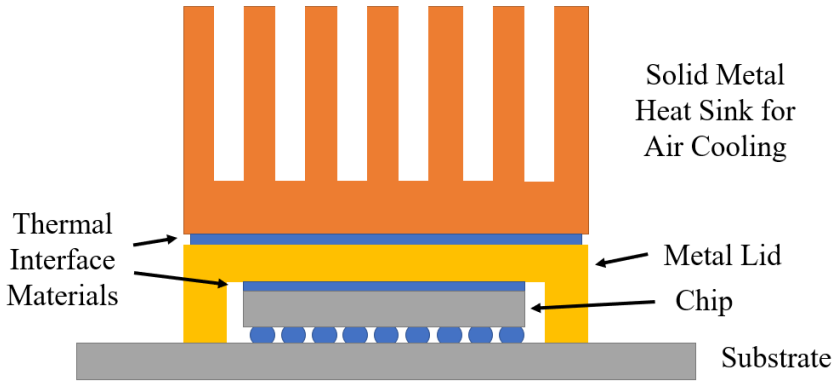

Figure 2.4 – Generic heat sink design for air cooling

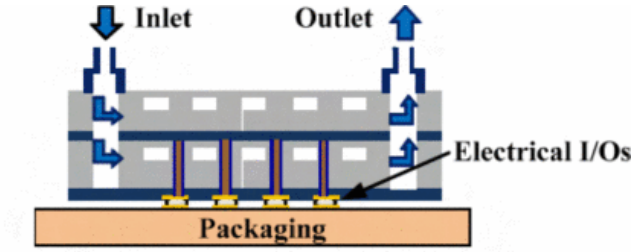

Figure 2.5 – 3-D architecture for on-chip cooling [5]

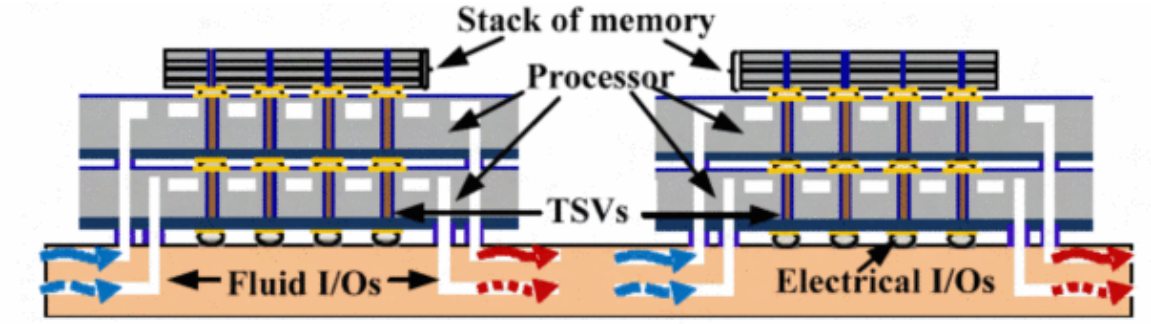

Figure 2.6 – 3-D architecture for microfluidic cooling of memory stacks using an interposer [5]

By implementing embedded cooling or on-chip cooling solutions, the thermal performance of the device improves dramatically. The effective thermal resistance of a basic heat sink includes the resistance of the chip, thermal interface materials, lid spreader, and finned heat sink. Considering the corresponding resistance for an embedded cooling system, the total resistance is reduced to a minimum section of the chip thickness. From a co-design perspective, this improvement does not come without trade-offs of fabrication challenges and cost, but the improvement can be significant enough to offset these costs.

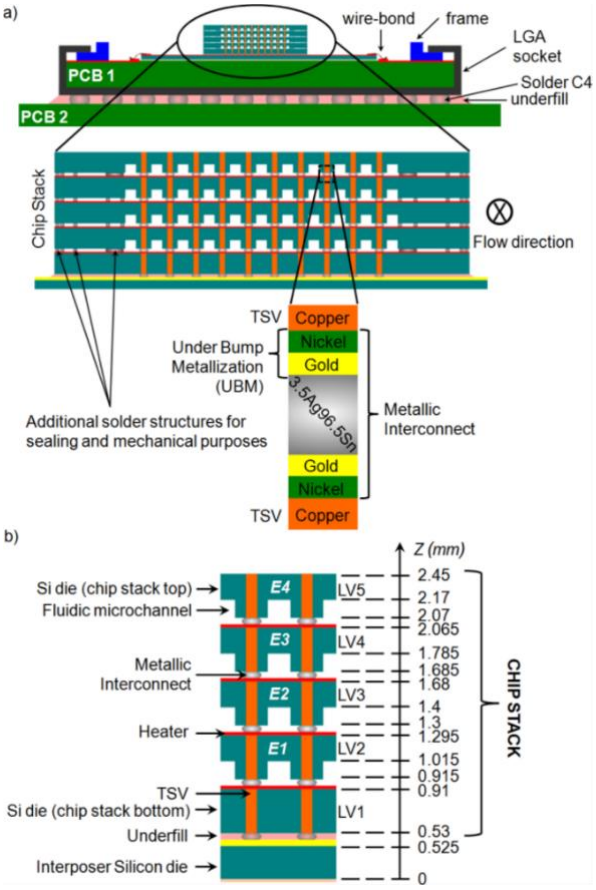

Figure 2.7 – 3-D microfluidic architecture for cooling of multi-chip stack with detail of interconnections [6]

New designs also utilize liquids such as refrigerants or water that provide greater opportunity for heat removal than air. Using a saturated liquid vapor mixture takes this concept one step further by allowing the phase change from liquid to vapor to also provide a heat absorption effect of the two-phase mixture.

2.3 Liquid and Two-Phase Cooling Design Variations

Generally, all design types strive to optimize the flow space architecture for increased surface area for heat transfer. This can be achieved in a number of ways, and each of these design types has advantages and disadvantages.

One such method of forced flow is jet impingement. In this method fluid is forced through a tube-like structure and ejected perpendicularly onto a plate surface, causing a focused heat removal effect. A cross-sectional view of this method is illustrated in Figure 2.8 [7]. The design shown in Figure 2.9 includes many flow ports that eject fluid on the opposing plate face causing a jet impingement effect with enhanced heat removal. While this design can create locally focused removal of heat at desired locations, delivering fluid to the entire device through many ports can be a challenge and may create unexpected, sub-optimal flow patterns. [7, 8]

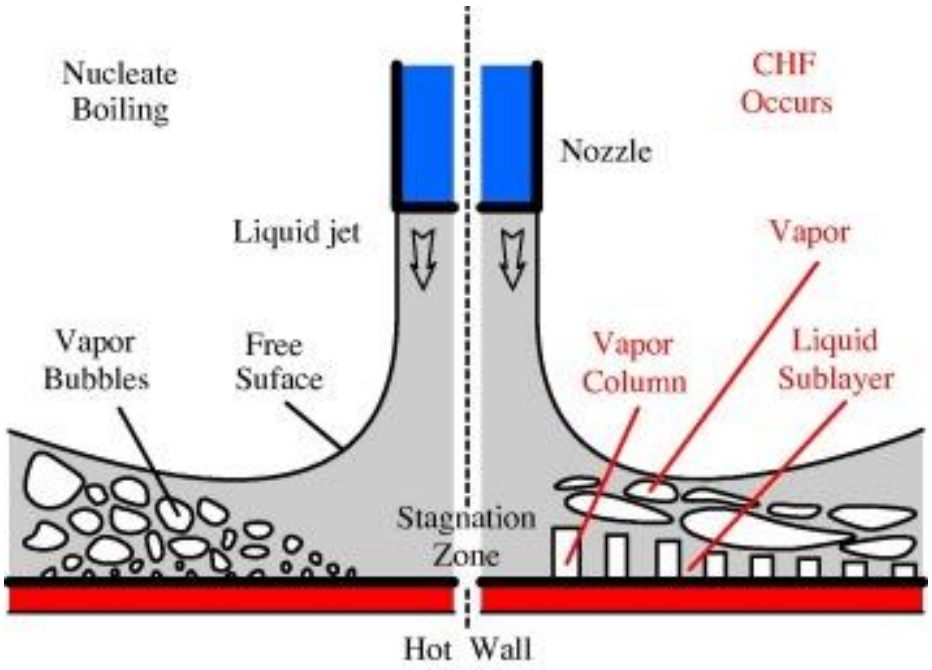

Figure 2.8 – Cross-sectional view of jet impingement effect for cooling of a hot wall [7]

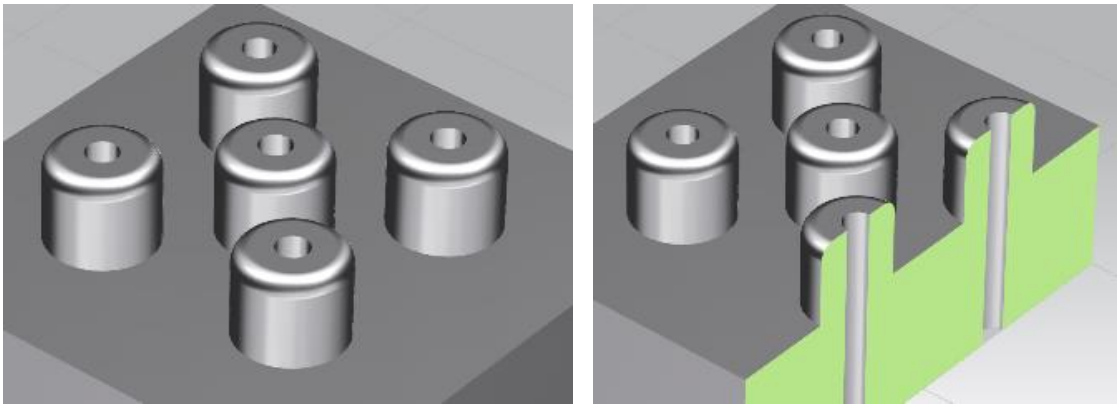

Figure 2.9 – Illustration of jet-impingement nozzles etched into a silicon substrate

Another design type is the radial flow design. Shown in Figure 2.10, this design also uses the jet impingement effect initially but includes a single inlet in the center of the device to deliver all the fluid of the system. The fluid flows outward radially away from the center of the device and exits the flow zone near the outside edge. This approach also creates a non-uniform fluid velocity profile, which depends on distance away from the central inlet. Non-uniformity and localization of flow can also allow for targeted cooling of possible hot spot locations. Flow manifolding for collecting and recombining the exiting fluid can be a challenge with this design. [8]

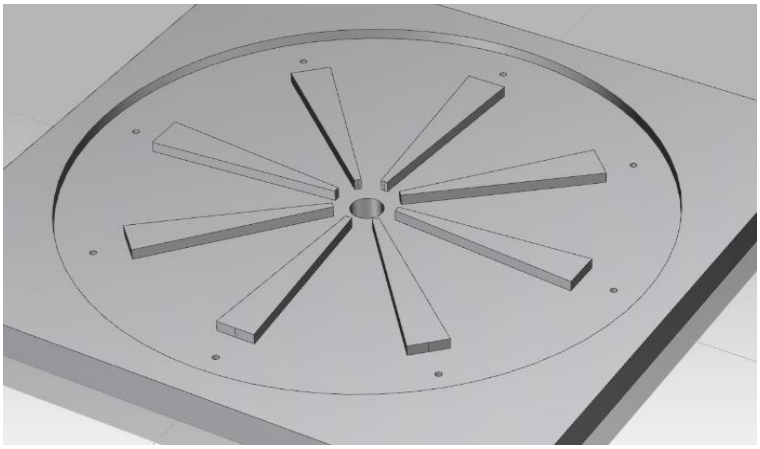

Figure 2.10 – Radial design for microfluidic cooling (central port)

Differing design types can also take a unidirectional approach. A simplistic microchannel design involves sending fluid into a channel through an inlet and forcing it through the channel in one direction to the outlet. This basic design is depicted in Figure 2.11a. Fluid is directed through an inlet into a microchannel in which heat is rejected to the fluid, and then it exits through an outlet. Some asymmetry in performance may arise since the fluid thermodynamic properties can change significantly from inlet to outlet. Further improvements on this design typically contain micro-pin fins for enhancing the surface area available for heat transfer. Pin fins (Figure 2.11b) can also be fabricated in open areas of micro-cavities and provide sites for mixing of the fluid and, in the case of two-phase flow, are bubble nucleation sites. [9, 10]

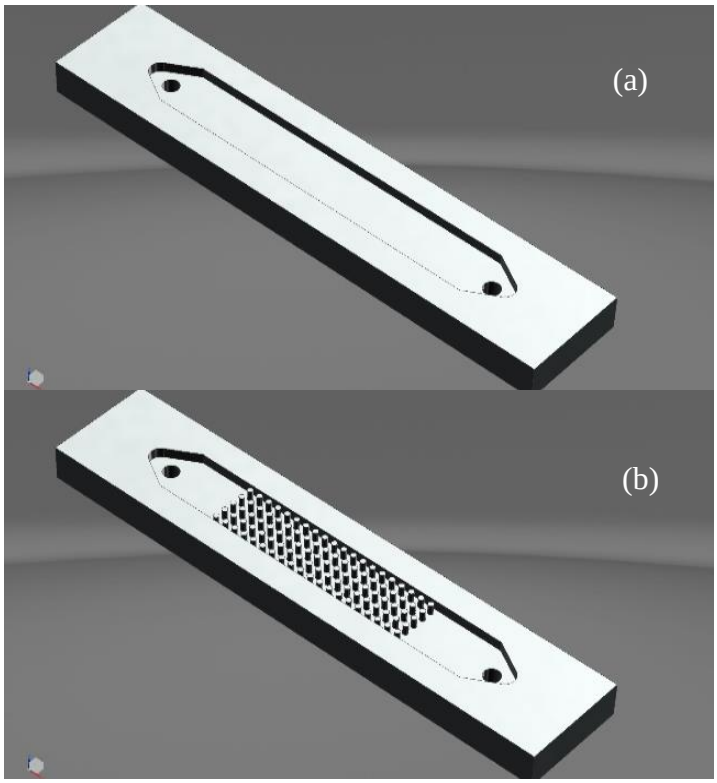

Figure 2.11 – Microchannels designed for on-chip cooling, (a) no pin fins and (b) including pin fins for enhanced area

An extension of this design is the serpentine channel architecture, which winds the microchannel in a snake-like fashion to cover a larger area in strips. While this design, seen in Figure 2.12, maintains a relatively lower flow rate for the actively cooled area, the pressure drop can be significant due to the relatively long channel.

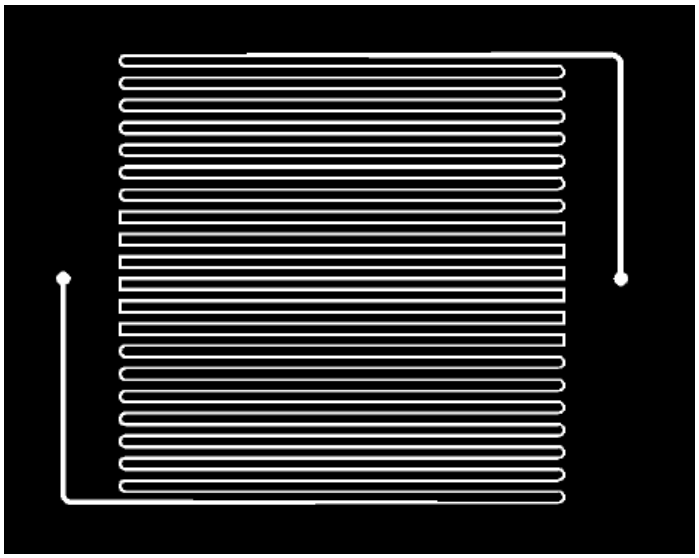

Figure 2.12 – Serpentine channel for on-chip cooling

2.4 Designs Used in the Scope of This Work

Various theoretical and prototype designs are the subject of the objectives in this work. Each has its own unique design considerations and make-up but fits into the scope of this work because of mechanical and reliability concerns, which drive modeling and experiments to address such issues. It is important to identify the key design elements of the die-substrate assembly unique to an integrated microfluidic architecture. These include fluid inlets/outlets with proper seal, a flow domain for fluid passage, electrical and mechanical connections between stack levels (through-silicon vias and solder

interconnections), as well as heat sources. The designs discussed herein illustrate these characteristics.

2.4.1 Theoretical Design for Background Cooling

The first design, which is referred to as Theoretical Background Cooler (or Design A), includes all of the key features mentioned and is analyzed to understand structural integrity in a microfluidic cooler device with through-silicon vias. A representative architecture is shown in Figure 2.13. This is the main subject device of Objective 1.

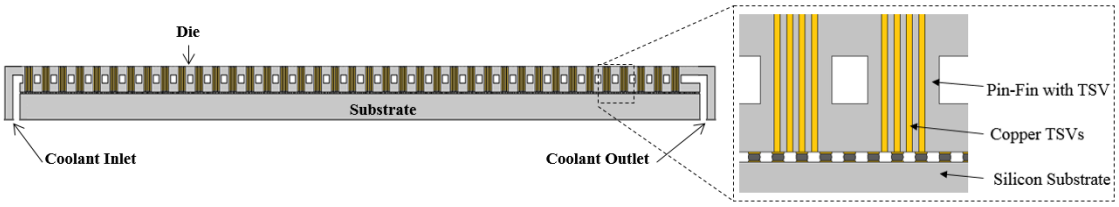

Figure 2.13 – "Theoretical Background Cooler" – Representative 3D architecture for finite-element analysis of generalized microfluidic cooler

2.4.2 Thermal Background Test Vehicle

Within Objective 2, several designs are examined including the Thermal Background Test Vehicle (Design B). The device, shown in Figure 2.14 with a top view and Figure 2.15 (side view), is primarily designed for testing two-phase flow in a full-scale device with active heaters.

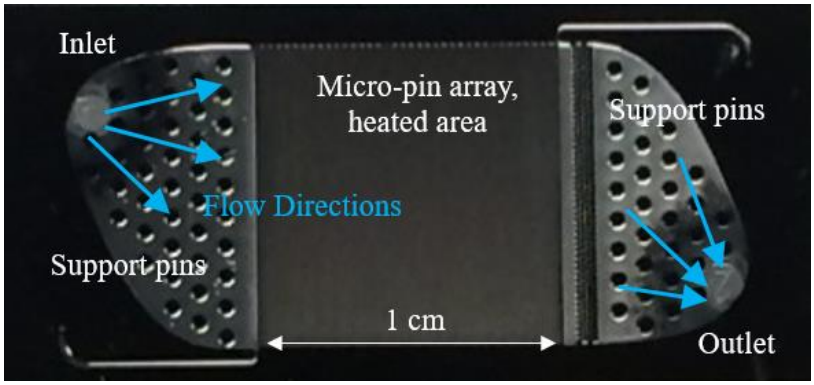

Figure 2.14 – Top view for application device, Thermal Background Test Vehicle, third generation

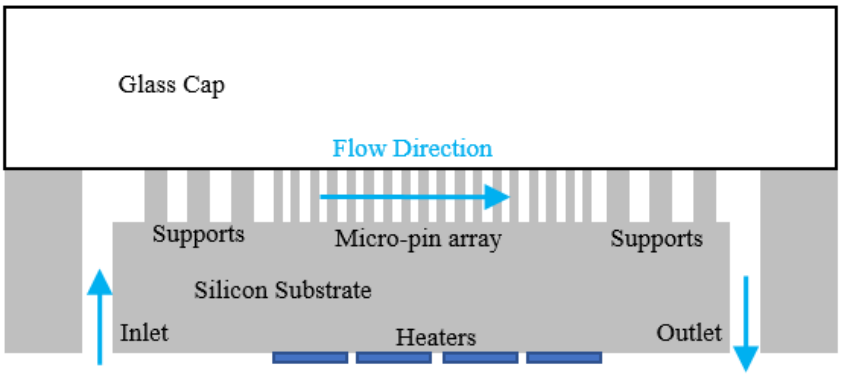

Figure 2.15 – Side illustration of cut section for application device, Thermal Background Test Vehicle

This application device typically measures approximately 3 cm in length, 1.5 cm in width, and 0.12 cm in thickness. The silicon substrate is 0.5 mm thick with the glass cap being slightly thicker at 0.7 mm thick. The actively heated area of 1 cm by 1 cm can produce heat in excess of 500 W. Pressures may exceed 2000 kPa during operation of the devices at this geometric scale. Cracking is a noticeable problem for sustained life of these devices and, as such, it is critical to better quantify the interfacial strength of the system. Experimental data were needed to understand the silicon-glass anodically bonded interface and to determine when cracking initiates and how subsequent crack propagation behaves.

2.4.3 FPGA Liquid Cooler

Another related design is a cutting-edge, integrated micro-pin fin cooler for a mainstream field programmable gate array device (FPGA) [11]. This FPGA Liquid Cooler (Design C) has been successfully fabricated and tested by others with deionized water, yielding dramatic thermal results which are indicative of the potential of embedded microfluidic cooling. The image in Figure 2.16 shows what future FPGA microfluidic cooling systems may look like. This design has a micro-pin fin array etched into the backside of an active FPGA device and capped to create a flow zone with ports for microfluidic cooling. Deionized water at 20 ^{o}C is pumped through the system at approximately 3 mL/min. [11]

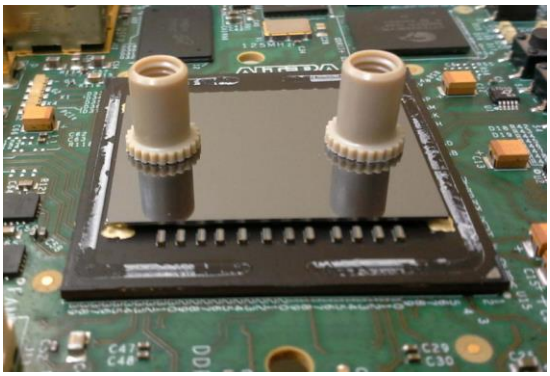

Figure 2.16 – FPGA device with embedded microfluidic cooling system mounted on board. Image originally shown by [11].

The results of thermal and electrical performance studies for this device indicate a drastic improvement in system temperatures for this cooling method versus a stock air-cooled heat-sink. For a supplied power of 20 W to the FPGA, the stock air-cooled heat-sink maintains system temperatures around 50 ^{o}C, while the liquid cooled system is approximately 23 ^{o}C, nearly the same temperature as the water pumped through it [11]. As

this device is mounted to a board in a working system, it is useful to understand the degree to which such a microfluidic cooler experiences warpage. Another section of Objective 2 is dedicated to evaluating whether warpage is positively or negatively impacted by the fabrication processes used to create microfluidic channels in this FPGA design.

2.4.4 Hotspot Cooler Design

A unique micron-scale hot-spot gap architecture designed and fabricated by others in the design team demonstrates localized cooling in excess of 5 kW/cm^2 [12]. An example of this Hotspot Cooler (Design D) is shown in Figure 2.17. In a single microchannel gap between silicon and glass, such large heat flux can be removed locally because of rapid phase change as the fluid is accelerated into the narrow gap of about 10 microns wide. This type of design may have greater application in situations of extremely high local hot spots where targeted fluid delivery is necessary. As part of Objective 2 of this work, mechanical analysis is performed to determine the relative stress levels in a localized hotspot design. [12]

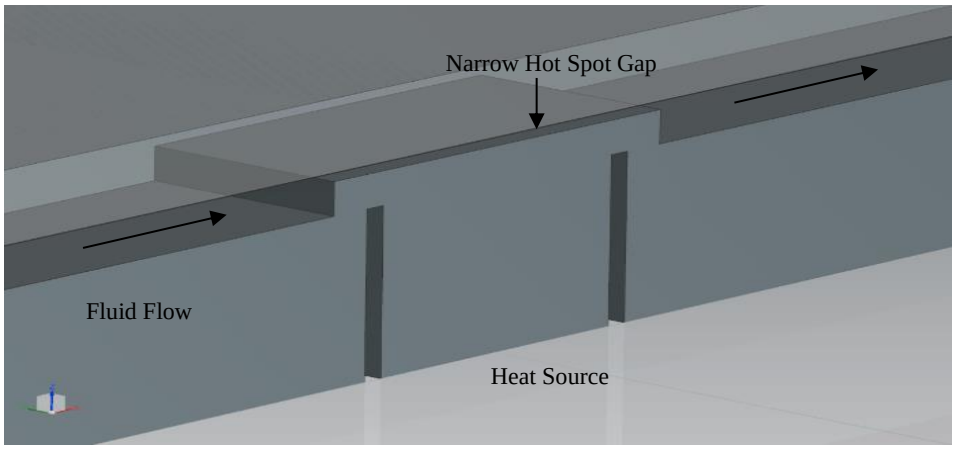

Figure 2.17 – Cut view from the side of hot spot design for removing upward of 5 kW/cm^2

2.4.5 Localized Pin Fin Optimization and Models

The various designs shown are capable of using pin fin geometries to enhance heat transfer performance. Pin fin placement, size, shape, and even material can be tailored to enhance heat exchange at critical locations. Hydrofoil-shaped and cylindrical-shaped silicon pin fins are shown by a scanning electron microscopic image in Figure 2.18. Objective 3 focuses on how optimizing pin fin geometry and separation distance can positively impact device reliability while balancing thermal performance improvement.

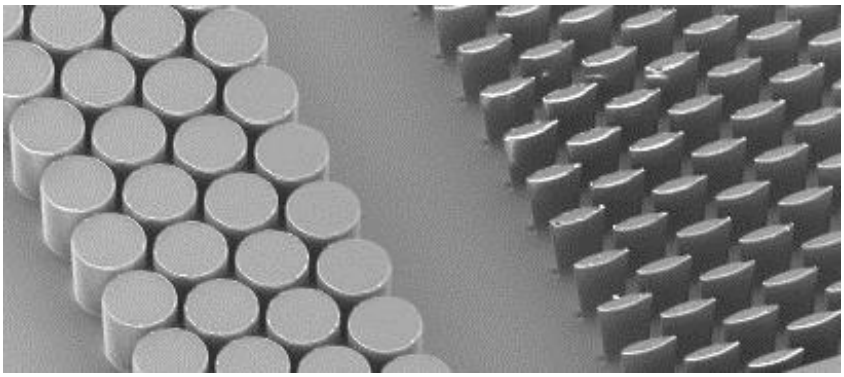

Figure 2.18 – SEM image of hydrofoil and cylindrical pin fins etched into silicon

2.3: Experimental Methods for Brittle Interface Characterization

The mechanical-structural requirements of a high-pressure microfluidic design fall into a wide range of categories but can be related to one of two broad categories for failure methods. The first method is the separation of one mass from another mass. This may include cohesive cracking of a single material, interfacial cracking between two different materials, and slow erosion or removal of material over time. The second method is the degradation of material from a functional state to a non-functional state. This could include

effects such as burnout where heat effects cause chemical changes in materials that affect performance. Of these possible failure modes, the critical failure to be examined in detail within this work is the cracking of the brittle solid bodies surrounding the high-pressure fluid flow space.

While cracking at or near the interface of glass and silicon has been observed for these devices, existing tests for near-interface cracking are not sufficient for this scenario. Although several test techniques, such as double-cantilever beam (DCB), four-point bend (FPB), end-notch flexure (ENF), blister, brazil nut, indentation, superlayer, magnetic actuation [13-21], etc., are available for characterizing interfacial fracture, these tests are difficult to be applied to glass-silicon interface due to the brittle nature of both materials involved. In most of these test techniques, the silicon or glass substrate will typically break before the interfacial debonding propagates under a given external loading condition. On the other hand, some of the test techniques are applicable for studying thin-film delamination from a substrate, rather than for studying interfacial delamination between two brittle substrates.

Among the available tests, characterization of the anodically bonded silicon-glass interface has been attempted in select publications. A modified double-cantilever beam test, as well as the standard tensile test, have been adopted for this set of brittle materials [22, 23]. Applications that could use such a material set of silicon and glass include microelectronics, MEMS pressure sensors, and other sensitive applications with stiff elasticity requirements. In this situation, understanding how high internal pressure induces stress on critical geometric elements of a microfluidic flow domain is a necessity for designing reliable microchannels for next generation on-chip fluidic cooling solutions.

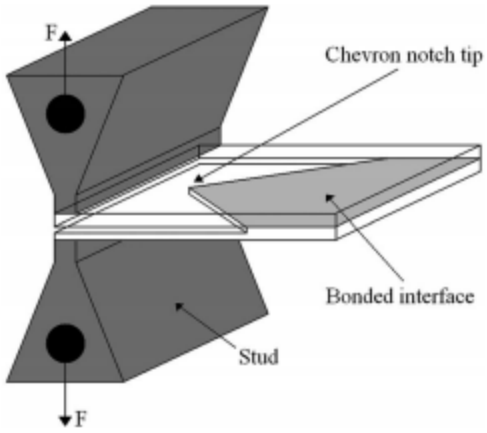

Figure 2.19 – Double Cantilever Beam test with chevron geometry

Figure 2.19 illustrates a modified DCB test for a chevron-shaped test feature. Tests such as DCB do not capture the same loading conditions that result from the internal fluid pressure of this system setup. This is because DCB is highly oriented toward a tensile, opening mode of failure (usually deemed Mode I failure), and thus mostly limited by critical energy release rate for Mode I (G_{IC}). Thus, this test may not be directly applicable for the internal pressure conditions acting on the various silicon-glass interfaces between pin-fin and cap. Devices are designed as part of this work to more accurately incorporate the native loading conditions for high-pressure microfluidics on brittle flow boundary materials. This "Chevron Pressure Cavity" test (CPC test) is the focus of Objectives 4 and 5. The CPC test is specifically designed to mimic the conditions that a high-pressure microfluidic design would endure and to allow for determination of a critical failure criterion for the glass-silicon interface and possibly other bi-material systems.

CHAPTER 3. CO-DESIGN METHODOLOGY AND DESIGN CONSIDERATIONS FOR ON-CHIP MICROFLUIDIC COOLER

This section is intended to shed light on the co-design processes and considerations used in developing all of the microfluidic cooler designs (with particular emphasis on Designs A and B), which are discussed within the scope of this work. Although mechanical reliability is a key concern, the importance of incorporating thermal, fluidic, electrical, and fabrication disciplines cannot be overstated. The intent of this section is to present a co-design approach that successfully yielded a working thermal test vehicle (Design B) for two-phase cooling of a high-powered microelectronics device (Figure 3.1).

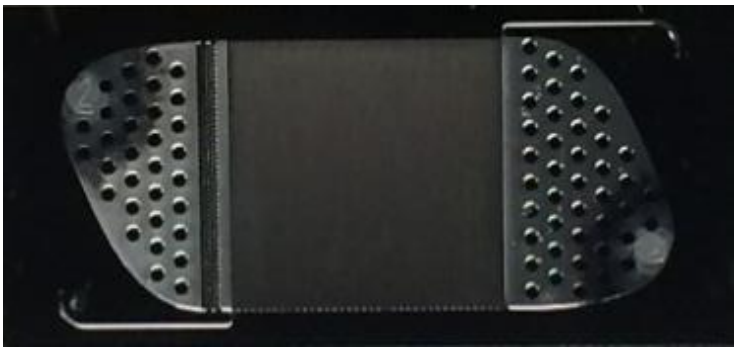

Figure 3.1 – Thermal test vehicle (top view) capable of sustaining and rejecting heat rates in excess of 500 W/cm^2

The target design type and geometric makeup of the test vehicle in question are based upon the end operational goals for this test vehicle. As such, it is valuable to identify any performance deliverables that may impact design choices. For the example design, possessing a relatively larger length scale than prior devices in literature is a primary goal. This means the geometry should be large enough to demonstrate heat removal from an area similar to the size of current die in service. This places the targeted area for focused heat

removal near 1 cm by 1 cm. Future designs may require total heat powers up to 1 kW or 10 times the heat densities of current technologies over the 1 cm by 1 cm active area. This 1 kW/cm^2 for background or average heat removal is another lofty goal that the test vehicle should be designed to attain. Some consideration may also be given to the possibility of non-uniform heating in actual devices that could sustain upwards of 5 kW/cm^2 in localized hot spot zones.

From fabricability and reliability perspectives, this test vehicle should afford repeatable fabrication and maintain operation for a target duration. The target lifetime or mean time to failure for this test vehicle is on the order of 10,000 hours, which is around one year of continuous operation. Based upon these goals, a flexible design framework is established. Some of the other metrics that impact this work and may be considered in other co-design processes include pressure drop of fluid flow through the device, vapor content limits in the two-phase flow, flow rate, temperature gradient allowed in both fluid and solid components, pumping power required, coefficient of performance, and system leakage limits. All of these can affect geometry choices such as device thicknesses, pump size, o-ring sealant selection. For this design type, a wide microchannel design populated with micro-pin fins is selected to allow for bulk fluid flow. The actively heated area of 1 cm by 1 cm can sustain heat rates upwards of 1 kW/cm^2.

3.1 Co-Design Methodology

After selecting a general design type and identifying the primary design criteria, the co-design process proceeds with forming bounds on secondary design criteria. These values mostly impact the geometry of the flow zone as it relates to thermal-fluid

performance and mechanical reliability, but also require knowledge of fabrication limits. To ensure each disciplinary sub-team exerts the proper influence on each design parameter, the team implements a co-design process flow according to Figure 3.2. This ensures that the device can be fabricated successfully, is electrically operational, is structurally sound and reliable, and can meet the thermal-fluid heat removal targets. Thus, from the inception of this design, all three facets of co-design must work together.

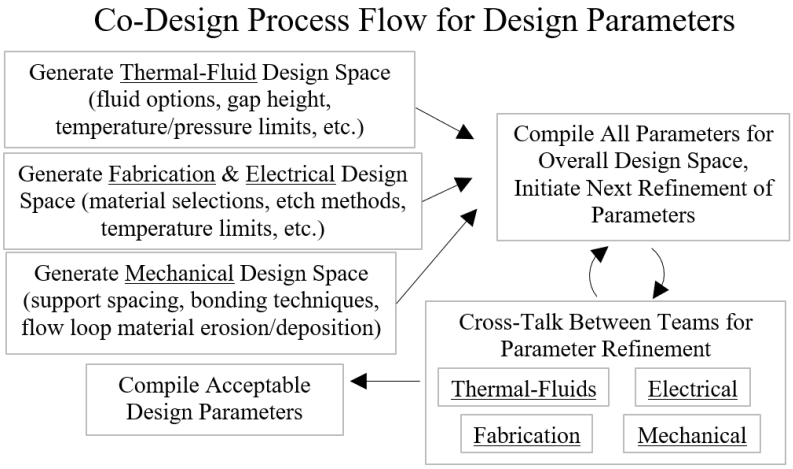

Figure 3.2 – Co-design process for developing limits on design parameters

The disciplinary dependencies of microfluidic coolers are clear: optimal electrical performance is the primary objective, which is dependent on ideal thermal performance, and thus is dependent on reliable mechanical performance. Any cracking or sealant failures can lead to catastrophic fluid containment issues, which may result in total device failure. In high-pressure situations, which can include two-phase liquid-vapor mixtures, the mechanical reliability of the overall system must be maintained in order to ensure electrical and thermal performances are safeguarded. The considerations for each co-design discipline that are required to develop a successful test vehicle can be examined individually beginning with thermal-fluid design.

3.2 Thermal Design Considerations

As this is primarily a thermal management problem, the thermal-fluid considerations are immense for this co-design process. With an embedded microchannel design type selected, the thermal-fluid team focuses on models and analyses to select the working fluid to be used, the geometry of the flow zone, pin fin specifications, and flow loop infrastructure.

The thermal-fluids team develops a key optimization study to first determine the best candidates for working fluids to be used in the microfluidic cooling designs. De-ionized water is useful as a readily available working fluid, but it has a sub-ambient operating pressure for the target saturation conditions of two-phase flow. Organic fluids like methanol and fluorocarbon refrigerants are also key contenders especially at high pressure conditions. The results of this fluid study (shown in Figure 3.3) indicate that, to achieve the greatest relative benefit (heat removal rate per gap height, k/H) for the lowest relative cost (pressure of the system, P_{out}), the best candidates are water, R134a, R245fa, and MeOH [24]. Methanol is discarded due to contamination factors, leaving water for low-pressure designs (although water inherently poses other risks such as becoming electrically conductive due to impurities), and R134a and R245fa as candidates for the high-pressure designs. [24, 25]

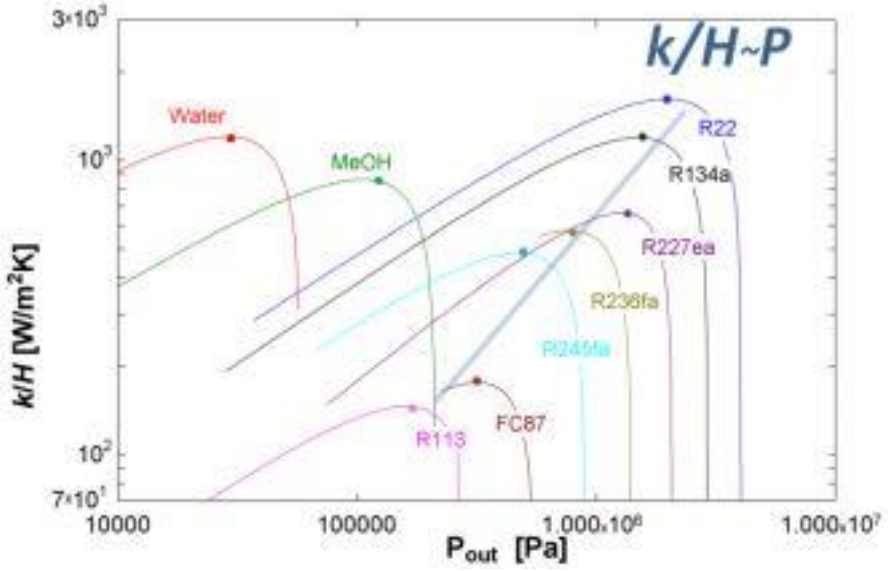

Figure 3.3 – Working fluid selection through optimization of heat transfer [24]

An approximate refrigeration cycle that these design use to remove heat from the microelectronic system is shown in Figure 3.4. To understand two-phase flow, it is useful to note that the heat absorption leg of the cycle takes place approximately from indicator "1" to indicator "2". Most of the heat transfer to the refrigerant within the chip occurs at these saturation conditions. Even though the fluid absorbs heat, the temperature of the two-phase fluid drops during this process, since the pressure drops as the fluid flows downstream. For these saturated conditions, the temperature decreases with the drop in pressure. The total enthalpy in the fluid does increase due to the phase change from liquid to vapor as the quality (vapor content) increases.

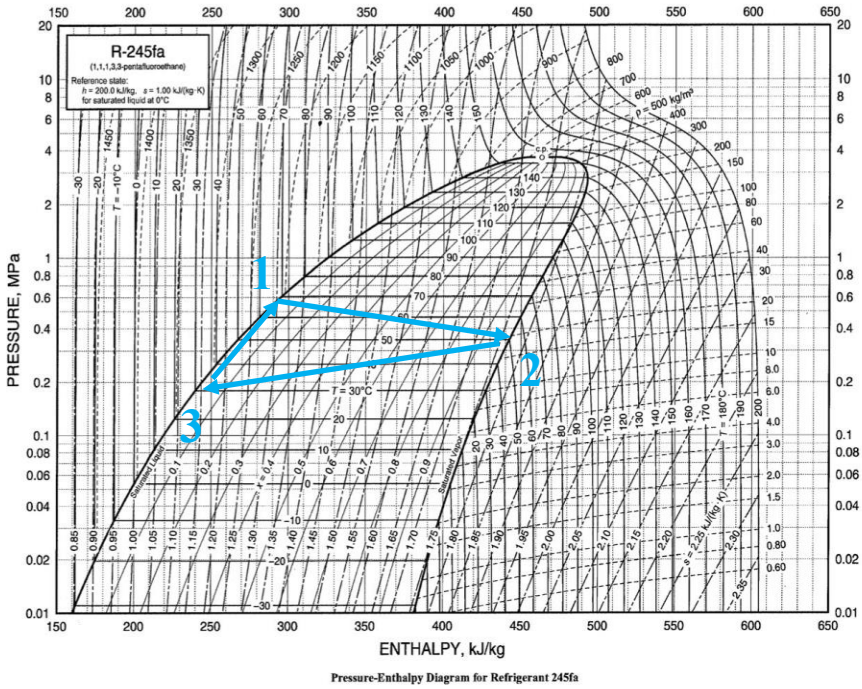

Figure 3.4 – Example refrigeration cycle for closed loop operation

The selection of water for the low pressure case and the refrigerants for the high-pressure case also creates restrictions on the possibilities of gap heights, operational pressures, and temperature regimes that are optimal for this design.

Another key thermal-fluid design consideration is the potential inclusion of micro-pin fins in the flow zone. An image of pin fins, which have been etched out of a silicon substrate, is shown in Figure 3.5. The addition of pin fins in the path of the working fluid creates two avenues for heat transfer enhancement within an equivalent working volume. The first increase arises from adding surface area, while the second comes from circulation and mixing effects. Particularly for two-phase flow systems, pin fins in the path of the fluid can be sites for bubble nucleation and thus heat absorption locations due to phase change. Pressure drop is the primary cost of adding pin fins to a plain microchannel, but

this cost can be a worthwhile tradeoff given the possible improvements in performance. The effective increase in convective heat transfer has been shown to reach a factor of 3 over a plain microchannel and could attain higher levels with greater area enhancement and pin fin geometric refinement. [26, 27]

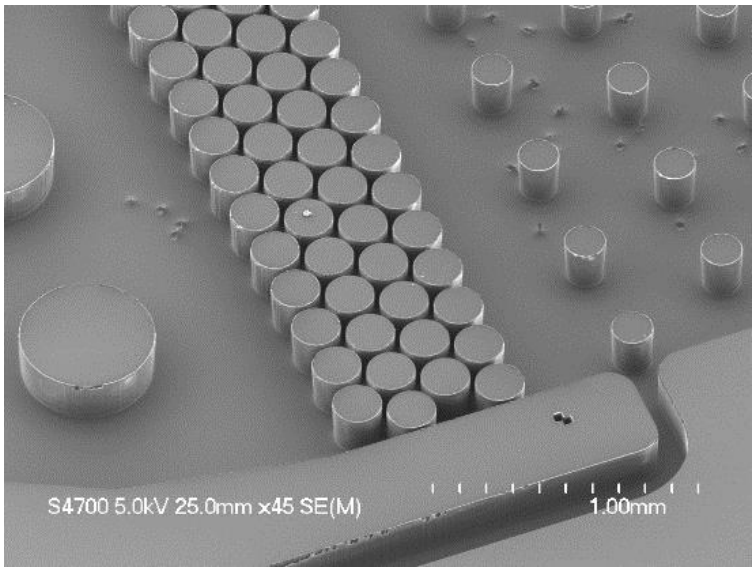

Figure 3.5 – SEM image of micro-pin fins etched into a silicon substrate for microchannel architecture

For this particular design, a closed flow loop design is selected for the experimental setup of the test vehicle. Using a gear pump to provide a steady flow rate, the working fluid is pumped into the device at subcooled conditions and attains saturated conditions for phase change and two-phase flow within the device. The flow loop design matches that of Figure 3.6 and includes the pump, reservoir, heat exchanger, and other instruments for monitoring pressure, temperature, and flow rate [25]. The flow loop can include a condenser for higher outlet qualities. Additional care is taken to ensure proper sealing of

the device within a polycarbonate package system with o-rings at all inlet and outlet ports. The reliability of the overall system hinges on negligible leakage, and the o-rings are a critical component for system integrity. With all of these various materials, the design team found that it is vital to ensure that no interaction between working fluid and flow loop components create reliability issues. Problems such as erosion or deposition of material in unexpected locations of the flow loop have the potential to cause clogging or cracking.

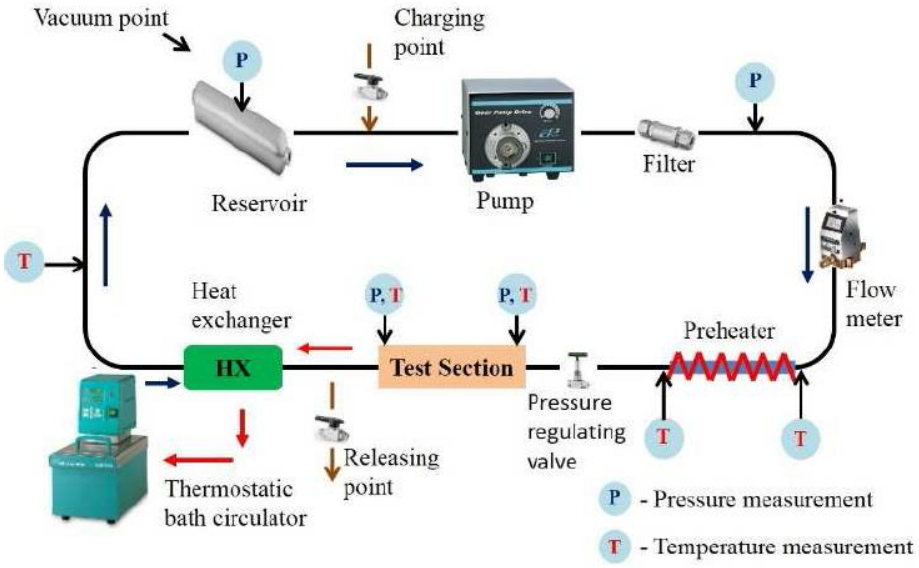

Figure 3.6 – Flow loop design and components utilized [25]

3.3 Fabrication and Electrical Considerations

The thermal test vehicle architecture is also constrained by current fabrication processes and must maintain the required electrical performance needed to generate heat within the test device. Though there are a wide range of possible options for fabrication,

this section presents the selected fabrication approach and highlights some of the critical choices made including material selection, techniques, and process flow.

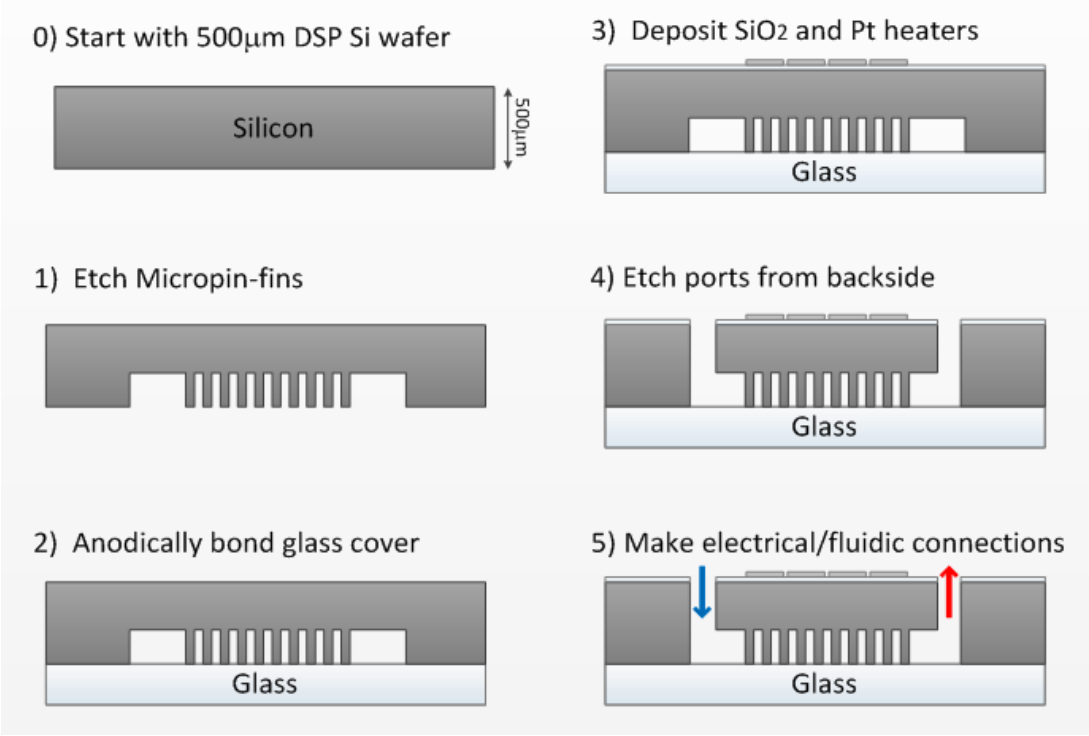

Figure 3.7 – Simplified fabrication steps for prototype thermal test vehicle (side-view illustration) [28]

The overall fabrication process is illustrated in Figure 3.7. A silicon wafer (500 microns thick) is selected as a substrate and etched to form the microfluidic architecture. A Bosch etch process etches approximately 100 µm deep into the silicon to form the flow zone and pin fin structures at a fairly high aspect ratio in excess of 10 to 1. Additional features deemed to be support pin fins, flow redistribution pins, pressure ports, and hot spot structures are also sculpted during this etch process. A cap (in this case Pyrex glass) is then applied to the exposed face of the flow zone using either of two bonding techniques. Epoxy bonding is used in the fabrication process for earlier generation designs, while

anodic bonding for glass and silicon creates the bond in later generations for greater structural integrity at high pressures. With this step, the flow zone is effectively sealed off between the bulk silicon substrate and the glass cap.

The next step involves depositing and safeguarding the electrically active heater elements and resistance temperature detectors on the backside of the silicon. For proper insulation, a silicon oxide layer is deposited on the free silicon face and then the thin-film platinum heaters and temperature detectors as well as the gold pads are applied. Then another insulating layer of silicon oxide is deposited using low pressure chemical vapor deposition. This encapsulation of the heaters protects them from exposure to other elements that may create shorts across the deposited lines, which is a problem that arose in an early generational prototype.

Finally, another Bosch etch step is completed in order to etch out the inlet and outlet ports for fluid flow along with the pressure ports for pressure measurements. After dicing of the sample coupons from the processed wafer, the samples are examined for flaws and prepped for testing. [25, 28]

3.4 Mechanical and Reliability Considerations

While many reliability concerns exist for microelectronic devices in standard systems, there are several new issues that arise when introducing embedded cooling techniques. The co-design process specifically focuses on the issues of internal pressure loading due to fluid flow and material erosion and deposition.

Cracking and fracture of test devices due to high internal pressures for the refrigerant fluid presented a major concern. Though finite element modeling can predict where potential failures may happen, without practical experimental evidence it is difficult to predict all failure modes. Because of this, an iterative design approach is particularly crucial for progressive evolution toward the final successful test vehicle. Over several generational designs (shown in Figure 3.8) the team makes design adjustments to improve flow and increase structural integrity. This generational prototyping approach is discussed in more detail within the scope of Objective 2.

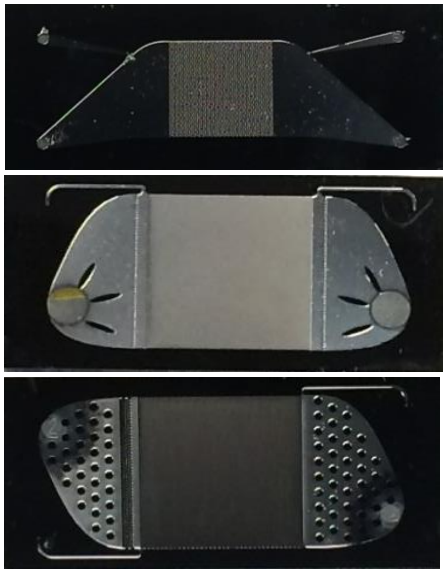

Figure 3.8 – Generation 1, generation 2, and generation 3 (top to bottom)

Fouling also presents a significant concern for the reliability of the entire flow loop including the microfluidic device. While operating various generations of test vehicles, clogging affected pressure drop, flow rate, and overall performance. It has been determined that precipitants from small components in the flow loop, particularly the o-ring sealants, caused this fouling that resulted in clogging of flow ports. As a solution to

this, the thermal-fluid sub team thoroughly washes the polymer-based o-rings to extract any excess material that could linger from manufacture.

Further evidence of fouling is witnessed by a test originally designed for erosion studies using the serpentine design from Figure 2.12. One hypothesis was that a silicon microchannel could experience erosion at high flow rates, and, over time, the geometry of the pin fins may deteriorate, such that eroded material could create clogging and other problems. The qualitative results for this erosion test with water are shown in Figure 3.9 and Figure 3.10 for the 5,000 hours of test operation. The images in Figure 3.9 are taken at the inlet port of the device before and after the test, which suggest an increase in the material stored at this location.

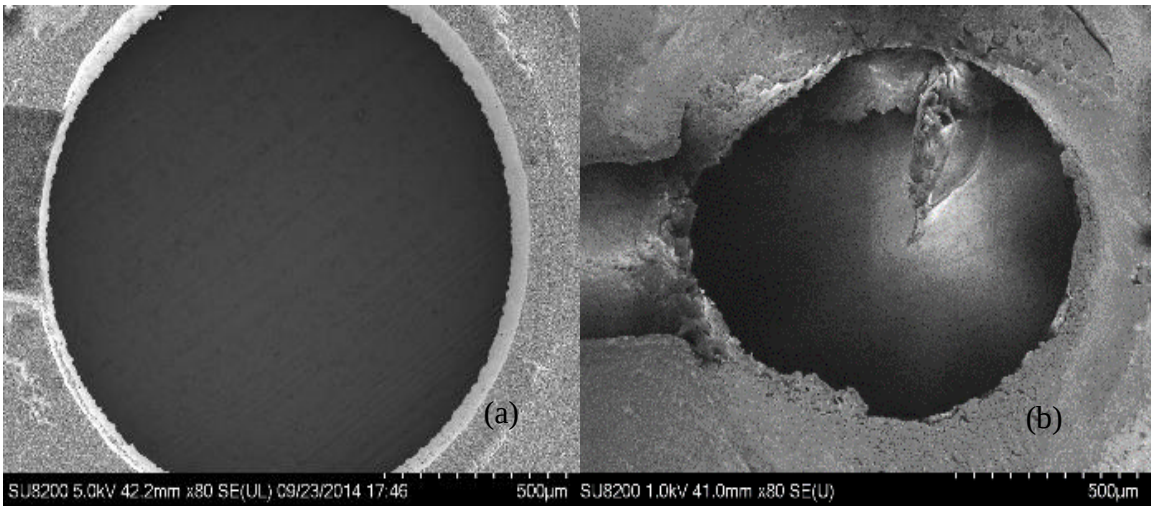

Figure 3.9 – SEM images before (a) and after (b) 5,000-hour erosion study

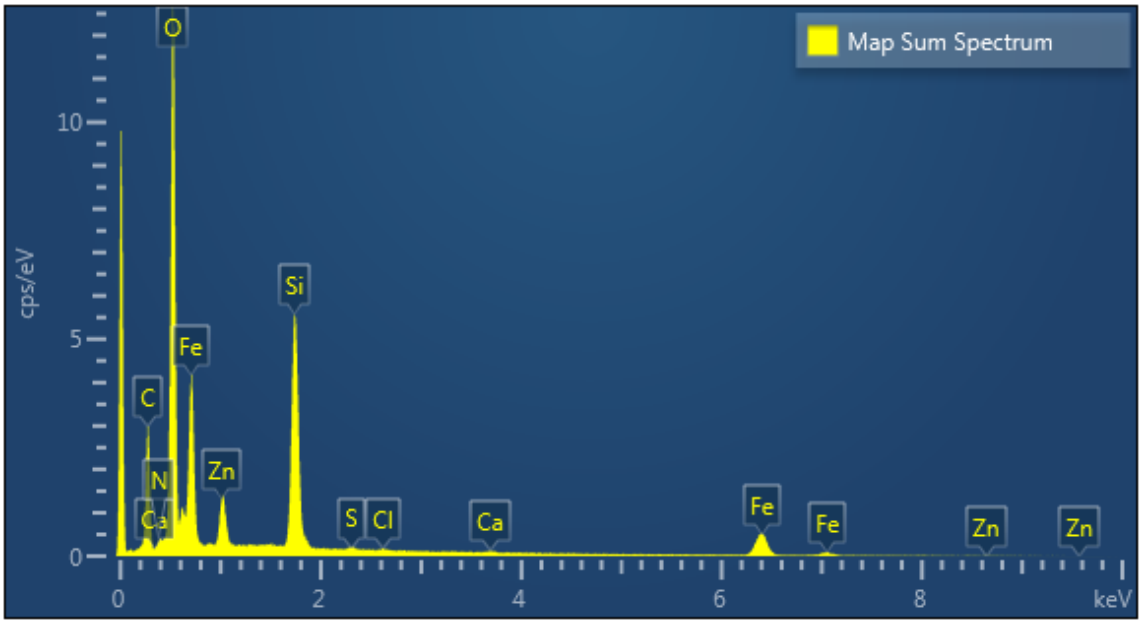

Figure 3.10 – Spectrum analysis of critical site after erosion test

The results from the erosion study indicate deposition from other flow loop sources is a greater concern than actual erosion of the ceramic silicon microfluidic device. Elements of iron, zinc, and excess oxygen pervade the surface of the deposited material at this port. Iron oxide (rust) was observed upon dismantling of the device. As with the o-ring issue, the erosion study underscores that clogging is a major concern and all elements of the flow loop must be tested for possible contaminates.

3.5 Results for Co-Design Process and Test Vehicle Thermal Performance

The team's final goal is to experimentally operate the test vehicle and generate meaningful data for the target metrics. With this multi-disciplinary co-design process and iterative prototyping, viable results are obtained for target heat generation rates near 500 W/cm^2 for background cooling and 5 kW/cm^2 at hotspot locations. Characteristic results for bubbly flow are shown in Figure 3.11 for the primary array of pin fins in the test device.

Phase change of the working fluid can be seen by the lighter gray region in the downstream portion of the pin fin array as indicated by the demarcation lines.

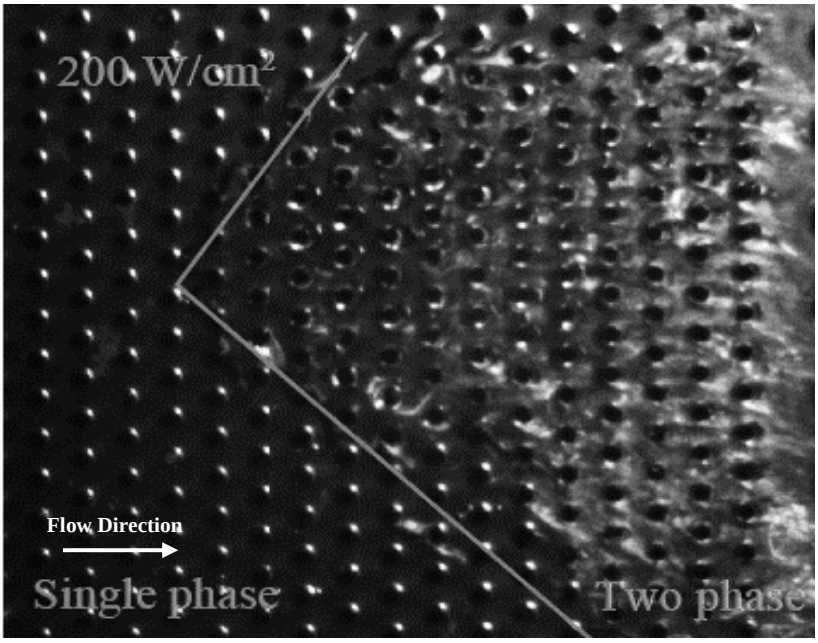

Figure 3.11 – Flow boiling of water in Design B test vehicle [29]

Specific results for the lower pressure refrigerant R245fa suggest even at high heat fluxes up to 326 W/cm^2, the maximum device temperature is kept below 130 ^{o}C even at the source of heat generation. Dryout occurs near the outlet of the device as a significant amount of heat is absorbed through phase change. By increasing flow rate above 120 mL/min and potentially modifying the pin fin array geometry, relatively low wall temperatures can be maintained even at higher heat fluxes. [29, 30]

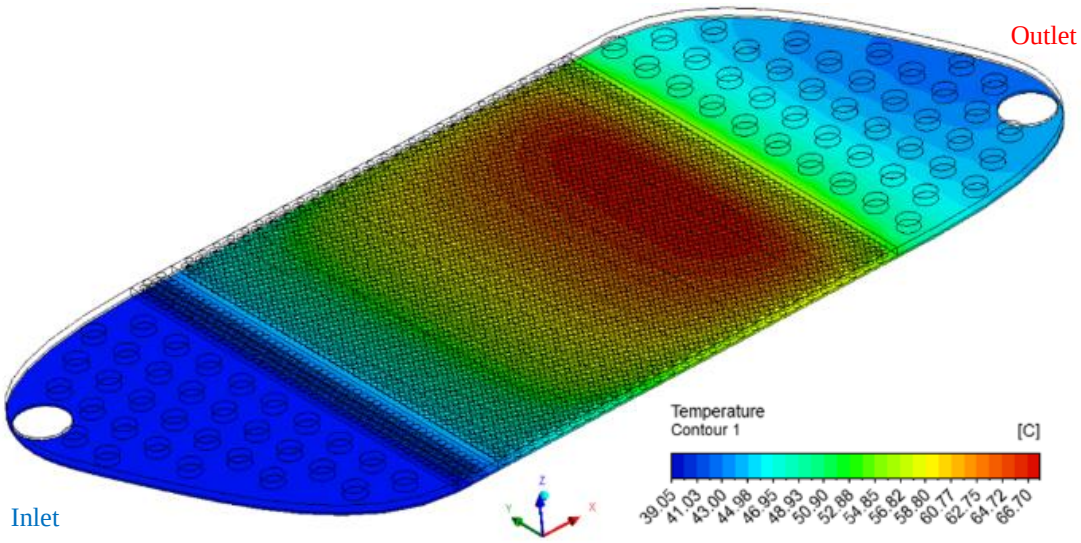

Figure 3.12 – Computationally intensive 3-D flow simulation for R245 for full device

Given the continuing increase in stacked heat densities of microelectronic systems, new approaches like embedded microfluidic cooling will be necessary for high-end devices. The approach for co-design focuses on developing solutions to thermal hot spot issues, fluidic leakage and particle deposition, electrical concerns, and mechanical issues related to bonding. The team's process successfully results in working test vehicles demonstrating meaningful advances in cooling techniques by cooling rates of approximately 500 W/cm^2 and 5 kW/cm^2 at isolated hotspot locations with two-phase fluid flow.

CHAPTER 4. OBJECTIVES AND APPROACH

The overall goal of this work is to develop a reliable microfluidic architecture for high heat-flux microelectronic applications and to experimentally characterize the bonded glass-silicon interface. This is achieved through an innovative technique and by employing numerical simulations and analytical models to ensure that the interface will not crack or delaminate under given pressure and temperature conditions. This work also aims to examine microfluidic architectures of different generations and designs to achieve its goal. Thus, the first objective of this work is to perform a thermomechanical analysis of a high-pressure, two-phase microfluidic cooler. The second and third objectives is to develop a reliable microfluidic architecture with an appropriate pin-fin configuration. This requires characterizing and understanding the failure modes through analysis of various generations of prototype thermal test vehicles for high-pressure two-phase cooling. These models underscore the significance of understanding, in particular, the failure mode of the silicon-glass interface and provide context for the fourth objective (broken into 4a and 4b). The fourth objective is to develop an innovative experimental test technique for evaluating the mechanical performance of a silicon-glass interface. By using a pressurized cavity to apply load on the silicon-glass interface, this test more accurately mimics the working conditions of a high-pressure microfluidic cooler than existing test techniques for evaluating brittle interfaces. The second part of objective four of this work is to obtain experimental results from this test technique and determine a critical failure criterion for the silicon-glass interface by incorporating experimental results into analytical models.

4.1 Objective 1: Perform Thermomechanical Analysis of On-Chip Microfluidic Cooler through FEM

In order to provide proper context for the other objectives, this first objective proposes to evaluate the relative mechanical performance of the key aspects of microfluidic coolers in the selected representative design. Models are developed for Design A, Theoretical Background Cooler, to evaluate stresses that may arise due to temperature gradient, coefficient of thermal expansion mismatch, and pressurization effects. The sub-goals for Objective 1 are summarized below.

Objective 1 will involve the following tasks:

- Development and implementation of 2D model (Theoretical Design A)
- Development and implementation of 3D strip model (Theoretical Design A)

4.2 Objective 2: Perform Mechanical Analysis of Microfluidic Test Vehicles for Design Optimization

Three-dimensional models of the Thermal Background Cooler (Design B), FPGA Liquid Cooler (Design C), and Hotspot Cooler (Design D) are also developed to explore mechanical effects in these systems. The finite element modeling of Design B and its prior generational prototypes seeks to verify mechanical performance for device pressures ranging up to 3300 kPa over relatively large length scales (10 mm) and high heat flux (500 to 1000 W/cm^2). A Hotspot Cooler model is also developed to capture pressure effects for this geometry specifically built to remove more than 5000 W/cm^2 from a relatively smaller area (.1 mm^2 to 1 mm^2) at a similarly high pressure of 3300 kPa. These models are critical for examining the mechanical response of the designs while exposed to such high-pressure.

In particular, the stress results for the Thermal Test Vehicle and Hotspot design are highlighted to show the importance of obtaining a better characterization of the silicon-glass brittle interface, which is the focus of the remaining objectives. Additionally, the FPGA Liquid Cooler is also experimentally tested to quantify the degree to which warpage may be exacerbated by an etch process to form microchannels for fluid flow.

Objective 2 involves the following items:

- Development and implementation of 3D models for Thermal Background Cooler generational prototypes (Design B)
- Development and implementation of 3D model for Hotspot Cooler (Design D)
- Warpage modeling and experimental comparison (low-pressure, high-performance FPGA Design C)

4.3 Objective 3: Develop and Conduct Mechanical Modeling for Optimization of Pin-Fin Shape and Spacing

In support of objective two, targeted modeling is also performed to determine trends in stress evolution for pin fins of different shapes and array spacing lengths. Pin fin geometries are varied from cylindrical to hydrofoil to a hybrid cross-section. For the same pressure it is also expected that the farther apart pin fin support structures reside, the greater the likelihood of failure. Objective three seeks to quantify the relative effects of shape and support spacing and also to establish recommendations for future designs and criteria for engineering microchannels architectures with pin fins.

4.4 Objective 4a: Development of Experimental Technique for Mechanical Characterization of Silicon-Glass Interface

The fourth objective is to engineer a novel test technique for evaluating the strength of microfluidic channels under high pressure. This focuses on the modeling, prototyping, and initial experimentation which is required for the development of the new mechanical test technique: the Chevron Pressure Cavity test (CPC test). Initial prototyping and modeling for devices utilize a geometric layout similar to that shown in Figure 4.1. Numerical modeling is carried out both prior to device fabrication as well as after experimental testing.

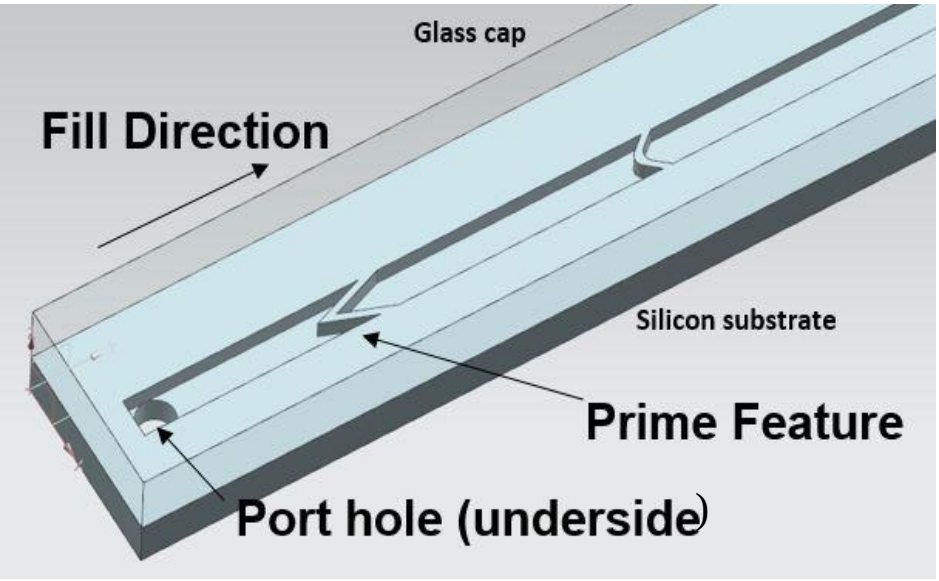

Figure 4.1 – Initial prototype for Chevron Pressure Cavity test

4.5 Objective 4b: Chevron Pressure Cavity Test—Experimental Testing and Modeling for Critical Failure Criterion of Silicon-Glass Interface

Objective 4b ties the prior objectives together with the common goal of characterization of the silicon-glass interface. The goal of this objective is to demonstrate the viability of the novel Chevron Pressure Cavity test for the silicon-glass material system and attest to the test's possible applicability to other material systems. By utilizing the CPC test, experimental data are extracted from various silicon-glass devices. Corresponding models are built to determine critical energy release rate from the experimental data. A virtual crack closure technique is used to determine energy release rate at the failure criterion observed from experiments.

CHAPTER 5. THERMOMECHANICAL ANALYSIS OF ON-CHIP MICROFLUIDIC COOLER THROUGH FEM

The Theoretical Background Cooler (Design A) is used as the focus geometry for the 2-D plane strain model and 3-D strip model for general microfluidic design. Figure 5.1 shows the geometry as well as the boundary conditions applied to these models. Heat generation occurs at one focused latitude within the device near the center of the thickness. To mimic the flow conditions, a varying convective heat transfer condition is used on the interior surfaces.

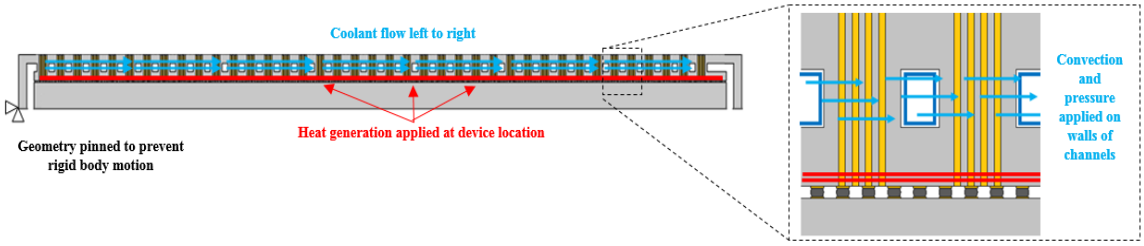

Figure 5.1 – Boundary conditions for model of Background Cooler (Design A)

A generalized one-dimensional thermodynamic model generates the expected convection conditions within the anticipated length of the design. Temperature and pressure of the fluid are also applied to the model to fully account for the impact of the fluid on the model. These conditions are shown in Figure 5.2 for both of the high-pressure refrigerants considered within the scope of this work.

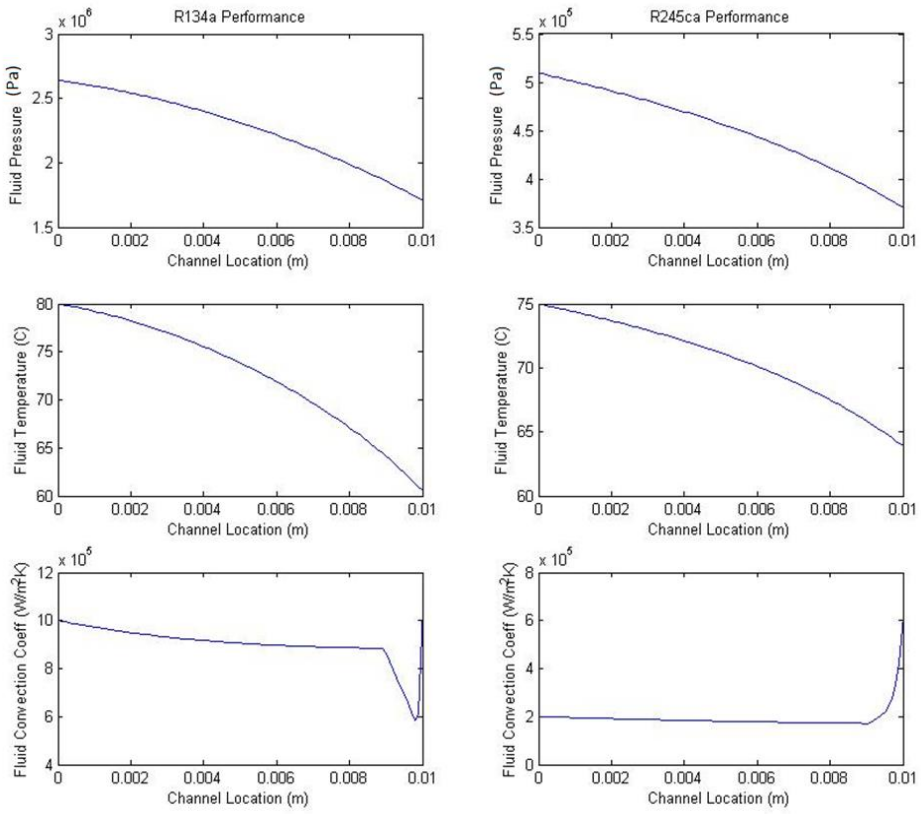

Figure 5.2 – 1-D fluid property profiles across 10 mm channel for refrigerants

In each model, a temperature distribution was first obtained and then applied to a structural model to create thermomechanical stresses. Due to coefficient of thermal expansion mismatches and temperature gradients, stresses arise in the system. Additionally, the pressure applied due to fluid flow based on the 1-D fluid model adds another stressor. Key geometric parameters are shown in Table 5.2. The approximate process temperatures and layout are shown in Figure 5.3 and Figure 5.4 for this theoretical design. First the silicon working material is etched out to form pin fin structures on one side, and then a pristine thin silicon layer is bonded to the exposed pin fins to form the basic working structure for this system. Then, pathways for through-silicon vias are etched and the silicon is oxidized to form the silicon-oxide liner. Through-silicon vias are formed

using electroplating of copper and an anneal step is used to restructure the TSV and form a residual stress. This level can then be soldered to a substrate and underfilled to complete processing.

Table 5.1 – Geometric parameters and values for modeling of Device A

Geometric Parameter	Value
Width_chip	10.7 mm
Height_chip	0.9 mm
Diam_pin	150 µm
Pitch_pin	225 µm
Diam_via	13 µm (each)
Diam_solder	25 µm
Pitch_solder	50 µm
Height_channel	100 µm

As seen in Figure 5.4, the models account for temperature profiles associated with various processes such as annealing, solder assembly, and underfill cure. With this information it is possible to account for the residual stresses present upon assembly of the microfluidic architecture on a substrate.

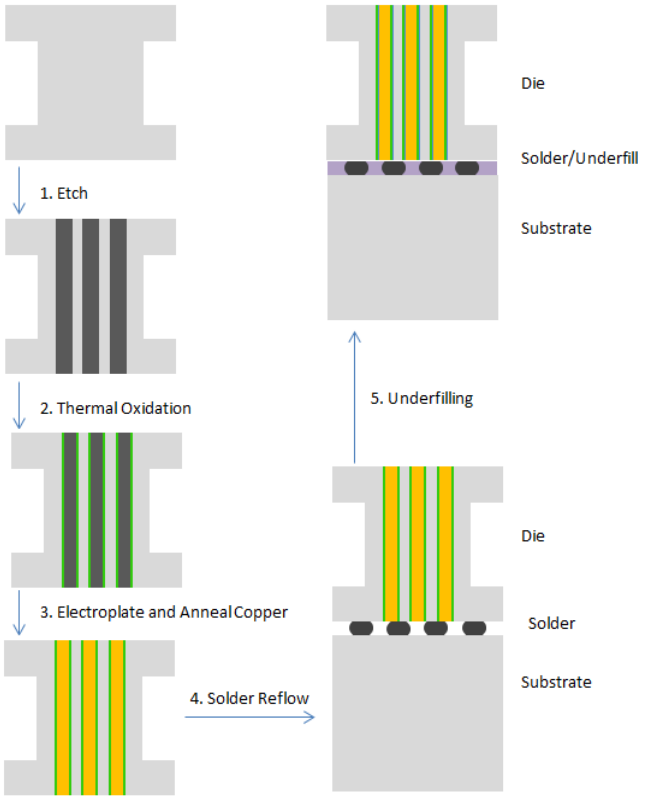

Figure 5.3 – Theoretical fabrication process possible for Design A

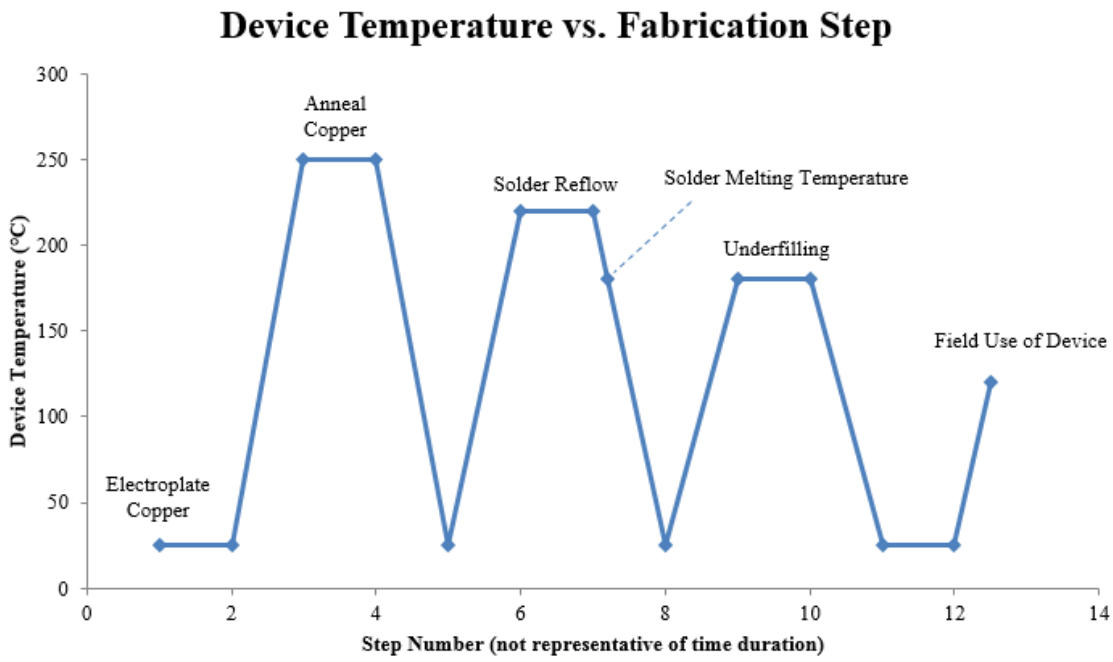

Figure 5.4 – Fabrication process flow with temperatures of processing

The material properties in Table 5.2 include the material model type and primary values near standard conditions for the copper TSV's, the silicon oxide liner around TSV's, the bulk silicon, solder ball components, and the associated underfill material. Because residual stresses are a concern for copper primarily, it is of note that temperature dependent models are used for copper and solder. Though elastic-plastic models are used (solder uses Annand's model), this modeling assumes that yielding of copper causes enough damage to lead to cracking and failure of TSVs.

Table 5.2 – Material properties for relevant materials within 2-D model

Parameter	Solder	Copper	Silicon	Silicon Oxide	Underfill Polyimide
Material Model	Temp Dependent, Elastic-Plastic	Temp Dependent, Elastic-Plastic	Elastic Anisotropic	Temp Dependent, Elastic	Elastic, Anisotropic
Modulus of Elasticity, E	30 GPa	80 GPa	140 GPa	70 GPa	5 GPa
Poisson's Ratio, ν	0.28	0.3	0.28	0.16	0.25
Thermal Conductivity, k	78 W/mK	400 W/mK	150 W/mK	0.5 W/mK	0.5 W/mK
CTE, α	20 e^{-6} /^{o}C	17.3 e^{-6} /^{o}C	2.6 e^{-6} /^{o}C	1.4 e^{-6} /^{o}C	25 e^{-6} /^{o}C

5.1 Two-Dimensional Model for Theoretical Background Cooler

With the geometric setup in place and materials models applied, sequential modeling takes place to build in the residual stresses of the system. Element birth and

death is utilized to active appropriate material elements at the expected processing temperatures. Once the residual stresses have been accounted for, the operating thermal boundary conditions are applied to the system. A varying convection boundary condition is applied to all free edges of the 2-D model according to the thermodynamic profile from Figure 5.2. Heat generation is applied to match the assumptions of the 1-D thermal model (300 W/cm^2 for R245 and 1 kW/cm^2 for R134) as well as a hotspot condition having five times the heat flux as the background rate. The resulting temperature distributions for the two refrigerant cases are shown in Figure 5.5 and Figure 5.6.

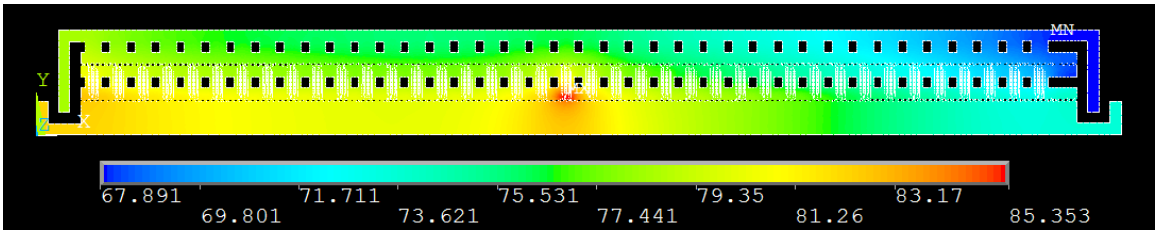

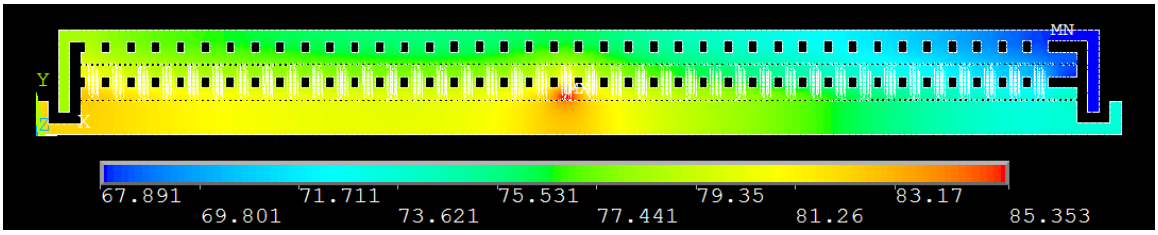

Figure 5.5 – Temperature distribution for 2-D case for R245ca

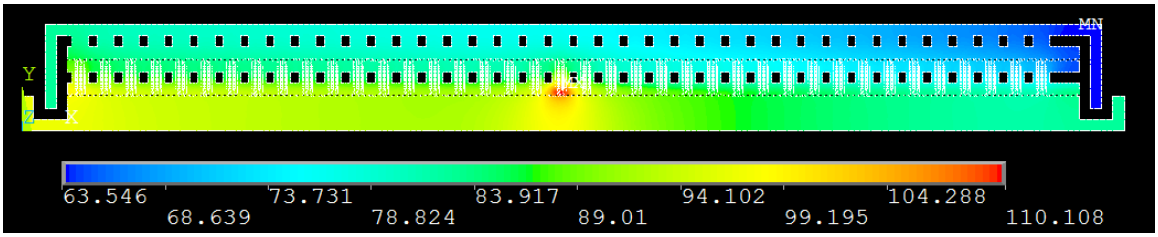

Figure 5.6 – Temperature distribution for 2-D case for R134a

With a known temperature distribution determined, the sequential model proceeds to the mechanical phase in which the temperature distribution is applied to the system along with expected pressure conditions from the 1-D thermodynamic model. The model is also constrained to prevent rigid body motion, but only at a single node so that the system may still warp upward. With these conditions in place, the model is solved to yield the results in specifically for R134a. While the principal stress in the brittle materials (silicon and silicon oxide) has a maximum of 130 MPa, the majority of the system experiences a nominal stress in silicon of about 30 MPa. Copper von Mises stresses range from 50 MPa up to 85 MPa, which indicates the TSVs may be in an undesirable state of plastic strain in some cases. In order to better understand the stress response and potential for failure of the system, a 3-D strip model (sometimes referred to as 2.5-D model) is also developed for the same geometry and setup.

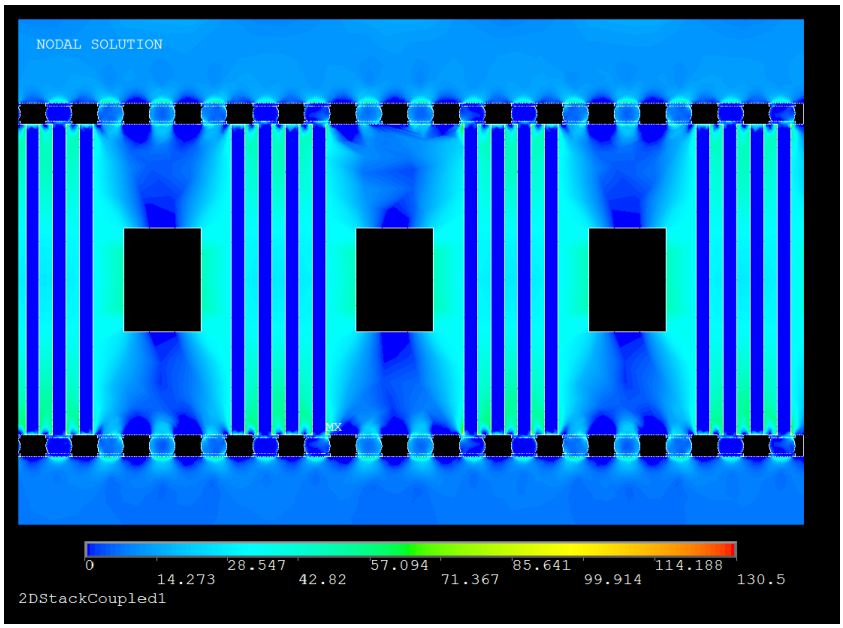

Figure 5.7 – First principal stresses for R134a case of 2-D modeling in MPa

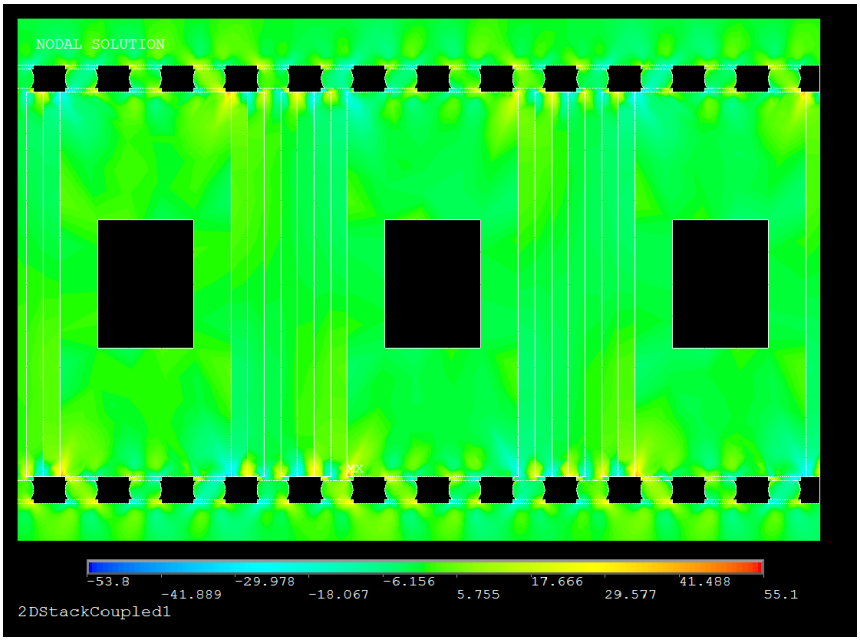

Figure 5.8 – In-plane shear stresses for R134a case of 2-D modeling in MPa

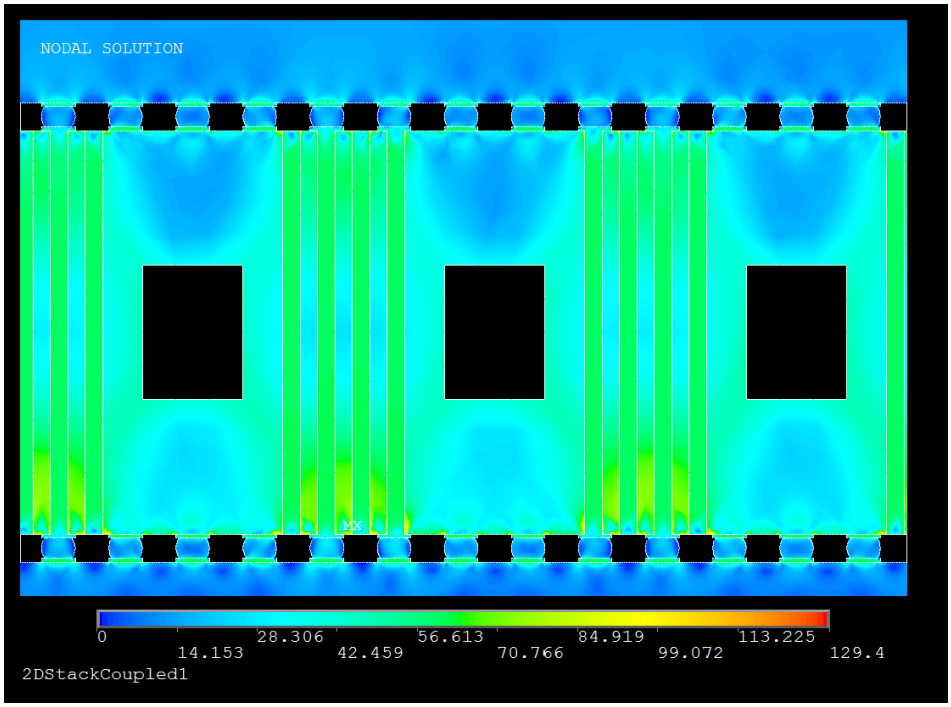

Figure 5.9 – Von mises stresses for R134a case of 2-D modeling in MPa

5.2 Three-Dimensional Strip Model

The 3-D strip model captures the same setup as the 2-D model, but it expands the out of plane dimension to include dimensions that are non-uniform in the third direction. The cylindrical shapes of TSVs, pin fins, and solder bumps are captured for example. A single strip of the 3-D system is modeled to minimize computational intensity. Figure 5.10 shows the essential boundary conditions applied for both thermal and mechanical sequential models. An example convection boundary condition at the inlet is also shown in Figure 5.11. Following the same steps as the 2-D model process, a temperature distribution is determined for the expected working conditions after residual processing stresses have been applied to the system. The resulting temperature distribution for the 3-D strip model is presented in Figure 5.12.

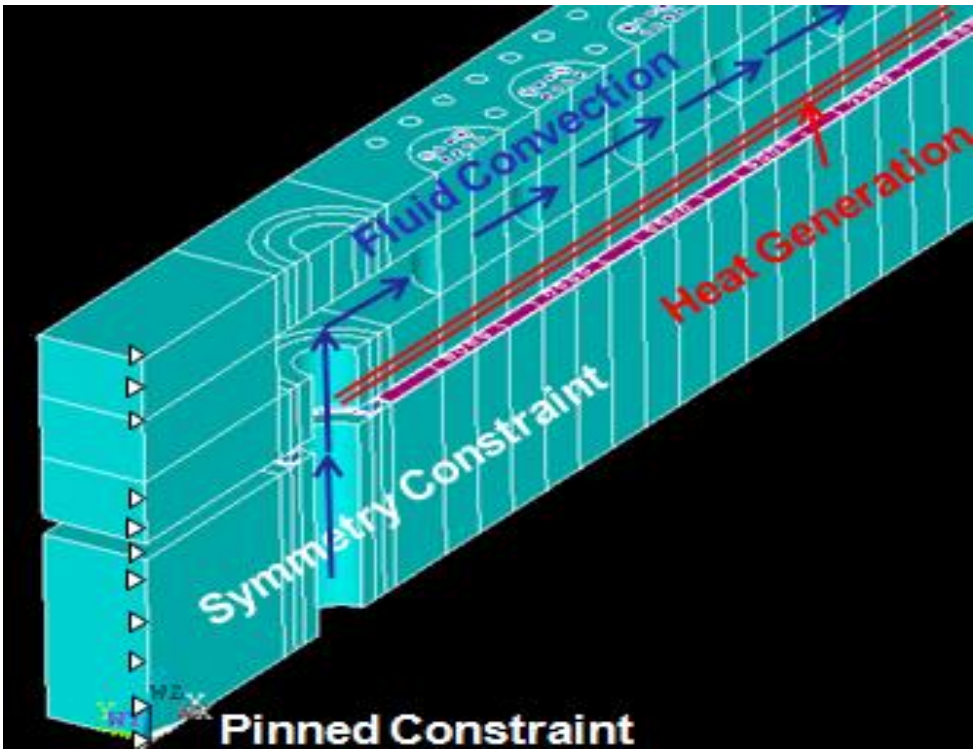

Figure 5.10 – Example boundary conditions for 3-D strip model

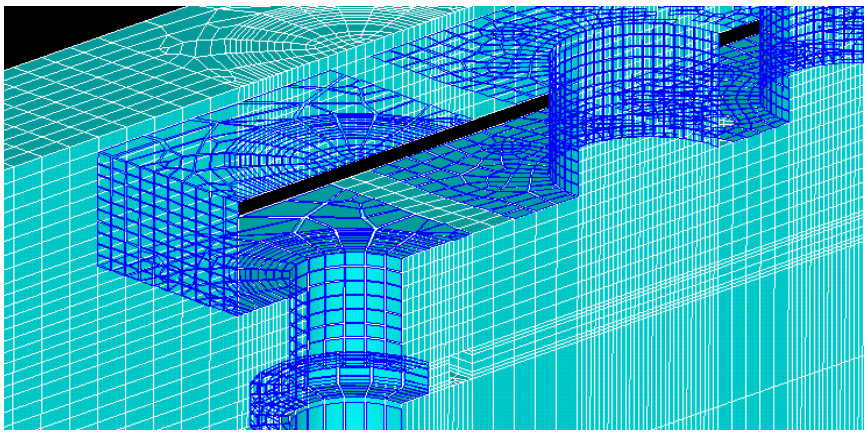

Figure 5.11 – Example convection condition shown on mesh elements for 3-D model

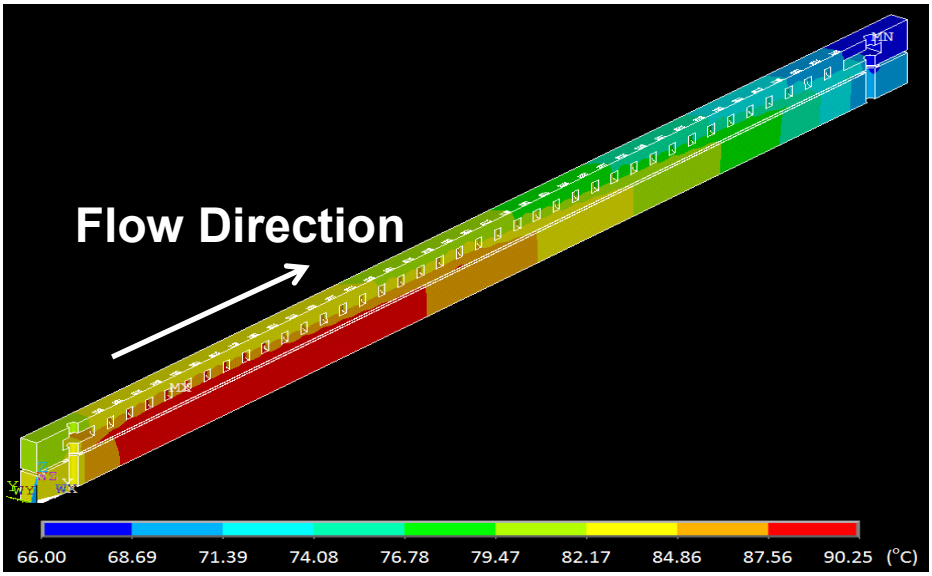

Figure 5.12 – Temperature distribution determined from thermal model for R134a

Because the 1-D thermodynamic model indicates that the convection condition will have slightly higher fluid temperature near the inlet compared to the outlet, the temperature noticeably drops toward the outlet. This is due to the drop in pressure as the fluid flows from inlet to outlet. At the same time, heat is absorbed by the fluid to change phase from

liquid to vapor rather than to increase temperature since it is saturated. After solving for this temperature distribution for refrigerant R134a, it is applied to the structural model as an operating temperature condition. Similar to the 2-D model, the system is constrained to prevent rigid body motion by fixing a single node. This does not hinder warpage of the device. The resulting stress values provided in Figure 5.13, Figure 5.14, and Figure 5.15 evolve from a convolution of residual stresses, CTE mismatch, thermal gradient, and wall pressure.

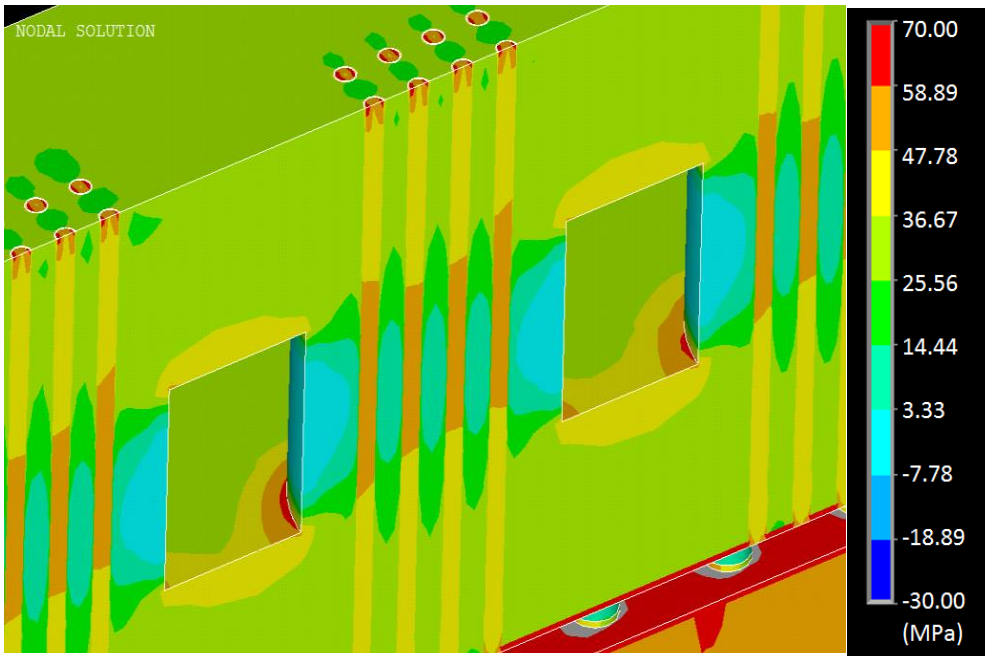

Figure 5.13 – First principal stresses in 3-D strip model

The 3-D model results agree with the 2-D results for shear stress at the ends of the TSVs and at the solder bumps. However the von Mises stress results are higher for the 3-D case (Figure 5.13) and indicate that copper pumping of the TSVs could be a concern, since the stresses are clearly beyond the yield point of 70 MPa and into the plastic domain.

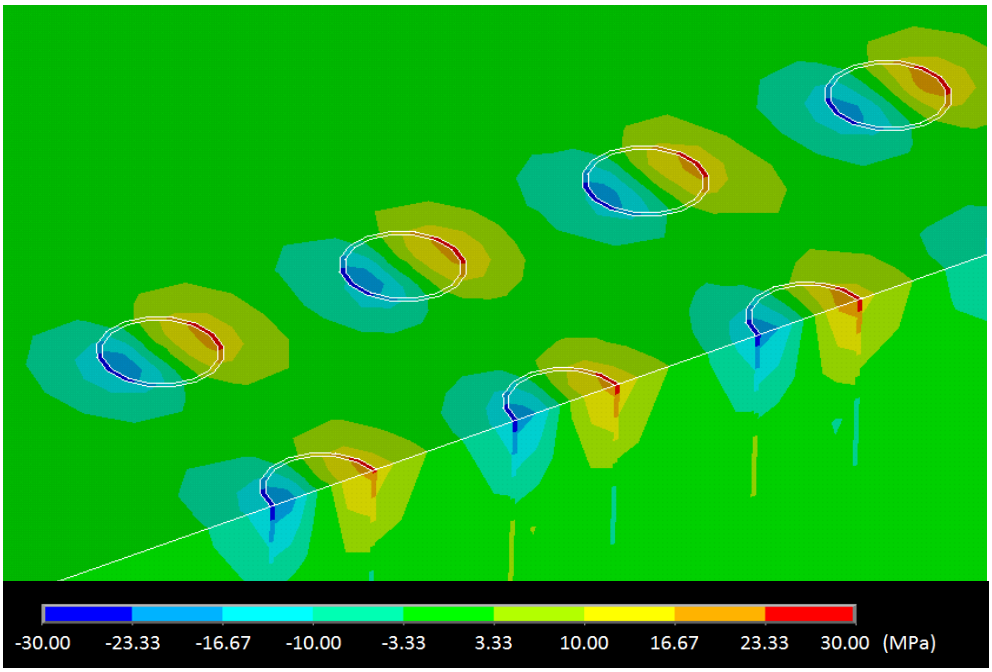

Figure 5.14 – Interfacial shear stresses of 3-D strip model

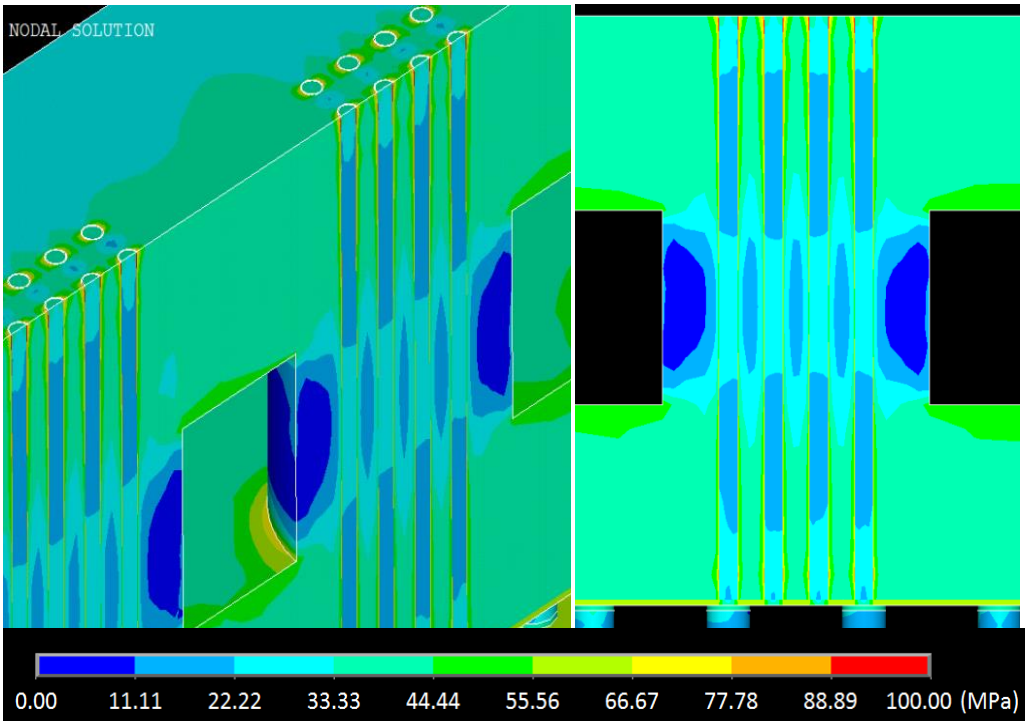

Figure 5.15 – Von Mises stress of 3-D strip model

This parametric, 3-D model of a theoretical microfluidic cooler is valuable for studying the effects of changing certain system parameters. Because the copper vias are a primary concern, the input geometric variables chosen to study are oxide thickness and via diameter because the relationship between copper and oxide liner may affect stress evolution. These geometric variables (which also affect via spacing) are shown in Figure 5.16. The assumed stress-free temperature for copper is also another variable of interest. A design space is created for combinations of these variables while other quantities are kept static.

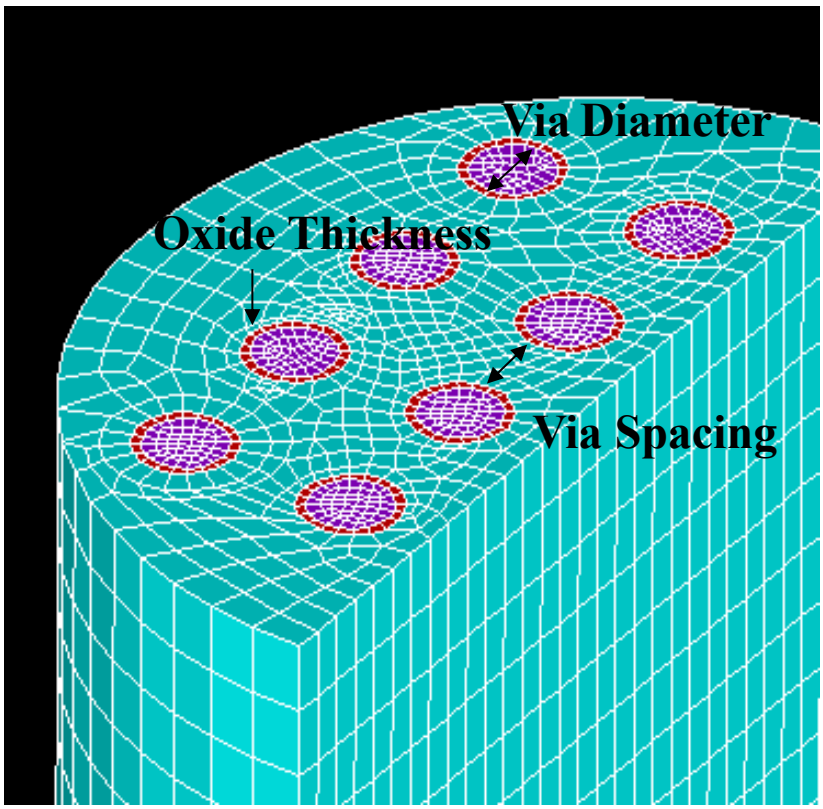

Figure 5.16 – Geometric parameters of focus in TSV optimization study

The input domains of the variables for the design space are shown in Table 5.3. Following the same sequential method for obtaining results, the model is solved for 30

different combinations of input variable values. A design of experiments process is employed to minimize the number of combinations that must be solved. For the results in this study, the range of output stress values is included in Table 5.4

Table 5.3 – Domain for input parameters of parametric study

Factor	Minimum	Maximum
Copper Stress Free Temperature (°C)	25	250
Oxide Thickness (um)	0.5	1.5
Via Diameter (um)	10	15

Table 5.4 – Response range for parametric study

Responses	Results Range
Silicon Max Principal Stress (MPa)	[20.0, 314]
Oxide Max Principal Stress (MPa)	[-11.6, 69.7]
Copper Max von Mises Stress (MPa)	[44.1, 71.0]
Interfacial Shear Stress Max (MPa)	[23.8, 84.2]

The stress response result data are provided to a least means squared analysis to determine four response surfaces for silicon max principal stress, oxide max principal stress, copper max von Mises stress, and interfacial shear stress between oxide and copper. These stress responses follow an equation with constants *A*-*J* and assume a quadratic relationship between the input variables (copper stress free temperature, via diameter, and

oxide thickness) and the output stress value. The equation takes the form of Equation 5.1 with coefficient values tabulated in Table 5.5 for each stress type (left column). Selected constants are highlighted to indicate they have relatively high effect on output stress value.

$$Stress = A(CopperTemp^2) + B(ViaDiam^2) + C(OxideThickness^2) + D(CopperTemp \cdot ViaDiam) + E(CopperTemp \cdot OxideThickness) + F(OxideThickness \cdot ViaDiam) + G(CopperTemp) + H(ViaDiam) + I(OxideThickness) + J \quad (5.1)$$

Table 5.5 – Coefficient correlations for effect of input parameter variation on stress types

StressType2	CopperTemp²	ViaDiam²	Oxide Thickness²	CopperTemp* Oxide Thickness	CopperTemp* ViaDiam	Oxide Thickness* ViaDiam	CopperTemp	ViaDiam	Oxide Thickenss	Intercept
-	A	B	C	D	E	F	G	H	I	J
Silicon	-19.86	7.27	-2.61	3.03	-18.46	-1.56	-118.1	14.04	7.06	163.6
Oxide	22.34	1.61	-4.61	-1.76	-6.65	-4.76	-20.24	5.62	1.89	7.62
Copper	3.96	-0.74	1.33	0.64	-1.37	-0.09	-10.70	1.90	0.05	52.06
Interface	-5.59	-9.29	-2.01	-4.62	-1.70	-3.94	-21.89	0.79	5.90	60.19

The copper stress free temperature has the greatest effect on all stress types. This negative correlation suggests that higher copper stress free temperatures (and thus using a higher temperature anneal process during fabrication) is most beneficial to reducing stress throughout the system with the exception of oxide principal stress. For the oxide liner maximum stress, there is a tradeoff above copper stress-free values of about 150 ^{o}C, as seen in the summary Figure 5.17. Though these issues are not specifically unique to microfluidic coolers, the incorporation of future pin fin geometries with TSVs must incorporate this type of analysis to optimize for minimal stress response.

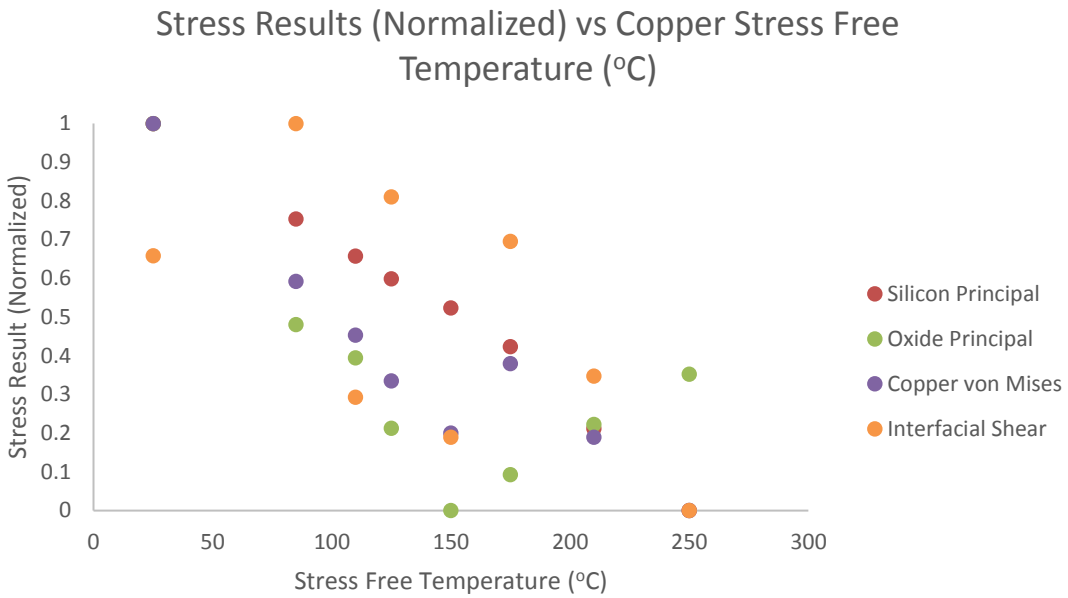

Figure 5.17 – Key stress results for variation of assumed copper stress free temperature (related to anneal temperature)

CHAPTER 6. MECHANICAL ANALYSIS OF MICROFLUIDIC TEST VEHICLES FOR DESIGN OPTIMIZATION

Within this objective, the mechanical modeling and design iteration process that supported the development Design B is presented. Multi-generational prototyping has involved the three device designs imaged in Figure 6.1. In Figure 6.1 the first generation (top), second generation (middle), and third generation (bottom, Design B) show a consistent increase in the utilization of pin fin structures as supports from generation to generation. The modeling, which is presented in this objective, is the driving factor in the increasing use of support pins within this design prototyping process. Additional device-specific structural analyses for Devices C (FPGA Liquid Cooler) and D (Hotspot Cooler) are also included.

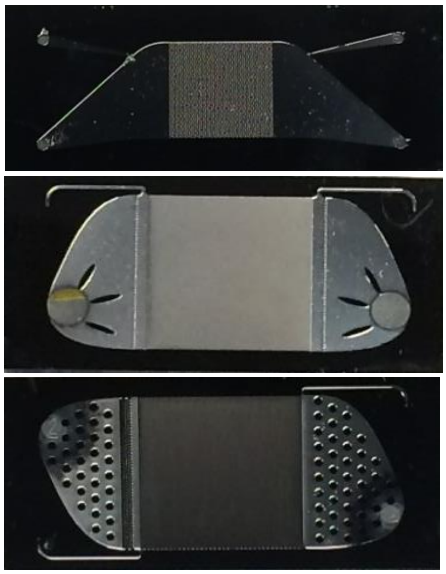

Figure 6.1 – Generation 1, generation 2, and generation 3 (top to bottom)

6.1 Generation 1 Mechanical Modeling

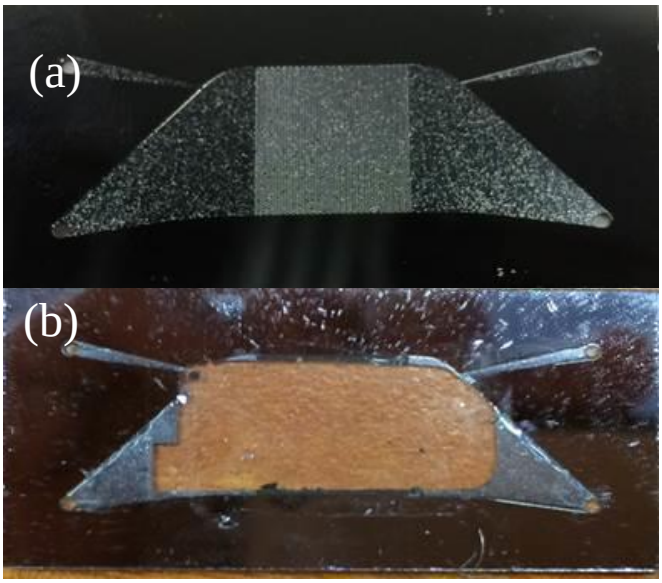

Figure 6.2 – Photograph of a working generation 1 device (a) and fractured device after fluid pressure test (b)

A practical example of the pressure challenges observed during experiments involve failures of the first generation design. Figure 6.2a shows the top view of the first-generation micro-pin fin array architecture where the central square region contains the fin array, while the curved regions on both sides of the square region serve as the inlet and outlet regions for the cooling fluid. The inlet and outlet ports are placed in the out-of-plane direction and are not shown in Figure 6.2a. Fluid pressure is also measured in the inlet and outlet regions, as shown in the figure. Failures have occurred for internal pressures between 700 and 800 kPa for these test devices with an example failed sample shown in Figure 6.2b. This failure pressure is significantly lower than the target operating pressures

for high-performance refrigerants. In order to achieve 1000 W/cm^2 in heat removal rate, the target operating pressures for R134a ranges up to ~2 MPa for this microfluidic design.

To better understand the reason for failure of this first generation, simplistic mechanical models are created to model the expected scenario. Initially in the generation 1 design, the glass cap is bonded to the silicon substrate around the edge of the flow zone with an epoxy. In this fabrication approach, the interior pin fins do not have a mechanism for bonding to the glass cap. As illustrated in Figure 6.3, the interior pin fins remain un-bonded. So, similar to a prism-like pressure vessel, when generation 1 is pressurized, the entire flow zone expands, and the larger glass and silicon faces bend, creating a bulging effect. Stresses develop near the boundary of the flow zone as shown in Figure 6.4 for the unrestricted flow zone case. These stresses can create cracking that leads to failure of the device. Thus, epoxy bonding can be a viable solution for bonding at low pressures, but alternative bonding techniques may be required depending upon geometry and the target pressures. For higher pressures, cracking and catastrophic failure was observed for epoxy bonding scenarios.

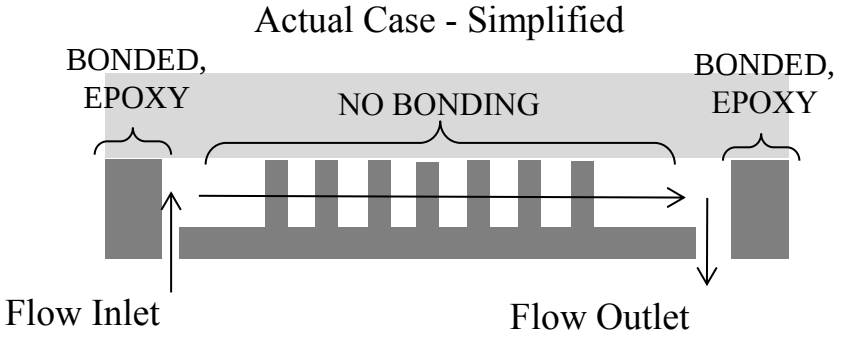

Figure 6.3 – Side view of cross-section to illustrate zones of bonding and non-bonding

The model geometry producing the results of Figure 6.4 is based on a simple 1 cm by 1 cm block with 500 μm of silicon and 700 μm of glass in which the interior section of silicon has been etched 100 μm. Symmetry is used to cut the sample in half and also allow for easy view of the internal response of the system. Table 6.1 has the material properties used for glass and silicon. The epoxy used to bond the edge of the device is not physically modeled. Under equivalent internal pressure loading of 700 kPa, the system bulges and develops maximum principal stresses in excess of 200 MPa as seen in Figure 6.4. This stress concentration at the periphery of the device is consistent with the failure observed in experiments and in Figure 6.2b for which cracking occurred around the edge of the flow zone. In an effort to reduce this stress concentration, additional modeling is conducted for scenarios where the geometry is externally clamped and where silicon support pin fins are added to the internal flow zone and assumed to be bonded to the glass.

Table 6.1 – Material properties used for silicon and glass

Parameter	Silicon	Glass
Model Type	Elastic Anisotropic	Elastic
Modulus, E	C_{11}: 166 GPa C_{12}: 63 GPa C_{44}: 80 GPa	70 GPa
Posson's ratio, v	0.28	0.16

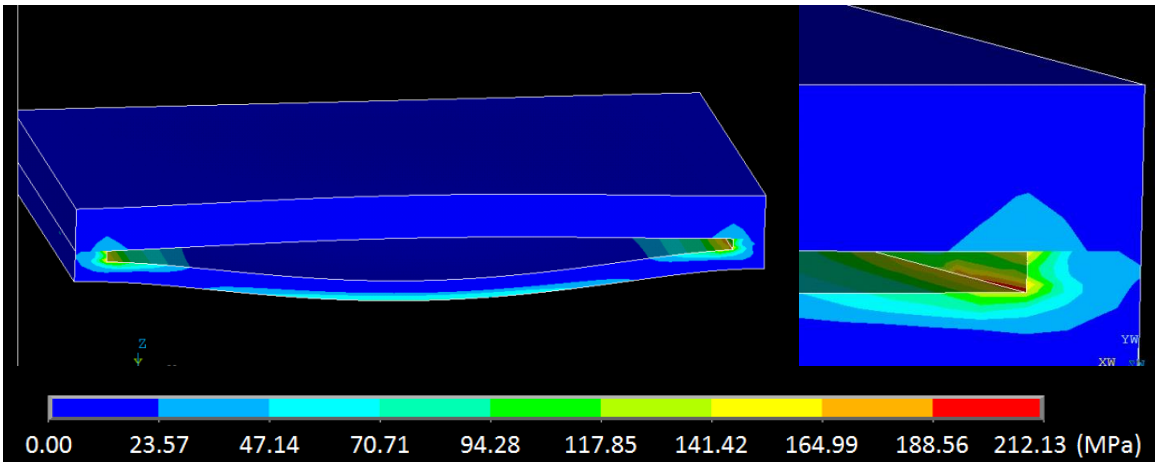

Figure 6.4 – 3-D simplified model for unrestricted pressurized microfluidic cavity

The same model is reworked to have a 1 mm x 1 mm zone in the center (reduced by 50% for this symmetric case), which is not allowed to expand in the outward direction from the cavity of the flow zone. In this case for the same mesh size, the stresses on the periphery of the device at the corners reduced to approximately 130 MPa (Figure 6.5), but stresses arise near the clamped section which reach 175 MPa. While this is a reduction in stress for the same mesh size, external clamping is not necessarily desirable as it requires additional packaging and can restrict view of the device. For this thermal test vehicle design, one function of the glass cap is to allow visualization of the flow zone during operation. External clamping on the glass side obstructs view of the flow.

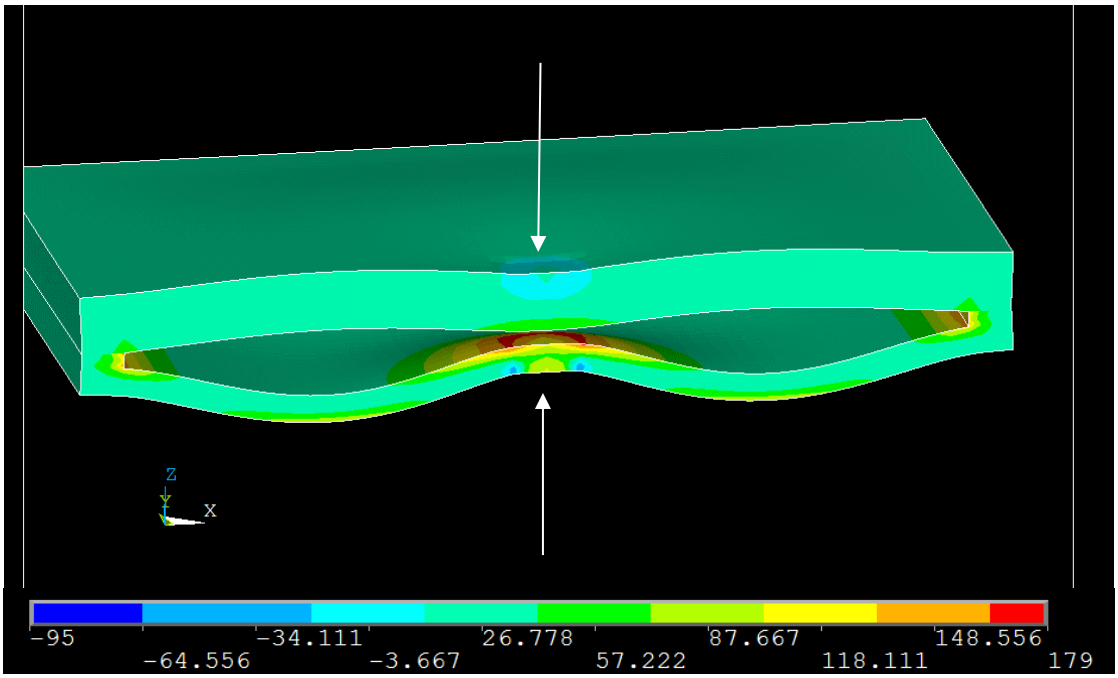

Figure 6.5 – 3-D simplified model for pressurized microfluidic cavity with external clamping

The second alternative is to develop a method to bond the glass cap to internal support features of the silicon rather than only around the periphery. Using the same model setup, the geometry is slightly altered to include support pins (1000 μm diameter silicon cylinders) that are mated with the bottom silicon plate and the glass cap. Figure 6.6 demonstrates the results of solving this model, keeping all other conditions the same. While additional stress concentrations arise on the new supports, the overall maximum principal stress is reduced to 80 MPa. Because of this improvement, the generation 1 device is redesigned for generation 2 to include mechanical support structures in the interior flow zone (along with other changes to thermal-fluidic and electrical properties). Alternative bonding techniques are explored to make use of these support structures.

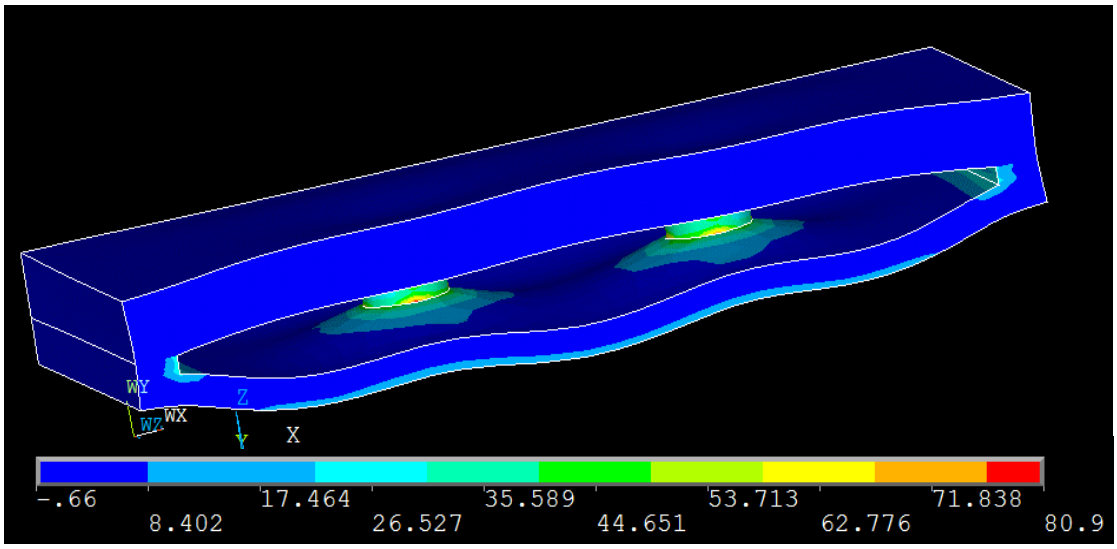

Figure 6.6 – 3-D simplified model for pressurized microfluidic cavity with internal support pins

6.2 Generation 2 Mechanical Modeling for Epoxy Bonding

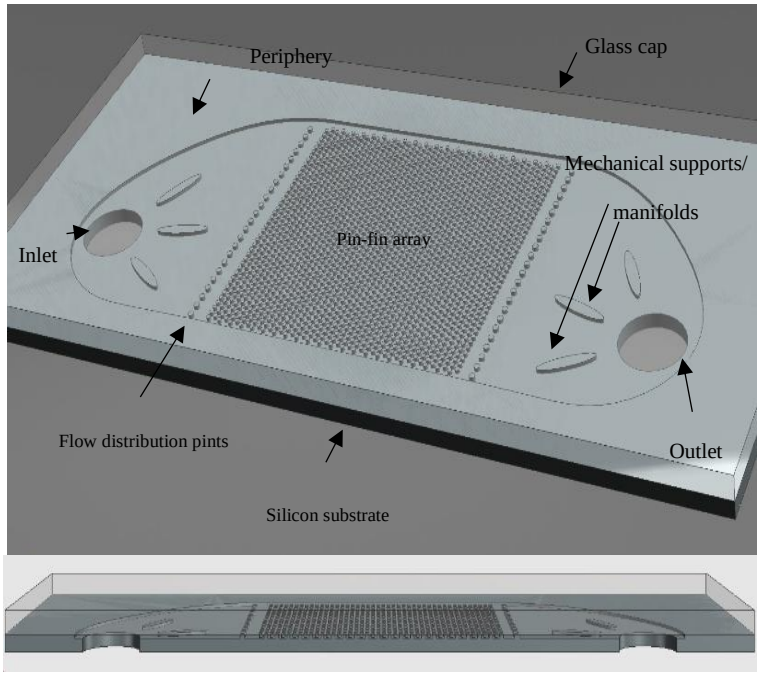

Figure 6.7 – Schematic of generation 2 thermal test vehicle microfluidic pin-fin array

The generation 2 main design premise explained in Figure 6.7 generally includes a substrate and a cap. This is the general fabrication process used to fabricate the similar designs of generation 1 and 3. In this approach, the proposed configuration has a silicon substrate with an array of micro-pin fins etched into it for improved surface area. The entirety of the open face of the silicon substrate is capped with a capping glass layer. For the epoxy bonding case, the silicon substrate and the glass capping layer are bonded to each other using epoxy that is dispensed around the larger flat face on the periphery of the coupons.

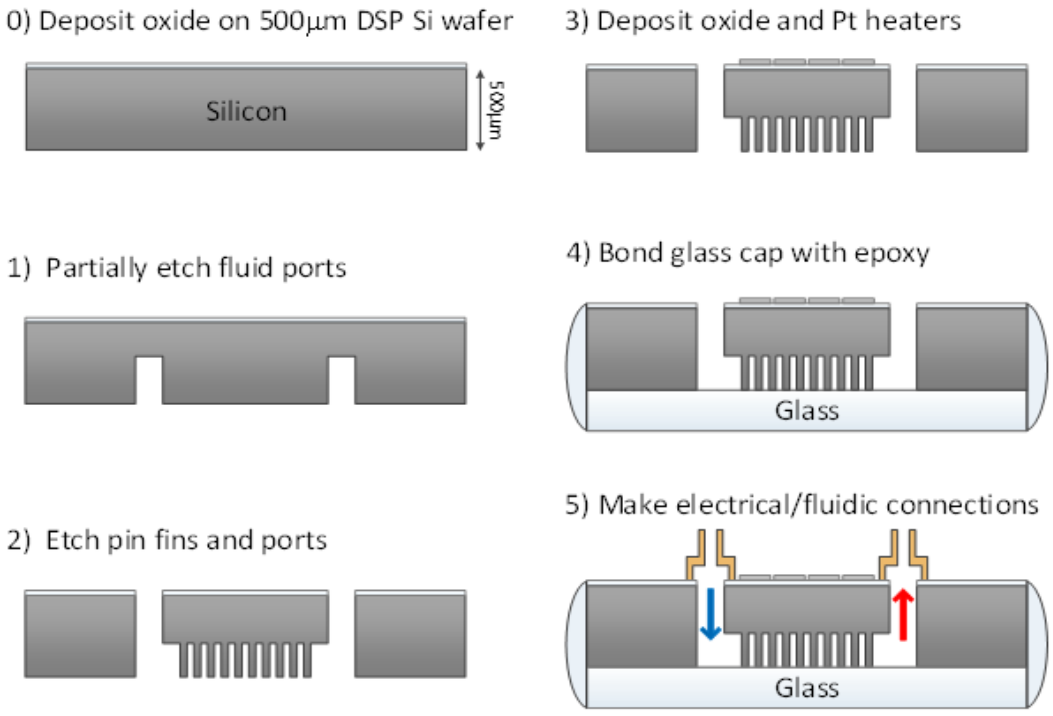

Figure 6.8 – Steps for fabrication of Thermal Background Cooler Test Vehicle (Design B)

The fluid inlet and the outlet are etched into silicon substrate and span a length of about 25 mm. Mechanical supports may also be built in to be able to direct the flow toward the micro-pin array and provide structural support to the assembly. For improved heat transfer over the active area, an array of pin-fins occupies the 1 cm^2 square region in the center of the design. Also, a single row of flow distribution pins can be added to the inlet region to ensure uniform flow through the micro-pin array. Two pressure ports are also present in the assembly, which allows for the fluid pressure to be measured before and after the micro-pin fin array. For reference, the entire sample is approximately 30 mm long, 14 mm wide, and 1.3 mm thick.

For a baseline, a 3-D structural model is developed using ANSYS® Mechanical based on the general design for generation 2 in Figure 6.7. The geometry is constructed using a bottom-up process for complete control of geometry, mesh density, and mesh direction. Areas are generated to form various geometric entities such as the coupon geometry, flow boundaries, inlet/outlet ports, supports, flow distribution pins, and pin-fin array. These areas are meshed and then extruded out of plane to form a 3-D system of elements to build-up the known geometry from this device design. For model integrity and flexibility in further tests, the entire model is setup to be parametric in nature and easily modifiable in terms of geometric size and mesh density. The geometric parameters in Table 1 are used for this model case.

Table 6.2 – Geometric parameters for modeling of Device B

Geometric Parameter	Value
Chip Length	2.5 cm
Chip Width	1.4 cm
Pin Diameter	150 μm
Pin Pitch	225 μm
Array Length	1 cm
Silicon Thickness	500 μm
Glass Thickness	700 μm
Gap Height	100 μm

In developing boundary conditions for this model, the epoxy bonding technique is a primary consideration. The initial experimental tests were performed using samples for which a 500 μm thick silicon is bonded to a 700 μm thick glass using epoxy around the periphery. Figure 6.9 shows a lighter blueish area that illustrates the peripheral area where epoxy is applied for bonding. This information is necessary for selecting which nodes are connected and which are not. The mating nodes at the bottom of the glass cap and the top of the silicon substrate are merged together where epoxy is present. For the tops of the pin-fins and other structures, no merging is allowed. This mimics the lack of bonding for those faces. Thus, this condition simulates the case when epoxy bonding only occurs on the periphery of the device.

To study the pressure-induced failure, all free faces of the flow space are subjected to the applied fluid pressure of 800 kPa that was observed to cause failure during experiments with the earlier generation design. A fixed condition is also applied on the far-left edge of the geometry at a single node to prevent rigid body motion and rotation.

This constraint condition is sufficiently far from the zone of interest as to avoid introducing any significant errors while still preventing rigid body motion from occurring. In addition to the mentioned geometric parameters, constraints, and loading conditions, the necessary material properties are also the same as used previously from Table 6.1.

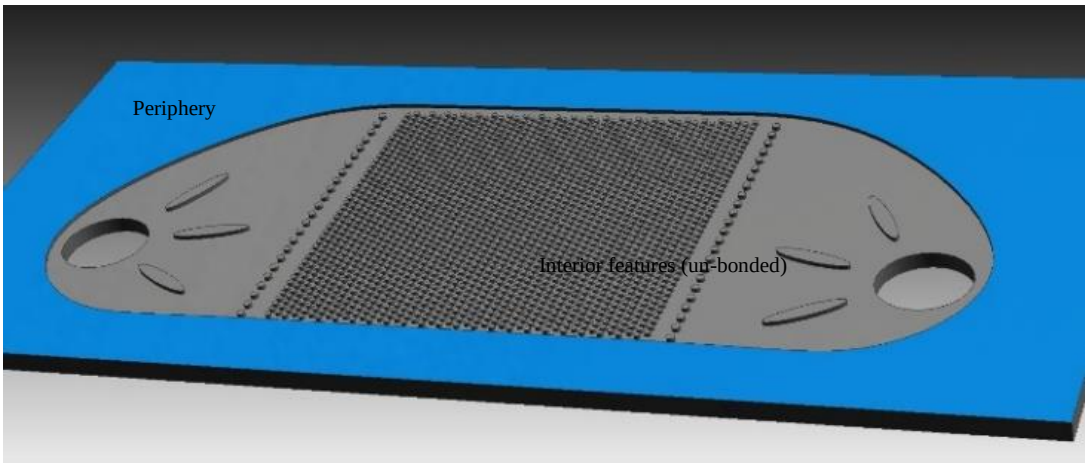

Figure 6.9 – Model illustration of bonding around the periphery of the device (blue) but not on any interior features

Based on this setup and specified boundary conditions, the model is well posed and can be solved. With the number of structural elements in excess of half a million and using three translational degrees of freedom, the model takes approximately six hours to solve on a six-core processor for the default mesh size. The displacement contours are shown in Figure 6.10 (exaggerated scale) with units of microns. Due to the lack of bonding on the interior features, both of the larger glass and silicon faces are allowed to flex outward. Though silicon has a slightly greater elastic modulus than glass, the maximum displacement occurs near the center of the silicon substrate. This is due to the fact that the substrate was thinned to approximately 400 μm versus the 700 μm thick glass, making it less stiff compared to the glass capping layer. The internal pressures cause the design to

act like a pressure vessel. The thick glass cap does not bend as much due to its higher flexural rigidity.

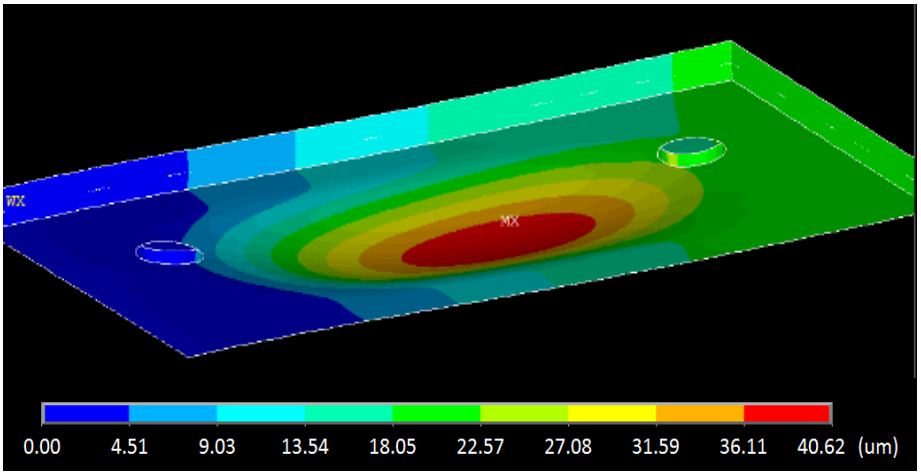

Figure 6.10 – View of maximum displacement on underside of silicon for peripheral bonding scenario; exaggerated visual

While the displacement plot is helpful for understanding the nature of the model results, it is more important to consider the principal stresses arising due to this load case. Stresses develop near the edge of the flow space due to this flexing action of the silicon and glass. The first principal stress contours are shown in Figure 6.11. These results show that high internal pressure causes high bending stresses near the edges of the micro-gap for both the silicon and glass sides of the microchannel. On the silicon side, which was observed to fail in experiments, the stress reaches approximately 470 MPa near the edge of the flow zone. At this corner where the silicon has been etched, the stress concentration could be causing crack propagation beginning at existing small crack defects. As the fracture toughness of silicon is in the range of 0.7 to 1 MPa$\sqrt{m}$ [31], the silicon substrate will fracture at these high stresses considering a flaw size on the order of 5 µm. Such

defects could come about due to fabrication processing such as etching or could be preexisting cracks from initial wafer manufacture.

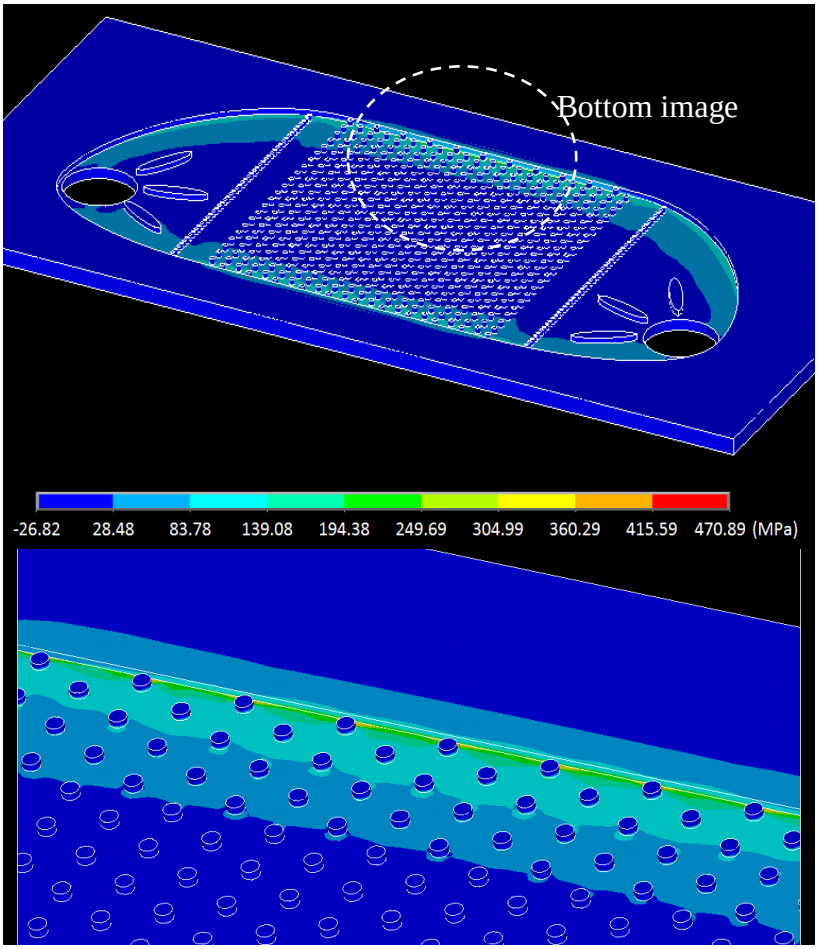

Figure 6.11 – Cut view of first principal stress in silicon side of model for peripheral bonding scenario; global view (top) and zoomed view of top silicon edge (bottom)

As observed in multiple experiments, several of these epoxy bonded samples fractured around 800 kPa in a similar fashion. To mitigate this failure, other bonding techniques may be warranted. Rather than using epoxy bonding, an alternative, anodic bonding, may be used to bond glass and silicon wafers through the application of compressive pressure, temperature, and voltage. This approach can potentially bond the faces of the silicon pin-fins to the glass as well, thus it is also valuable to perform structural

modeling for the case when all interior faces are bonded to the capping layer, to see what improvement this will have on device reliability.

6.3 Generation 2 Mechanical Modeling for Anodic Bonding

Based on the baseline model setup used for epoxy bonding, one can readily establish a similar model for the case of anodic bonding between silicon and glass. The prime difference between these models is purely related to the selection of elements that are merged. Where only the elements on the peripheral top faces are merged for the epoxy case, all the interior top faces of the pin fins and manifolds are also be merged for anodic bonding. This is illustrated by the faces highlighted in blue in Figure 6.12. For this model one can infer that the bulging action of the free silicon and glass areas will be more constrained, and stresses will no longer only arise along the corner edge of the silicon or glass, but also around the edges of other bonded features.

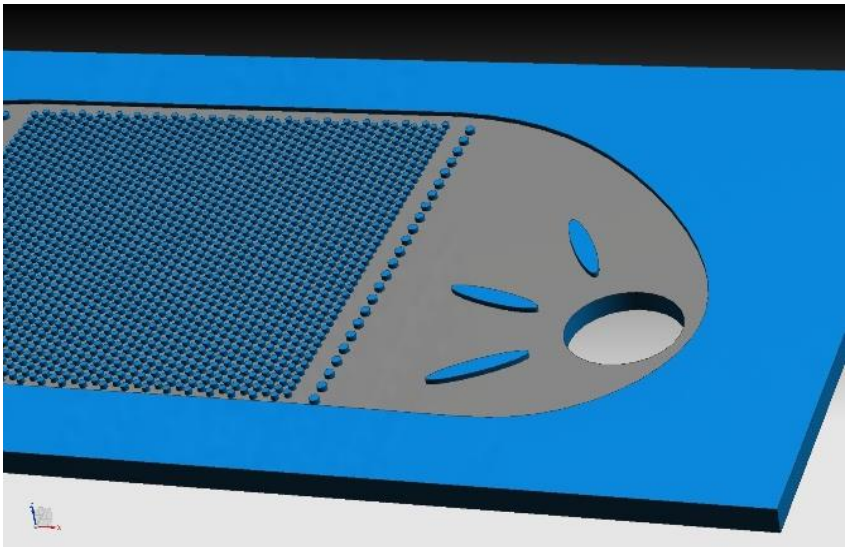

Figure 6.12 – Model illustration of surface faces assumed to be bonded (blue)

This model setup includes the same pressure loading condition within the cavity, the fixed constraint at one far edge away from the flow zone, and the same material and geometric values are utilized. For a similar loading condition of 800 kPa, the stress field now is significantly different as shown in Figure 6.13.

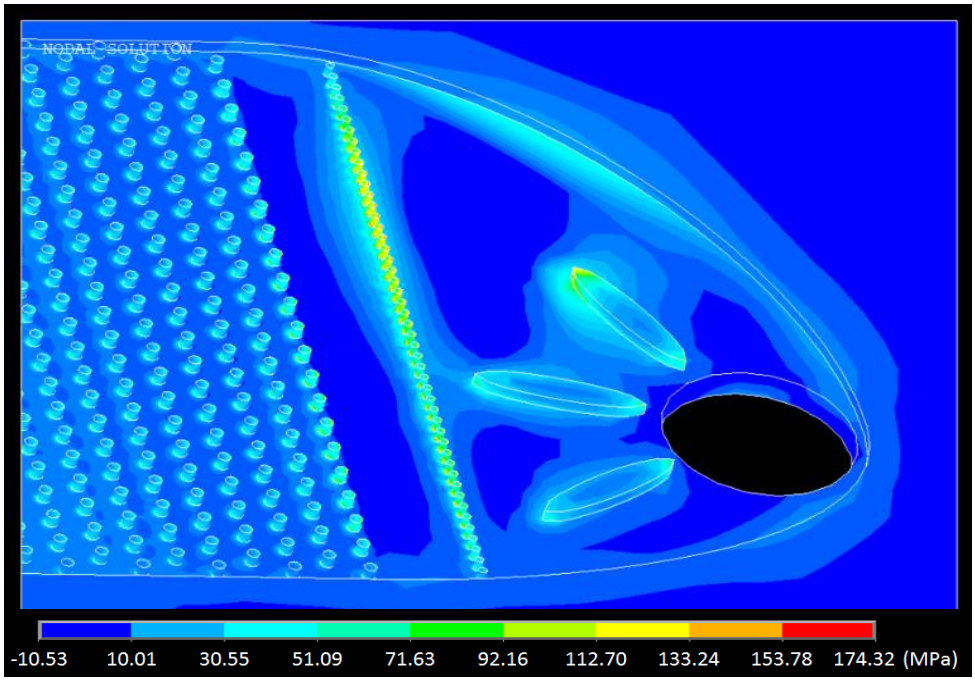

Figure 6.13 – Principal stress in silicon side for ideal bonding case

The maximum observed principal stress has been reduced from approximately 470 MPa (epoxy bonding) to 175 MPa (anodic bonding) for the same mesh size. The stress concentrations also shifted from the corner edges of the overall flow domain to be focused on smaller interior features. While this is not a clear indicator that this design and bonding approach is the final solution for this high-pressure design, these modeling results do suggest an improvement in tolerable experimental pressure could be observed.

6.4 Generation 2 Dye and Pry Techniques

With the new information from the finite-element modeling, additional tests are conducted with samples fabricated and bonded using anodic bonding. A dye-and-pry method is developed and utilized to visually evaluate the results of an experimental pressure test across a range of internal pressures. Dye-and-pry techniques are commonly used for identifying cracks and defects in solder joints in microelectronic packages, e.g. [33, 34], where a dye is forced into cracks in the solder joints and then allowed to dry. Afterwards the sample is pried open, the cracks can be observed by visual inspection and in some cases cross-sectioning is used to fully measure the depth of cracks and dye penetration. In the experiment presented, a similar technique is used for the microfluidic sample assembly where a green working fluid, triarylmethane dye, is pumped in using a syringe pump while a pressure transducer provides in situ pressure data. The outlet port of the device is sealed to create a closed system that can be pressurized successfully. A mechanical clamp gradually actuates the syringe pump compressing the liquid within the closed system. The goal of this test is to determine the pressure at which the device fails and to record where cracks occur through visual inspection of the penetration of the green dye. Additional concerns with this test include fluid leakage, depth of field, levelness of the sample beneath the microscope, and safety of the working environment at failure point.

For reference, a model image of a failed sample is shown in Figure 6.14. This shows the view direction of the other microscope images that are provided. Figure 6.15 shows an image before failure of the device from the direct downward direction through the glass cap to see the top faces of the pin fins. As seen, the sample has an array of micro-pin fins with a diameter of 150 μm as well as flow redistribution pins of a similar diameter

prior to fluid entry to the main array. As the fluid pressure is gradually increased, the sample breaks when the fluid pressure reaches 800 kPa, although the glass cracks in addition to the silicon. This maximum pressure exceeds the range of pressures previously observed for epoxy bonding, but it is still only about a 15% increase over the 700 kPa previously recorded.

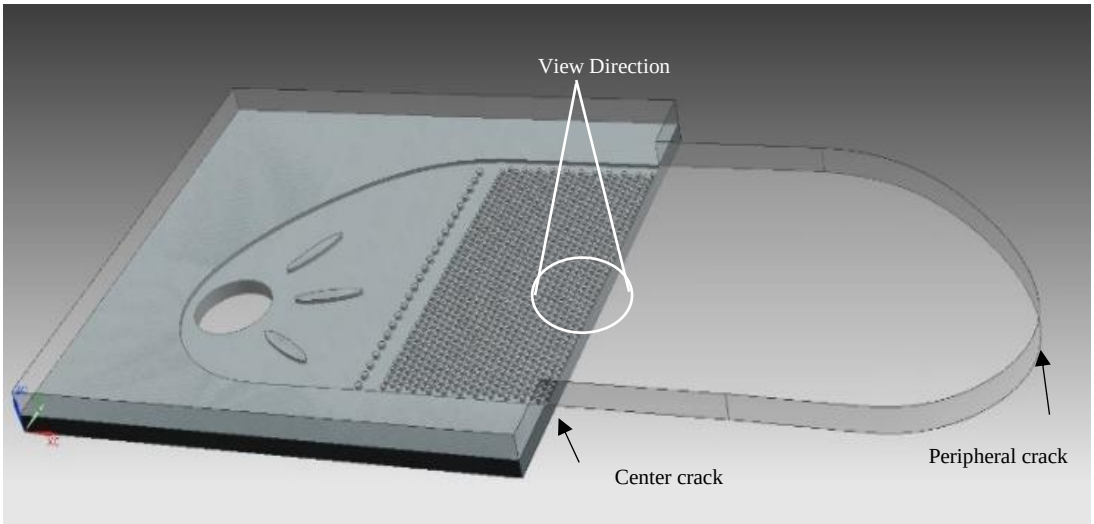

Figure 6.14 – Model of broken sample after attaining maximum pressure

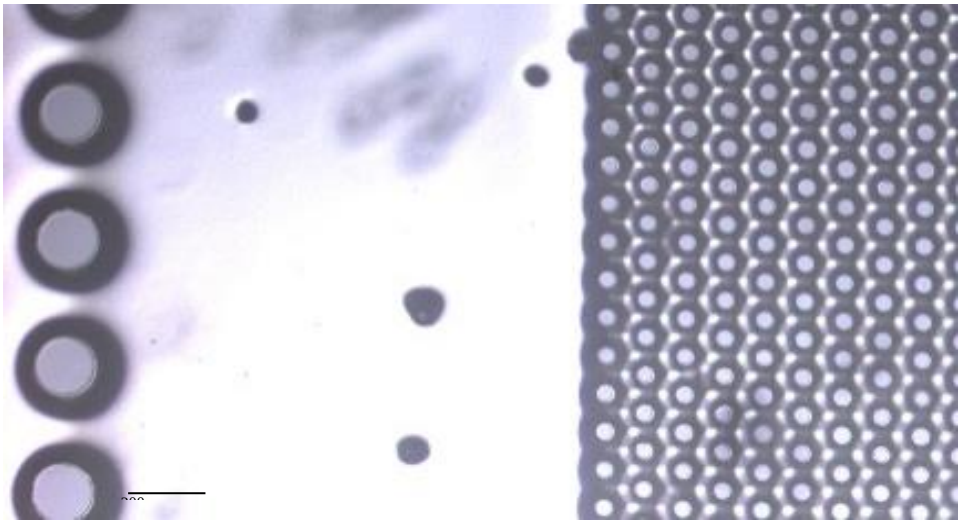

Figure 6.15 – As-fabricated-and-assembled sample before fluid pressure test

Immediately after failure, the sample was visually inspected using the microscope setup since the dye remains in place and begins to dry. This reduces the risk of destroying the remainder of the sample due to handling in between sample unload and reload steps. As illustrated in Figure 6.14, sample fracture occurs around the periphery where the glass cap has cracked around the edge of the flow domain. The silicon also failed and then broke off for the sample in question. In other samples the silicon side of the device remains fully intact while the glass cap cracked around the periphery of the flow domain as in the example sample. This sample presents a unique opportunity to view a section of the silicon pin-fin array that still is protected by the section of the glass cap.

As seen in Figure 6.16, even after much of the green dye leaves the open flow zone, there appears to be green dye remaining trapped between the glass cap and the top of the silicon pin fins. This could suggest there was significant separation between the top faces of the silicon pin fins and the glass cap to allow the green dye to fill some space and remain trapped.

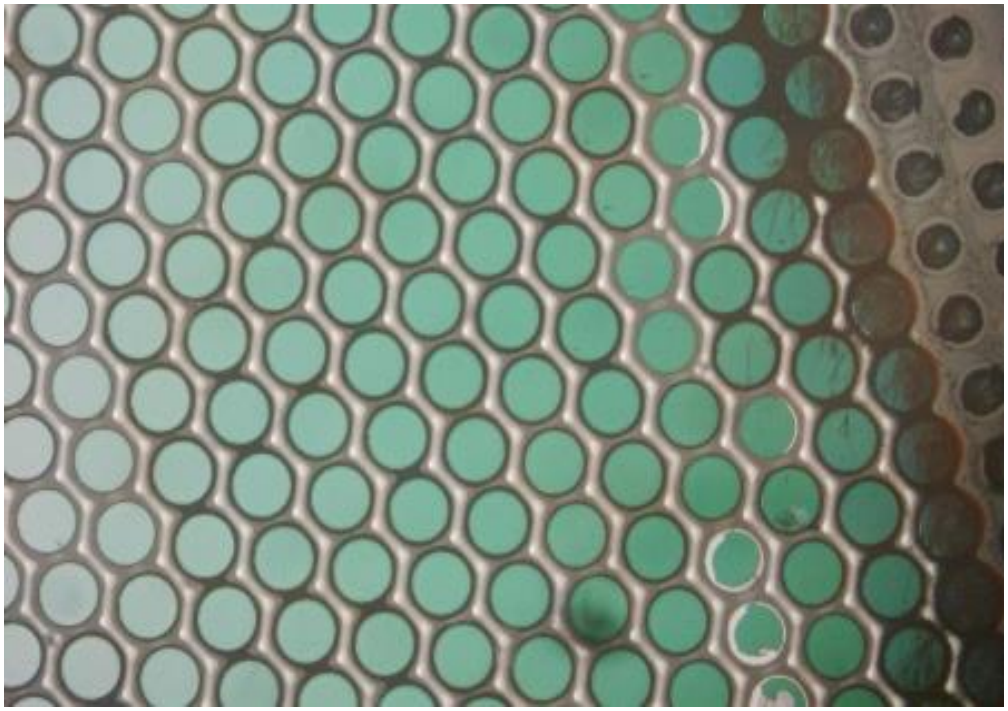

Figure 6.16 – 150 µm diameter pin-fin heads after fracture (covered by glass and dye)

Still it is significant to note that no green dye was observed to have penetrated between silicon and glass at these locations during the ramp up of the pressure, only after catastrophic fracture; it was not a gradual separation of glass cap from silicon pin-fins. In addition, the intensity of the green color on the pin-fin faces is highest near the edge of the main crack where the bottom silicon split. The color intensity decreases away from the primary crack zone. This indicates that even though cracking is occurring, the crack opening between pins and cap near the edges of the sample does not open as wide as the pins near the center of the sample. This is consistent with the bulging profile observed for the epoxy bonding case where no internal bonding is considered for the interior features.

Based on the timing of the dye flow and how it is trapped after catastrophic failure occurs, one can develop a reasoned hypothesis about the failure process. First, the anodic

bonding fabrication process between silicon and glass is successful to some degree; dye does not penetrate between silicon and glass until pressures reach the critical failure pressure. Second, at the point of failure, a localized zone of pin-fin tops develops complete cracks between silicon and glass. After this point, that localized zone becomes more compliant since silicon and glass are now not bonded and are allowed to bend and bulge outward further given the same pressure load. This increases the stress on the neighboring pin-fins, causing these neighbors to fail and so forth. And thus, the localized zone of failure catastrophically expands, as additional pin-fins rapidly separate from the cap. Once a critical number of pin-fins in the array failed, there will be enough energy available for cracking and failure at the edge of the flow zone in the glass cap, fully relieving the pressure load to ambient conditions.

This hypothesis would support the use of anodic bonding in future fabrications, but there may be a need for optimizing the parameters of the bonding process to try to increase the integrity of the bonds or possibly adding additional mechanical supports. To substantiate this hypothesis, additional ad hoc images and measurements are taken to try to establish the success of anodic bonding. Figure 6.17 is a microscope image of the same zone from Figure 6.16, but the dye has had enough time to dry. The dye residue has clotted and clings to cracks in the structure and clearly shows that the crack surfaces on most pin-fins have contours. One could argue that this roughness is in direct contrast to the smooth pin-fin faces that existed before bonding. If the silicon pin-fins were never bonded to the glass, these contours would not exist. In order to further investigate the crack profile of the pin fin tops, laser profilometry is used to scan across the tops of the pin fins.

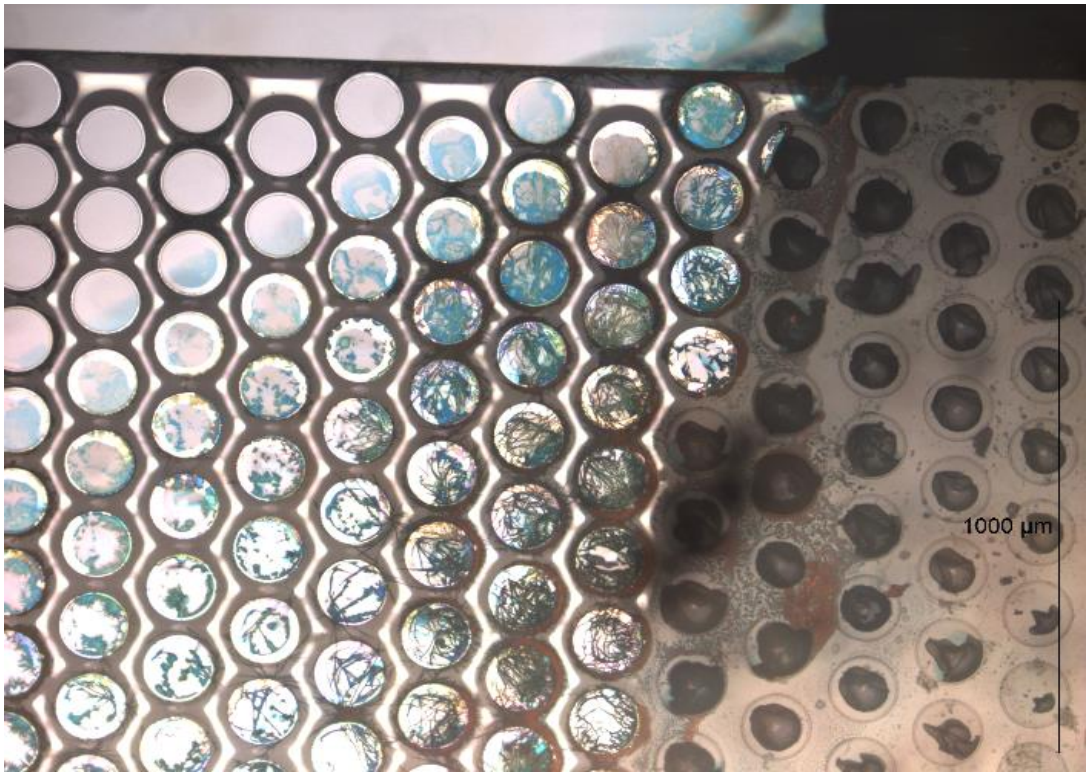

Figure 6.17 – Dried sample after failure showing dried dye fluid

Since this particular sample split along the middle of the silicon substrate and also cracked around the edge of the glass, it formed two mostly intact specimens upon completion of the experiment. The first of the two half-specimens has been discussed, but the second half of the failed device is also useful because there is no longer a glass cap covering the silicon pin fins. It has broken off and remains with the first half-specimen, allowing for open investigation of the top of the silicon micro-pin fins. Using a profilometer, profile scans are taken for several of the standing pin fins. Figure 6.18 shows a microscope image with the line that was scanned and also the profile measured into the page.

In the visual image of Figure 6.18, the tops of the cylindrical, silicon pin fins are in white, but appear to have some other material applied or removed from the top. The profile

measurement indicates that a dome-like structure adhered to the top of a vast majority of these pin fins. This section of glass that remains adhered to the top of the silicon pin fins is approximately 5 µm at the thickest point. Where the base of the residual dome material attaches to the silicon, it is approximately 100 to 130 µm in diameter versus the full 150 µm diameter of the pins. This is clear evidence that anodic bonding is at least partially successful in achieving bonding for even these small interior features.

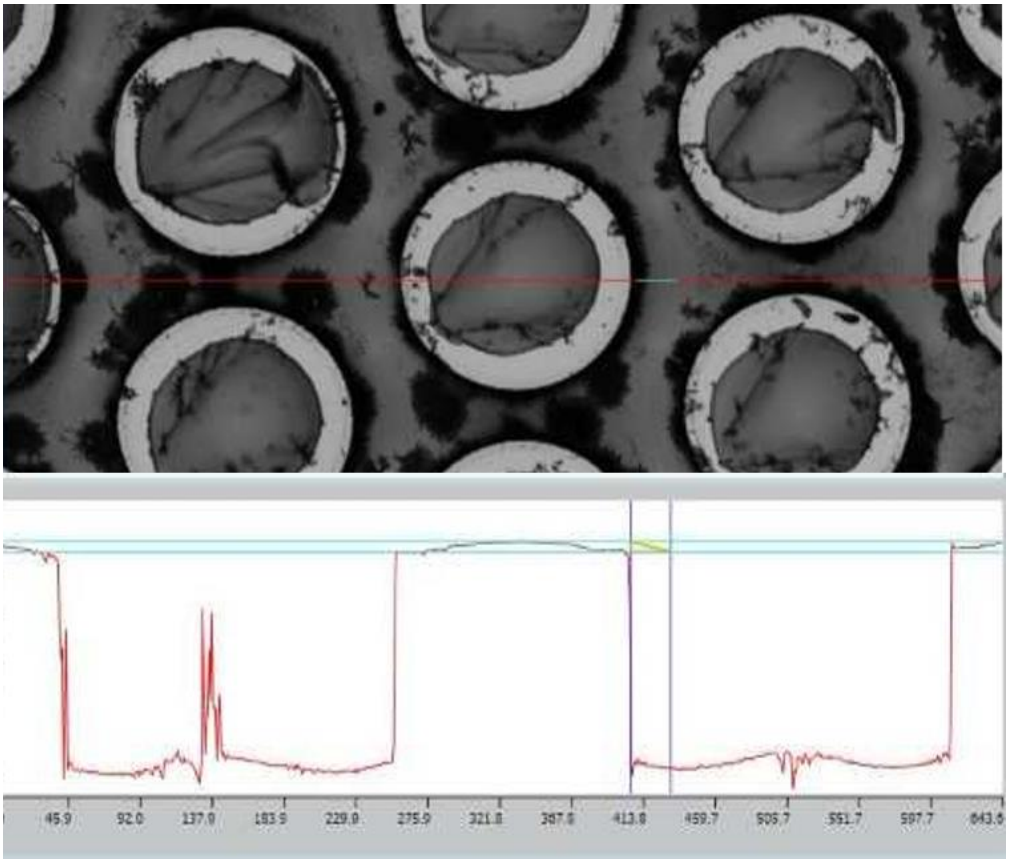

Figure 6.18 – Measurement of pin fin profile with profilometer

Based on this study, new designs and new anodic bonding parameters may be considered for improving bond strength. Additional supports and manifolds could also improve the overall structural integrity of the design. Additional testing using dye and pry

type techniques may be able to isolate the central point of failure in other samples and thus indicate where stronger bonding and larger supports are required. As a final consideration, additional designs may include more exotic pin-fin geometries other than purely cylindrical shapes. These designs also benefit from both modeling and experimental dye and pry testing.

6.5 Generation 3 Predictive Study and Mechanical Modeling

Using the generation 2 mechanical model for epoxy bonding, an additional study is performed to determine the trend in principal stress for support spacing values at different pressures. For the same roughly 800 kPa loading condition (adjusted to 825 kPa to match updated experimental data), additional supports are placed in the inlet and outlet plenums at known spacing distances. The model maximum principal stress is recorded for various spacings at 825 kPa pressure loading. In addition, the model is solved for the same support spacing values for the target pressure of 3300 kPa.

With the resultant model data, the comparative plot shown in Figure 6.19 is developed. Previous models and experimental results suggest failure is likely occurring for stresses around 200 MPa (and defects are around 5 μm in radius for fracture toughness of 1 MPa$\sqrt{m}$). A 200 MPa critical stress value (for the consistent mesh size of 5 μm) is included on Figure 6.19. The generation 3 device is designed to have supports spaced at maximum of 1000 μm apart to ensure that failure of the device does not occur until pressures reach an excess of 3300 kPa. In this way the model results of Figure 6.20 for a generation 3 design are used to predictively influence design prior to device fabrication to ensure mechanical reliability.

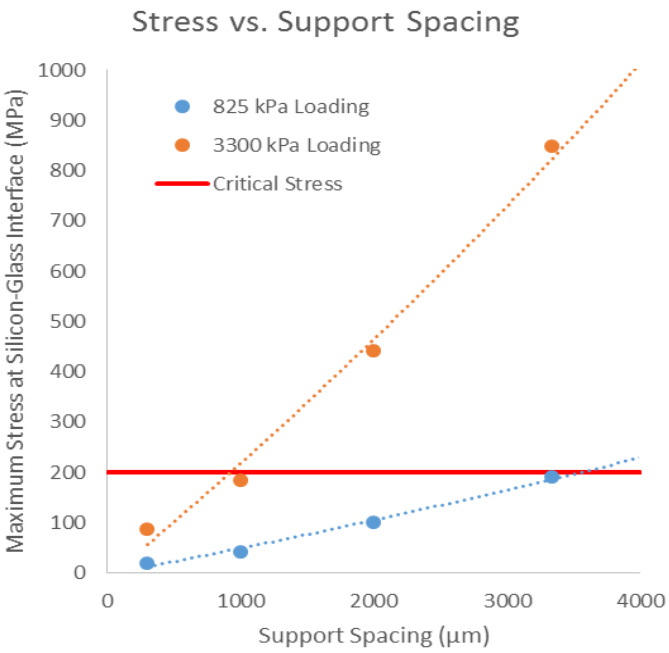

Figure 6.19 – Results for finite element model which governs support spacing selection

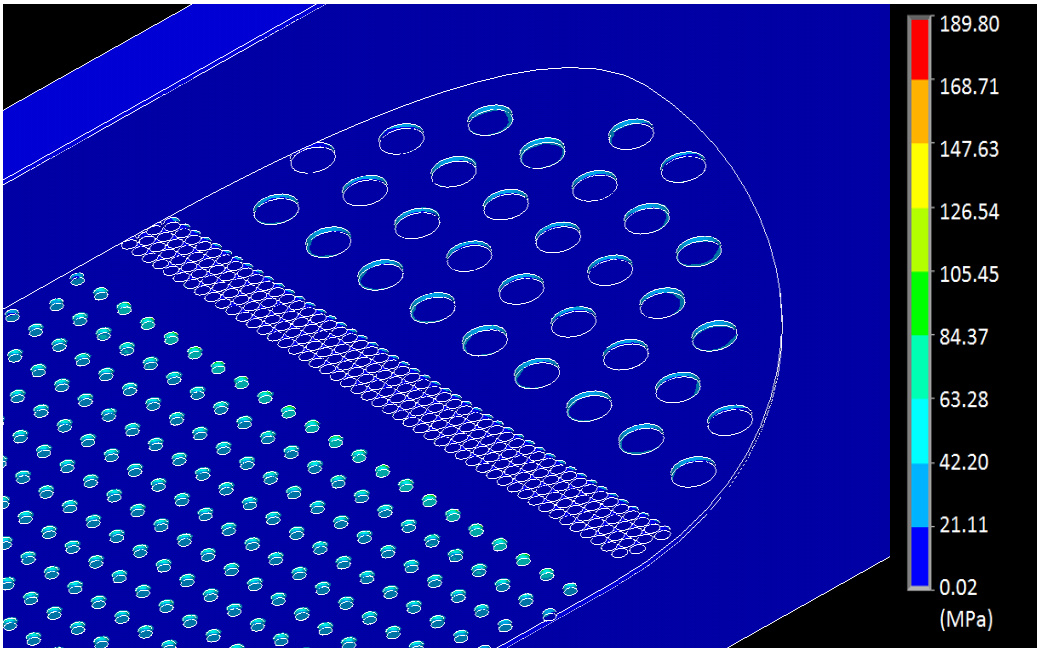

Figure 6.20 – Maximum principal stress results for Thermal Test Vehicle Generation 3 at 3300 kPa (cut-view)

6.6 Alternative Designs: Hotspot Cooler Modeling

Alternative designs such as the dedicated hotspot cooler device provide opportunities to expand the application of mechanical modeling to other geometries. A brief study is conducted for this dedicated hotspot coolerb which regularly operates with internal pressures in excess of 3000 kPa and potentially up to 6000 kPa. These high pressures allow for high quality, two-phase flow and absorption of heat rates in excess of 5 kW/cm^2 from localized areas that are 200 µm x 200 µm. Using a mechanical model similar in setup to those previously discussed, the hotspot geometry is loaded with pressures up to 3000 kPa. The results indicate that at such reduced length scales (10s of microns instead of 1000s of microns) the structure is effectively well supported and maintains low stress levels. [12, 25, 37]

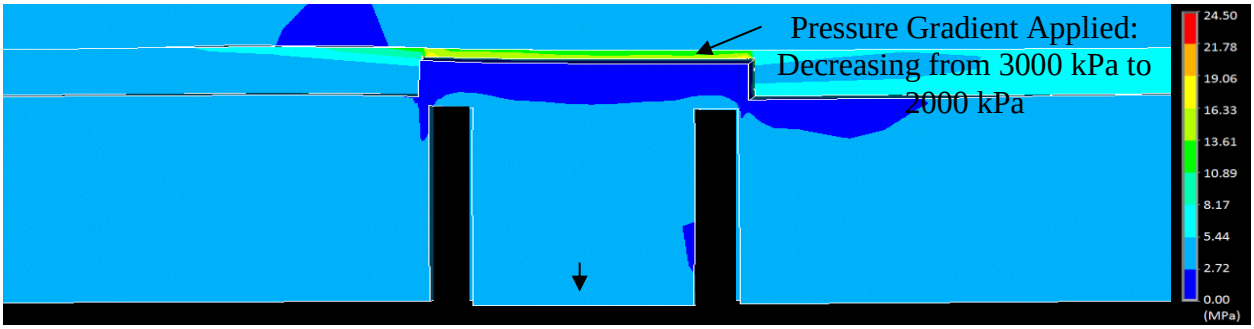

Figure 6.21 – Hotspot design results: first principal stresses during operation.

6.7 Alternative Designs: FPGA Liquid Cooler Warpage

Additional modeling and experimental measurements are included for another key design, a low-pressure, high-performance FPGA design [11], which has been fabricated

for low-pressure on-chip liquid water cooling. As such, it is important to determine how adding microfluidic pathways to the device affected its warpage in an otherwise nominal design. This example "Electrical Test Vehicle" is shown in Figure 6.22. The material stack-up and resulting experimental warpage map at room temperature are shown in Figure 6.23 and Figure 6.24. Due to decreased compliance of the bulk silicon after etching the microchannel, the overall system experiences a larger relative warpage (35% larger) than an un-etched device. Warpage is a significant consideration in standard microelectronic systems, and this experimental study suggests that it will be as great or more of a concern in future work for on-chip microfluidic system. [11]

Figure 6.22 – FPGA Liquid Cooler (Design C) developed for liquid cooling of an active device from industry as an electrical test vehicle

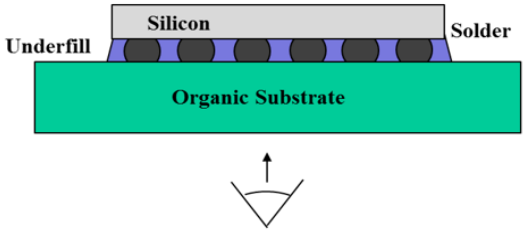

Figure 6.23 – Layout and experimental warpage view direction for liquid-cooled electrical test vehicle

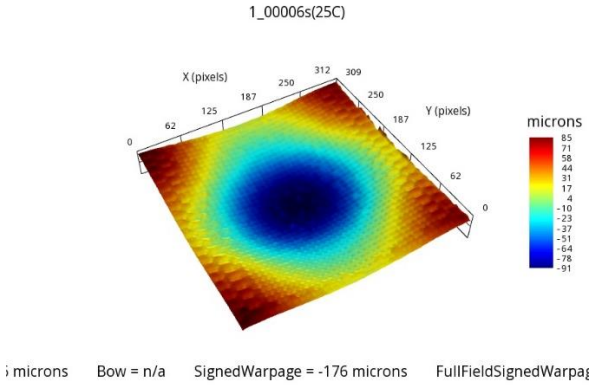

Figure 6.24 – Experimental warpage map for liquid cooled FPGA

CHAPTER 7. MECHANICAL MODELING FOR OPTIMIZATION OF PIN-FIN SHAPE AND SPACING

Though the pin-fin features native to this design have been shown to add some mechanical/structural stability, their primary purpose as elements for enhancing heat transfer should not be forgotten. The cylindrical pin-fin designs mentioned up to this point certainly add complexity for fabrication, but also increase heat transfer characteristics of the microchannel and also provide consistent mechanical strength when placed in proper locations. Changing the pin-fin design from cylindrical to a more exotic shape, such as a hydrofoil, is a natural progression for increasing heat transfer effectiveness while reducing the need to increase fluid inlet pressure and pumping power. While maintaining the overall design premise illustrated in the global architecture in Design B, hydrofoils can be used in place of the cylindrical pin fins populating the primary array of pins. Thus, an inlet flow plenum with supports precedes the primary array of hydrofoils, which is succeeded by an exit plenum with supports and an outlet. The inlet plenum and a section of the hydrofoil pin-fin array are shown in Figure 7.1. One concern is that by changing the shape of these smaller pin fins, there could be a significant negative effect on the reliability of devices at higher pressure.

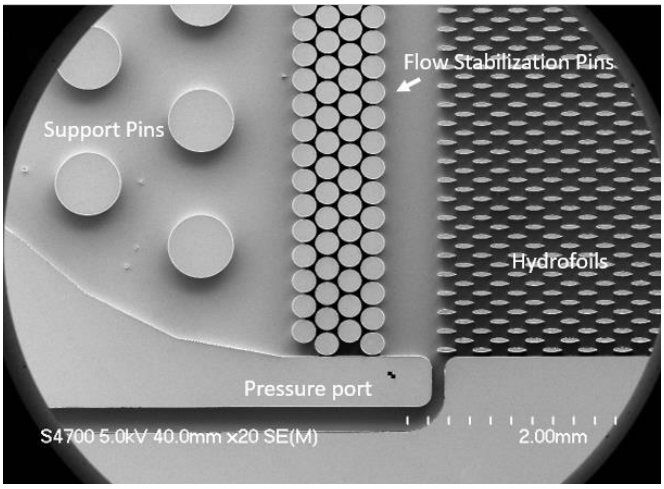

Figure 7.1 – SEM image of example device with hydrofoil micro-pin fin array

Because of the natural shape of a hydrofoil, which has a sharp radius of curvature at the tail section, it is possible for stresses to concentrate on this sharp feature, and thus decrease the allowable operating pressure. Figure 7.2 shows some of these hydrofoils, which have cracked and broken off. The cracking occurred during an experimental test at higher pressure which resulting in catastrophic device failure. It could be due to a number of factors, which include mechanical fracture at the tail of the hydrofoil pin fins.

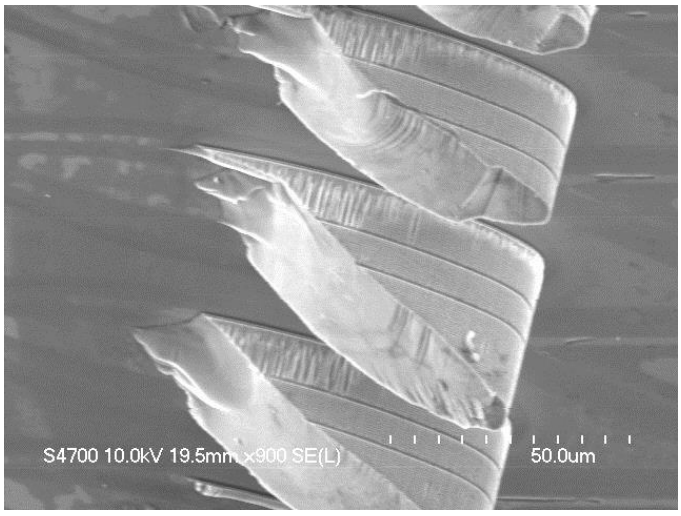

Figure 7.2 – SEM image of failed hydrofoil pin fins

7.1 Model Setup

The full design is very similar to the cases discussed in earlier sections, but from a modeling perspective the study can be expanded more effectively as a local model just focusing on the pin-fins. A 3-D structural model is developed through ANSYS® Mechanical for a key section of the flow domain where the array of small pin fins ends and opens up to the exit plenum with structural supports. This simplified geometry includes one column of hydrofoil pin fins and the adjacent support pins, as illustrated in Figure 7.3 and Figure 7.4. This illustrates the arrangement of pin fins beneath the glass capping layer.

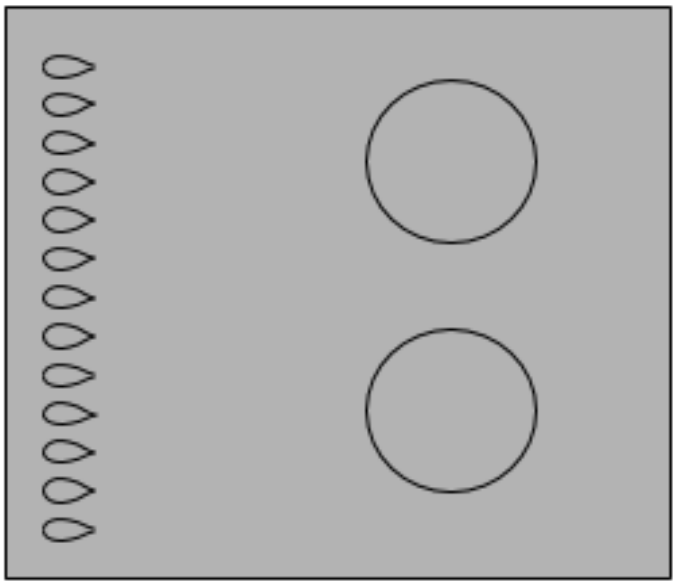

Figure 7.3 – Top view of the silicon features of local structural model for pin fins

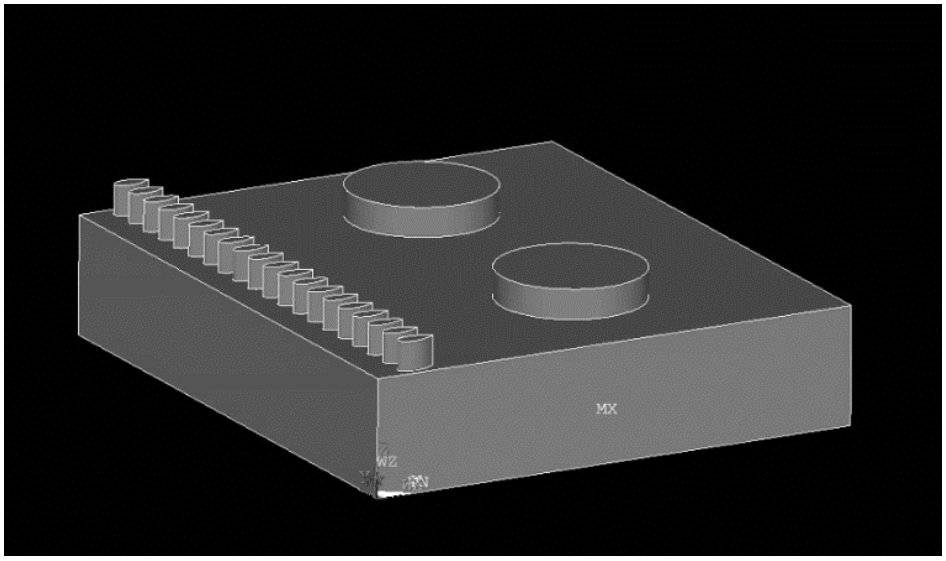

Figure 7.4 – 3-D view of silicon pin fins and supports with glass cap removed

In the initial case for this study, the smaller pin fins on the left of the design are assumed to be hydrofoil shaped, while the large support pin fins have a circular cross section. This case accents the effects of the sharp hydrofoil tail pointing toward the open, unconstrained space. This may be expected to exacerbate the stresses experienced by the hydrofoil compared to the standard cylindrical pin fin design. As shown in Figure 7.5, the full system is loaded with an internal pressure and constrained at one corner to prevent rigid body motion at a sufficiently far location from the critical points of interest. The internal pressure applied during experiments could range from 100 kPa up to 3000 kPa, but for the modeling considered in this case a pressure load of 900 kPa is applied on all internal faces to simulate the pressure that the fluid would apply on the solid boundary faces. Even though there will be a pressure gradient as the fluid would flow, this is not considered for the modeling performed on this local scale. The separation distance between the larger cylindrical bulk supports and the smaller hydrofoil micro-pin fins is the one key parameter of interest.

Using the geometric parameters listed in

Table 7.1, the geometry for the model is built. Bottom up construction is used to build the model, which involves creating 2-D cross-sections for the 3-D pin-fin shapes and then extruding the meshed cross-sections through the appropriate heights. Material properties are applied to the system as appropriate for the silicon pin fins and glass cap. The internal pressure load and constraints are applied and then the model is solved.

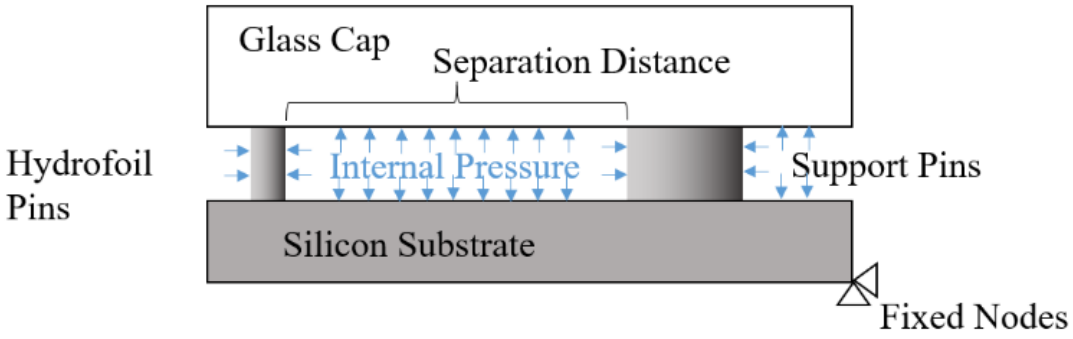

Figure 7.5 – Side view of structural model with boundary conditions and separation distance indicated

Table 7.1 – Geometric Parameters for Local Pin Fin Model (Case A)

Parameter	Value
Width/Length Model	3 mm
Diameter Support	500 µm
Length Hydrofoil	100 µm
Width Hydrofoil	40 µm
Pitch Hydrofoil	100 µm
Separation Hydrofoil-Support	1500 µm

7.2 Model Initial Results for Case A

As the system is the same brittle material set of glass and silicon, the key stress to examine is the first principal stress. Example contour plots of the first principal stresses for the geometric case are shown in Figure 7.6, Figure 7.7, and Figure 7.8. This is the characteristic case for a 10 μm pin fin mesh size. The stresses observed where silicon meets glass at the top of the pin fins reach 133 MPa for this mesh size and for the pin fins near the boundary of the local model. The hydrofoil pin fin tails are the solid features nearest to the unconstrained zone; thus, these features must accept a majority of the pressure loading acting on the exposed faces of the unconstrained zone. Due to the large separation distance between the hydrofoil pins and the support pins, the pressure acting on the unconstrained zone acts across a large moment arm increasing the load which must also be absorbed by these features. Similar to a cantilever beam simply supported at both ends with a uniform load in the middle, this situation illustrates how a separation distance (the length of the beam) amplifies the stress at the concentration point as the beam flexes. In this case the hydrofoil tail is the concentration point which is subjected to an even higher stress concentration as the geometry of the tail tapers down.

For reference, 89.4 MPa is the approximate maximum stress on the silicon side of the model where silicon pin fin's base is attached to the silicon substrate. The interior hydrofoil tails experience smaller stresses of 103 MPa at the silicon-glass interface and 73.5 MPa at the silicon pin fin base versus their counterpart values at the boundary. These characteristic stresses are indicated directly on Figure 7.8.

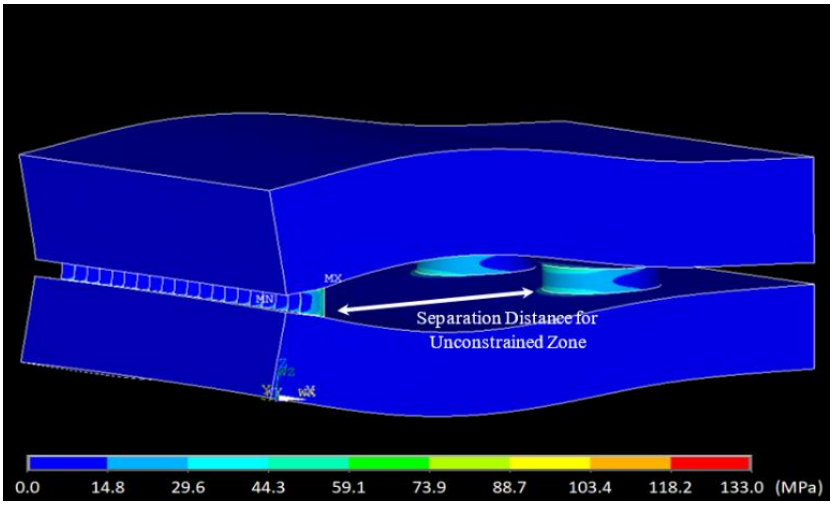

Figure 7.6 – First principal stress results for 1 MPa pressure loading (Case A)

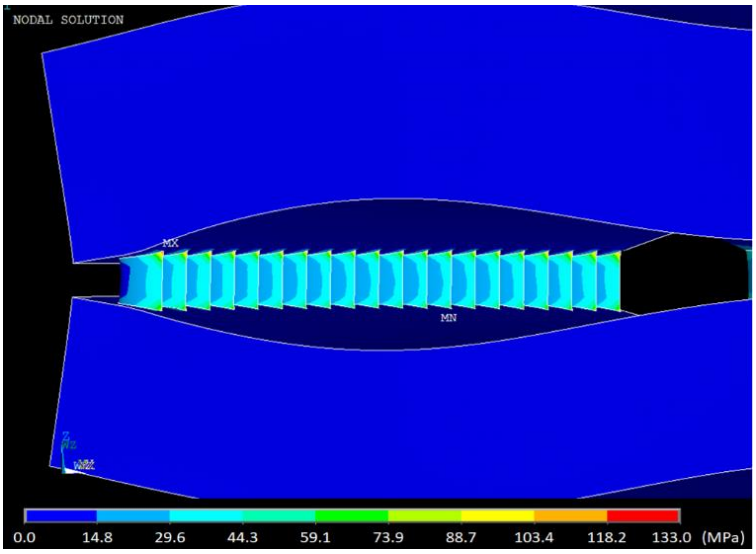

Figure 7.7 – Rotated view of hydrofoil pin fin tails facing the unconstrained zone

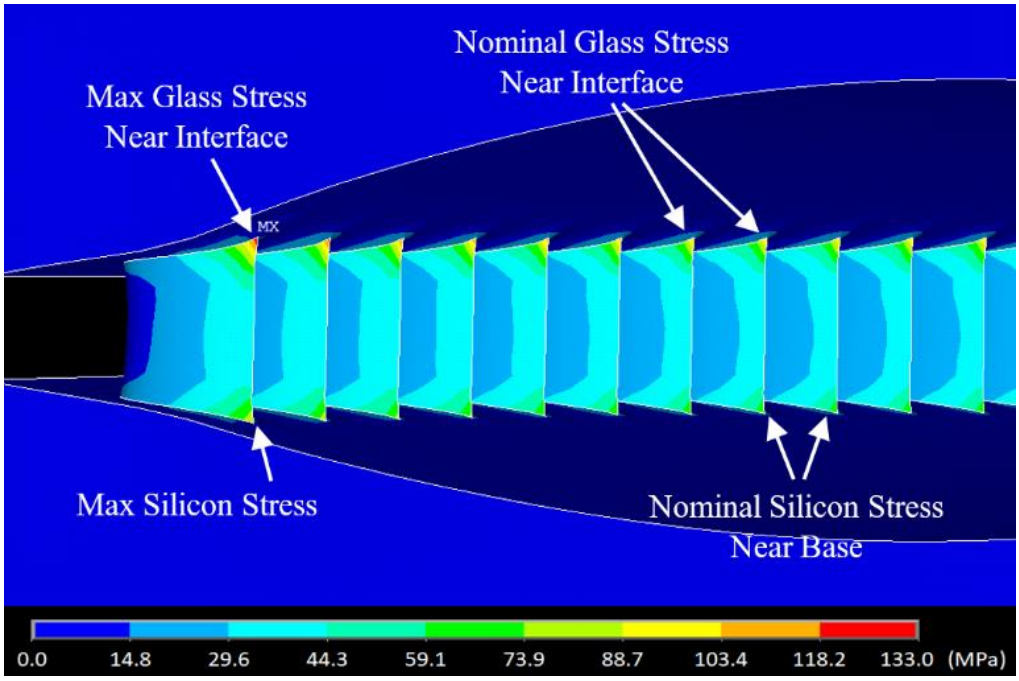

Figure 7.8 – Key principal stresses of interest for hydrofoil pin fins (Case A)

With this parametric model, three important studies are chosen to be pursued. The first study is an exploration of the effect of reducing the separation distance between pin fins and the larger support structures. By reducing this spacing distance, it is expected that the stresses observed (and thus the resulting stress intensity factor) will drop. The second study investigates what effect changing the mesh size for the small pin fins have on the critical stresses observed. It is expected that the mesh will not converge for this sharp corner geometry, but the comparison of results for the same mesh size is still insightful. The third study of interest is for determining the degree to which the hydrofoil shape exacerbates the stresses relative to a standard cylindrical pin fin shape and also a hybrid truncated hydrofoil pin fin shape.

7.3 Model Results for Various Cases in Full Study

The first variation of the separation distance between large support and small hydrofoil pin fins focuses on the variation of principal stress for separation distances of 1,500 µm down to 250 µm. Using Figure 7.6, Figure 7.7, and Figure 7.8 as reference, the maximum stress at the interface of glass and silicon, as well as the maximum bulk stress for silicon are recorded and the results shown in Figure 7.9. Indeed, the maximum stresses drop as the separation distance decreases. Additionally, it is observed that the stress in the pin fins near the glass-silicon interface has the highest stress for all four cases.

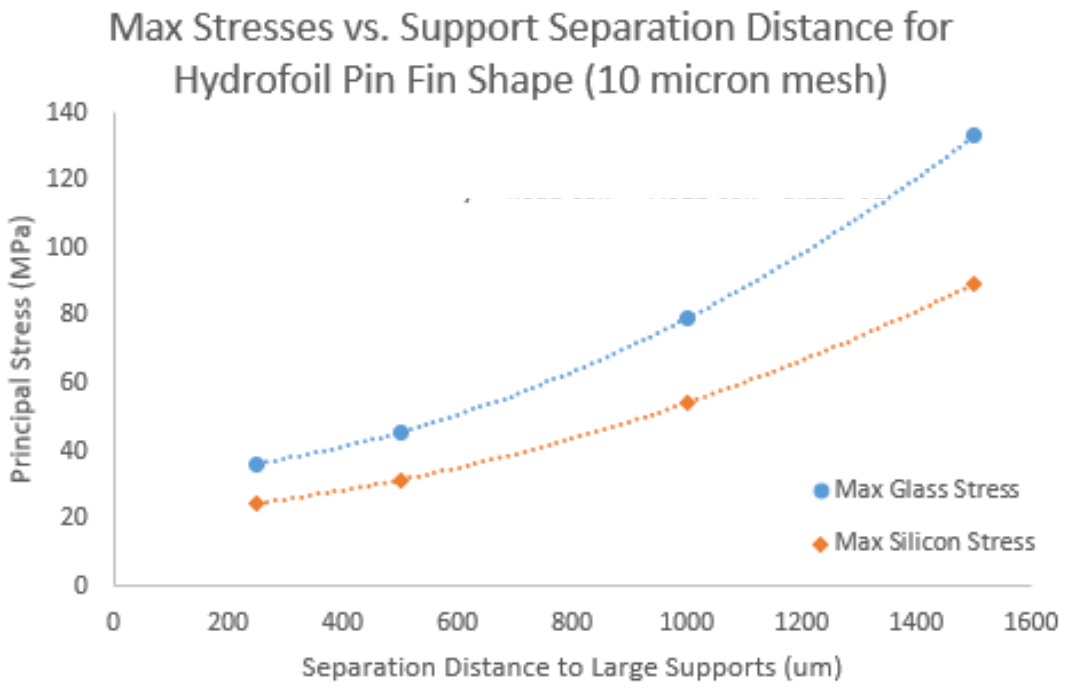

Figure 7.9 – Plot of maximum stress versus separation distance for 4 cases

Table 7.2 – Data for various cases modeled using the local pin fin model

Case	Shape	Mesh Size (μm)	Separation Distance (μm)	Max Stress Glass Side (MPa)	Max Stress Silicon Side (MPa)	Nominal Interfacial Stress (MPa)	Nominal Base Stress (MPa)
A	Hydrofoil	10	1500	133	89.4	103	73.5
B	Hydrofoil	10	1000	79.3	54.3	65.8	45.6
C	Hydrofoil	10	500	45.7	31.7	38.0	26.3
D	Hydrofoil	10	250	36.4	24.8	25.2	11.0
E	Hydrofoil	20	500	31.7	23.2	25.2	18.7
F	Hydrofoil	5	500	81.2	48.6	58.1	37.3
G	Hybrid	20	500	22.8	16.5	16.3	13.9
H	Hybrid	10	500	41.9	29.0	25.9	19.7
I	Hybrid	5	500	58.9	34.5	33.7	21.4
J	Circular	20	500	22.7	18.3	12.4	11.3
K	Circular	10	500	32.3	23.8	22.2	17.1
L	Circular	5	500	45.4	32.4	32.6	22.2

For cases two and three regarding mesh convergence and variation of pin fin cross-sectional shape, the studies are combined and completed for mesh size variations for all three shapes. The comparison for different shapes involves the profiles shown in Figure 7.10 with the hydrofoil, hybrid, and circular cross-sections. Across these three designs, the mesh size for the pin fins is varied for 20, 10, and 5 microns. In all of these cases the separation distance between small pin fins and the standard circular, large support pins is kept at 500 μm. Figure 7.11 shows the results of these mesh convergences for the three different shapes. Table 7.2 also includes a breakdown for all the results of this local model for the three different studies.

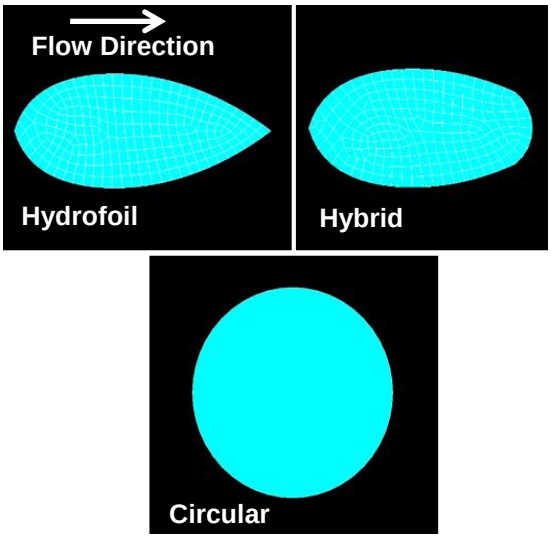

Figure 7.10 – Three pin fin cross-sections used in this local model: hydrofoil (top-left), cylindrical/circular (bottom-middle), and hybrid (top-right)

In terms of mesh convergence for any of the three shapes, it is not expected that this model will necessarily converge for the loading provide. The load likely causes the formation of a stress concentration at the sharpest corners as mesh size decreases. Though the stress concentration does not directly allow for a purely quantitative discussion, there is still valuable information from a qualitative perspective regarding shape effects. The maximum stresses observed in the hydrofoil shape case are approximately 50 percent higher than the circular shape. The truncated hybrid case only increases stress by approximately 20 percent relative to the circular case. The necessary pressures to cause failure would be reduced by a corresponding reciprocal amount assuming the linear elastic behavior of this brittle material set. A lower tolerable pressure threshold for the hydrofoil design is clearly undesirable but should be weighed against the improvement in thermal-fluid performance that may be obtained.

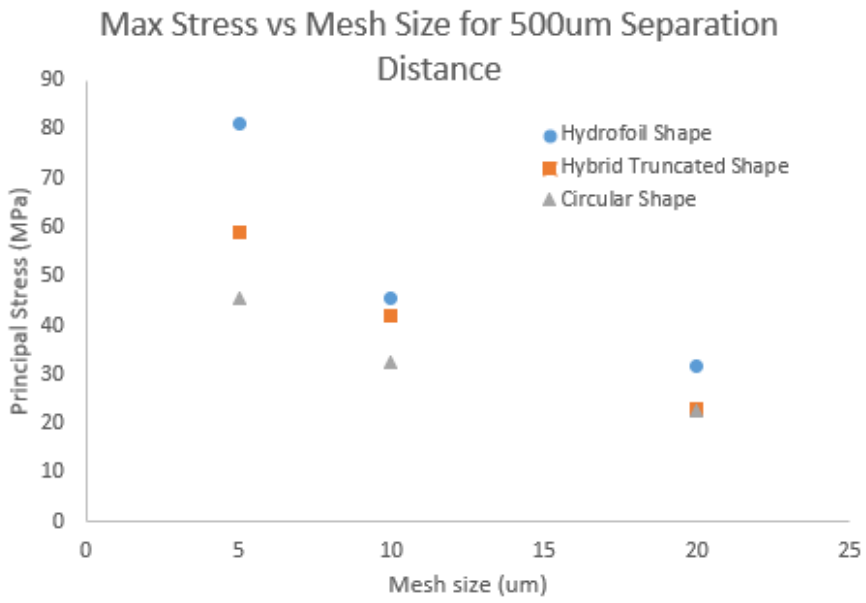

Figure 7.11 – Comparison of mesh and shape effects on maximum stress near the glass silicon interface

From a fracture mechanics perspective, this increase in stress from approximately 45 MPa to over 80 MPa greatly decreases the flaw size required for monotonic fracture. Since the fracture toughness of silicon is approximately 1 MPa$\sqrt{m}$, a corresponding crack size of approximately 10 to 100 µm would be required for crack propagation if this range holds for the 5 micron mesh size [31]. Still, the relative 78 percent increase in stress from 45 MPa to 80 MPa suggests the cylindrical pin fin design can handle approximately that same increase in pressure before reaching the same propensity for failure as the hydrofoil case.

In order to decrease the propensity for failure in future system designs, consideration should be given to the radius of curvature of the hydrofoil. Specifically, augmenting the radius of the hydrofoil tail may reduce the magnitude of the stress concentration that occurs at this location. The limits of fabrication resolution should also

be considered to ensure that the radius of sharp features is known. Another approach to mitigate failures would be to increase the number and density of the support structures. By reducing the separation distance between support and the hydrofoil pins, the magnitude of the stress concentration will be reduced. In this way the layout of the microchannel features directly impacts thermal, fluidic, and mechanical performance of the device.

CHAPTER 8. DEVELOPMENT OF EXPERIMENTAL TECHNIQUE FOR CHARACTERIZATION OF SILICON-GLASS INTERFACE

Characterization of the silicon-glass interface has been shown to be a critical need for development of further microelectronic packages that use anodic bonding. In the situation of microfluidic coolers such as the Thermal Background Cooler (Design B), failure of the silicon-glass material pair is a catastrophic failure for the design and a major issue to solve during design and implementation. Objective 4a for this work is to develop a novel fixtureless test technique for characterizing the silicon-glass brittle interface under working conditions similar to that of a high-pressure microfluidic cooler. It is a secondary goal for this innovative test to also be applicable for characterization of other bi-material pairs.

There are several key features that the new test technique must have to achieve the primary goal and objective of this work. These are listed below:

- Silicon and glass materials are included and bonded using anodic bonding
- The cracking failure mode of interest takes place at or near silicon-glass interface during testing
- An internal pressure is responsible for initiating cracking and is the primary load on the system (using a working fluid for microfluidic cooling)

An initial concept for a test device for the new test technique is depicted in Figure 8.1. In this design a silicon substrate is etched to form a cavity with "prime features" for concentrating stresses during pressurization. A glass cap is used to close off the cavity and bond to the top of the silicon and any chevron-shaped prime features. A port hole is included for access to the cavity and to allow for loading of the prime features through pressurization of a working fluid. It is considered that by placing several chevron-shaped prime features in sequential cavities, failures may be observed in succession for different features over time and at different loads. This "Chevron Pressure Cavity" test combines a chevron-shape for stress concentration with pressurization of a working fluid in a cavity formed by the bi-material system.

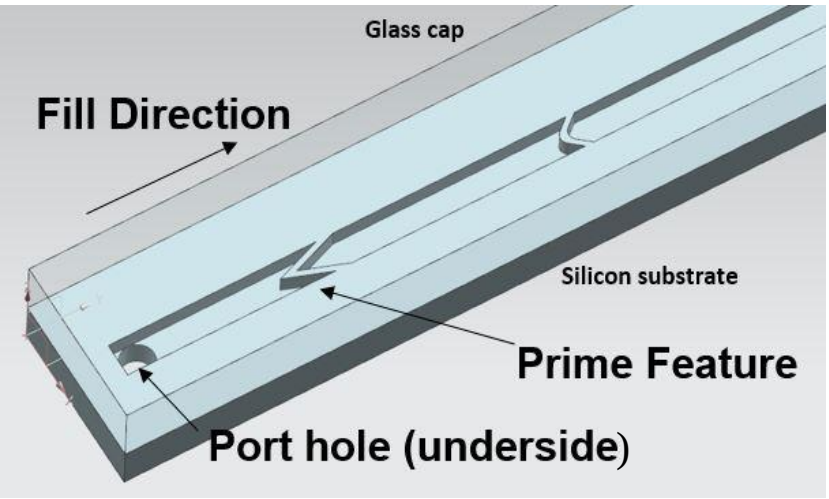

Figure 8.1 – Initial prototype for Chevron Pressure Cavity test

Through the use of a standard chevron test feature, the effect of radius of curvature, exposure angle, and feature thickness can be explored systematically through models and experiments. Figure 8.2 shows these parameters as defined for the chevron design test vehicles. This feature creates a known stress concentration that is the focus of experimental

and model failures, and by varying the geometry of the prime feature, it is possible the load for failure will be appropriately affected.

In fixture-based techniques like those previously mentioned [13-23], the loading conditions are usually displacement-controlled. Therefore, a drop in force load is an indication of crack propagation. Such fixture-based techniques are difficult to employ for the current silicon-glass interface due to the brittle nature of the material pairing. Thus the Chevron Pressure Cavity test attempts to utilize fluidic pressure drop as an indicator for the onset of failure rather than a force drop. The assembly consists of a silicon substrate and a glass capping layer bonded in the same way as the thermal test vehicle (Design B). As seen in Figure 8.1, fluid enters the port hole from the underside, the first critical chevron-shaped feature eventually fails due to pressurization of the internal fluid. The fluid then flows into the subsequent cavity allowing for visualization of failure through the glass top, and a change in pressure may be observed.

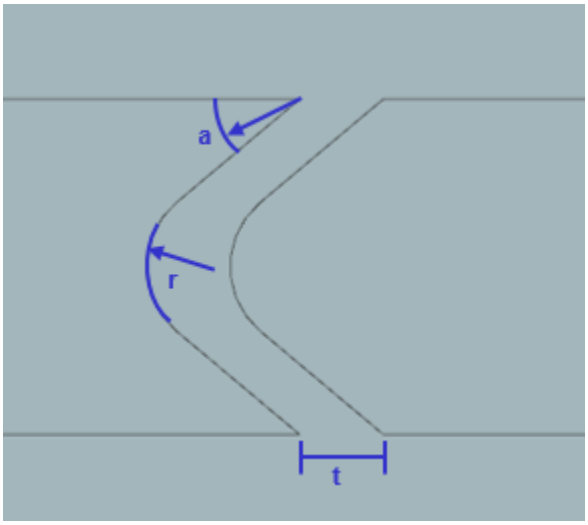

Figure 8.2 – Geometric parameters for chevron feature shape

8.1 Modeling for CPC Test Devices

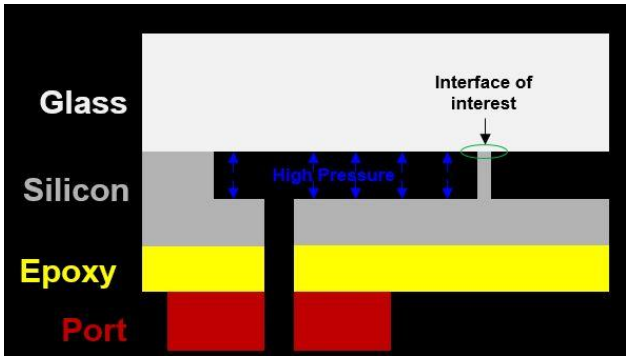

Figure 8.3 – Experimental sample build-up used in finite-element modeling

Prior to device fabrication, modeling of the system is completed to verify that the chevron tip receives the greatest stress concentration within the model. Shown in Figure 8.3, the material system is setup to best match the end setup for experimentation, including epoxy, silicon, glass, and constraints from the plastic port for fluid injection. The fluid itself was not modeled in the simulation. Instead, a static pressure was applied on appropriate internal faces resulting in high stress on the chevron feature, especially the sharp tip. In addition to this internal pressure condition, the system displacement was constrained at one corner to prevent rigid body motion due to the pressure loading.

Table 8.1 – Material properties for prototype modeling of CPC design

Material	Silicon	Glass	Epoxy
Material Model	Elastic, Anisotropic	Elastic	Elastic
Modulus, E (GPa)	140	70	12
Poisson's Ratio, v	0.28	0.16	0.25

For the selected stress results of Figure 8.4, the exposure angle, *a*, is 45^{o}, the radius of curvature, *r*, is "sharp" with an effective radius of 0, and is limited by the exposure angle and photolithography processes, and the thickness, *t*, is 50 μm. The resulting first principal stress in the silicon side of the device and near the interface for an assumed internal gauge pressure of 1100 kPag. The internal pressure causes the flat regions of the flow space to bend and bulge outward slightly creating stress zones. Tensile stresses arise at the walls of the microchannel and the tip of the chevron due to this bulging effect. Upon inspection, the maximum stress occurs at the tip of the chevron shape at the interface between the silicon substrate and the glass cap. For the load of 1100 kPag, the maximum first principal stress determined by the numerical simulation is 207 MPa at this tip concentration point. This number does agree with other estimates for stress at failure due of similar microchannel architectures, but will be expanded upon to better gauge stress intensity factor for this setup and across different mesh densities [33, 35].

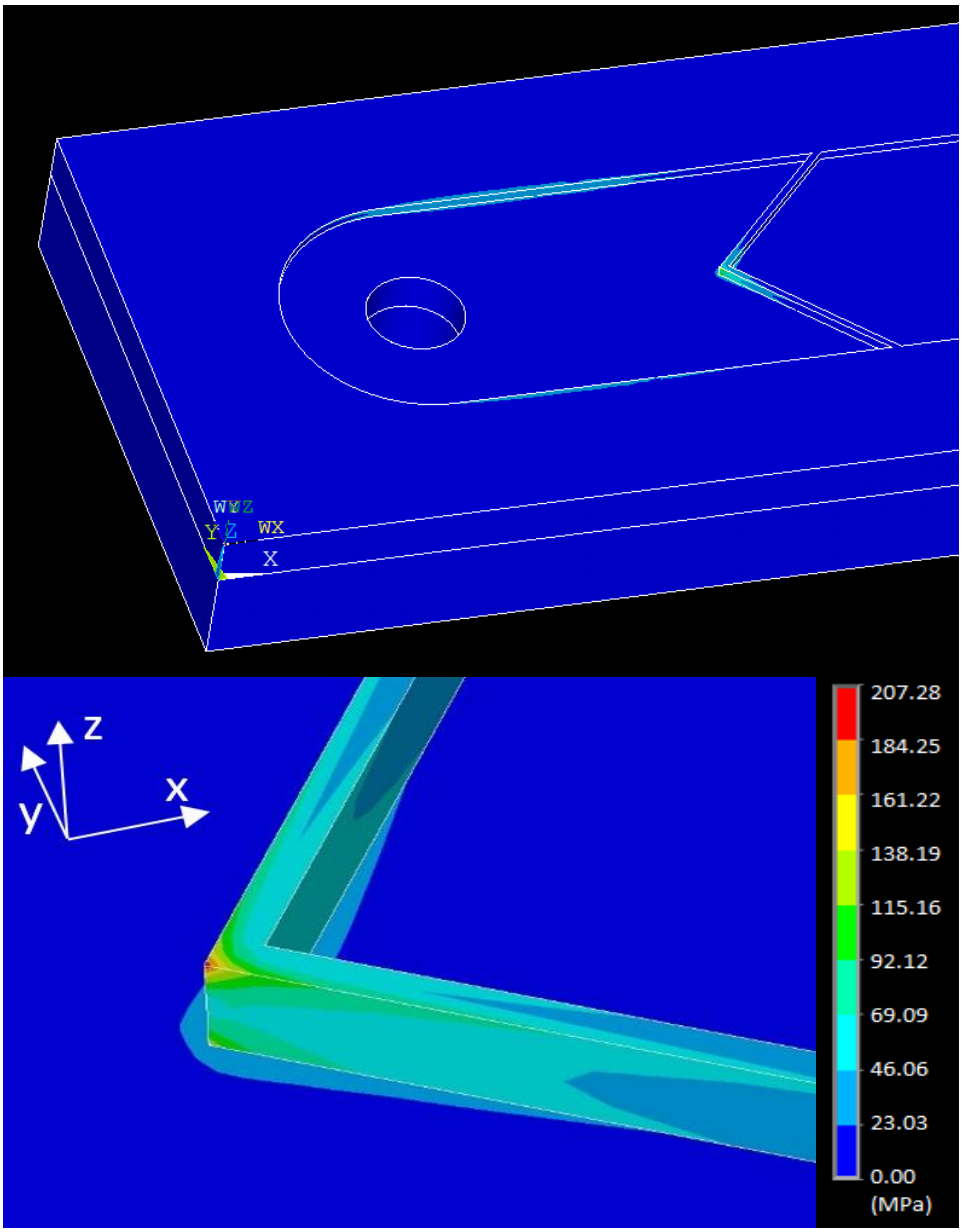

Figure 8.4 – View of model results for prototyping of CPC devices (first principal stress)

8.2 Serpentine Devices

In the initial test prototype, a long, serpentine microchannel is fabricated with intermediate blocking features in chevron and other shapes. In place of the initial concept of Figure 8.1, the serpentine design shown in Figure 8.5 and Figure 8.7 is developed and

fabricated to allow for visualization of the full device in a more localized area rather than a long channel. In other words, the long microchannel is compartmentalized into series of cavities with different areas and thus different volumes. When the fluid (water) is injected into the first cavity and as the pressure continuously increases, the first chevron feature fractures making the fluid rush into the next cavity. In this current setup, it is possible to visually detect when the first chevron shape fails due to the use of the glass capping layer. Though a pressure drop was not observed at the time of failure for most of the experimental results, this may be due to the relatively high viscosity of water (compared to air for instance), which slows the flow of fluid from the initial chamber to the subsequent chamber.

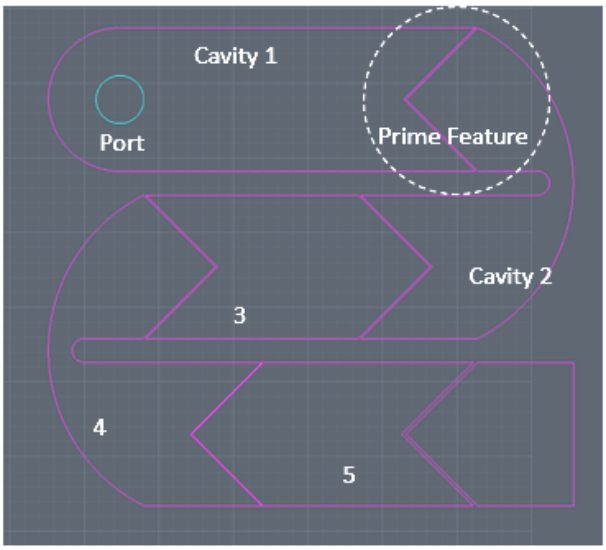

Figure 8.5 – Mask design for serpentine multi-chambered experimental devices

The experimental devices for testing are fabricated using a very similar process to the actual fluidic microchannel application devices. A 4-inch wafer of 500 µm thick silicon and a 4-inch substrate of 700 µm Pyrex glass are used as outlined in the processing steps

in Figure 8.6. In a class 100 cleanroom, the silicon substrate is etched during two separate etch processes to yield the port holes and the microchannel architectures. The glass is then bonded to the silicon substrate to cap the flow domain, resulting in the only available openings being the port holes, which have been etched all the way through.

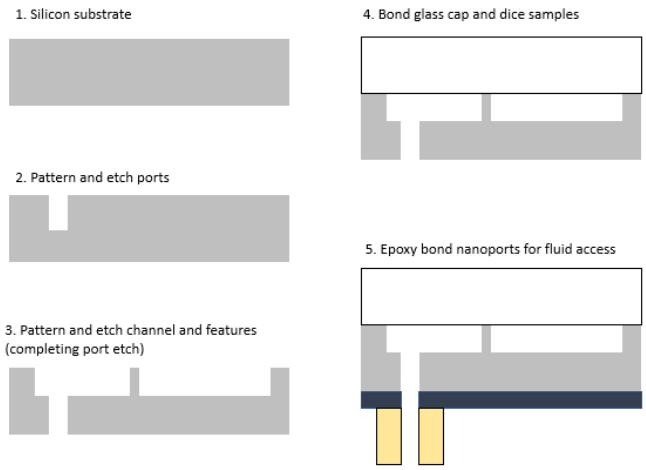

Figure 8.6 – Fabrication process for experimental test samples

Figure 8.7 – Actual devices after fabrication

8.3 Serpentine Device Testing

Experiments have been conducted for the given geometry in Figure 8.7. The fluid, in this case water, fills the cavity ahead of the prime feature as the fluid pressure is increased due to external compression. Pressure is precisely controlled via a syringe pump and feedback from a pressure transducer. As pressure increases, the fluid enters the first cavity and compresses residual air in the system. Eventually the first chevron structure catastrophically fails and fluid flows past the feature head into the next cavity, resulting in visual confirmation that the feature has failed via microscope observation. In this way the failure pressure can be determined for the given feature geometry and experimental setup parameters. Figure 8.8 illustrates the progression of the fluid front during an experimental failure of a 50 μm thick chevron feature. The fluid front first can be seen ahead of the chevron tip as it compresses the trapped air remaining in the first cavity. After failure, the fluid rapidly proceeds into the next flow region and begins compressing the air that was trapped in the second cavity at approximately atmospheric pressure. Successful experiments are completed using water with pressures ranging as high as 1600 kPag for the designed devices before failure.

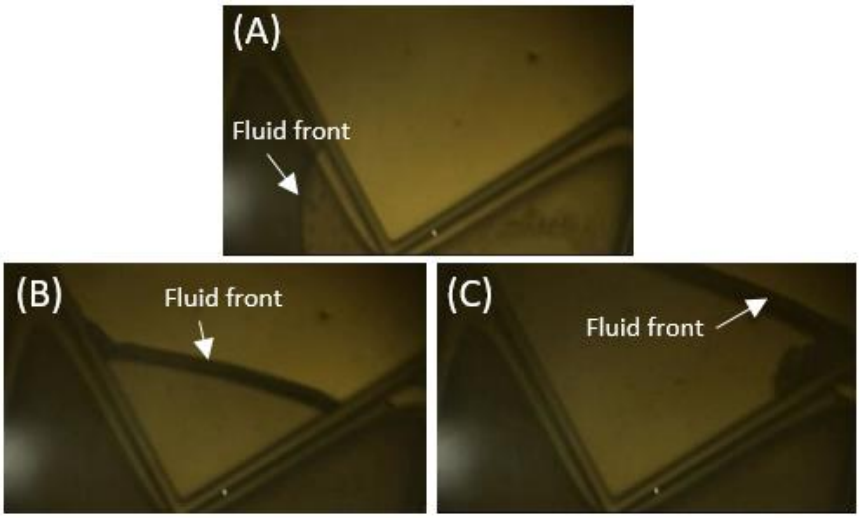

Figure 8.8 – Device imaging just before failure (A), during failure (B), and after complete failure (C)

The full failure process of a single feature spans less than one second, but no noticeable pressure drop was measured by the pressure transducer in most cases. Still the pressure versus time plots were useful for understanding the sequence of the experimental studies. Figures Figure 8.9Figure 8.10 show the gauge pressure versus time plots for two runs of sample failures with the instances of fracture highlighted. The failure instances in Figures Figure 8.9 and Figure 8.10 were determined through visual observation of fracture in the sample under fluid pressure, and not necessarily through sudden drop in pressure. It should be pointed out that the pressure drop approach is intentional, as this approach can be employed for silicon-silicon and other opaque brittle interfaces to be able to determine the onset of interfacial fracture by observing the pressure drop. For silicon-glass interface, it is possible to determine the onset of by visually monitoring the interface with the continued increase in fluid pressure.

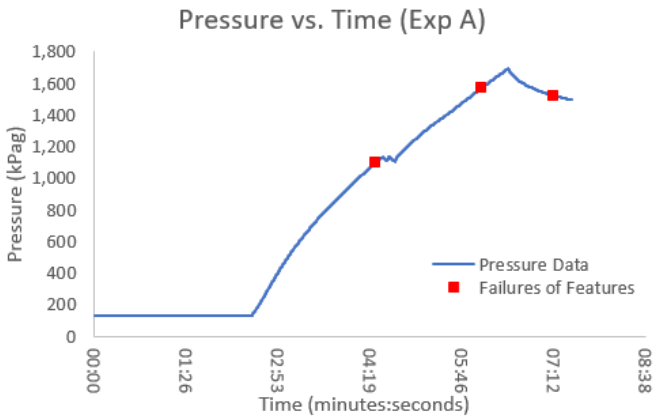

Figure 8.9 – Gauge pressure versus time for experimental run with multiple visualized failures (experiment A)

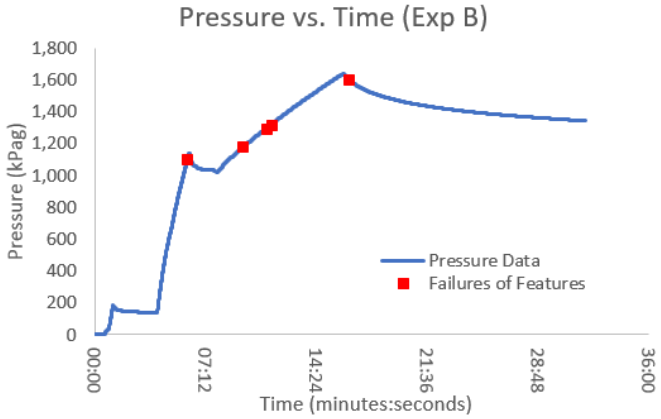

Figure 8.10 – Gauge pressure versus time for sample experimental run with five feature failures (experiment B)

The results of experimentation indicate relatively repeatable methods for the same sample geometry. For the experimental results, the pressure versus time plots indicate failures ranging from pressures of 1000 kPag up to 1600 kPag for the chevron feature thickness of 50 µm. Possible sources of variability arise from the pressure transducer measurement error and any discrepancy in pressure of the cavity and pressure upstream at the transducer. The pressure is assumed to immediately equalize between cavities at the point of failure. Fluid flow is observed to be relatively slow, which may negate the initial

assumption of the cavities' pressure equalization. Additionally, at the time of failure, an instantaneous pressure drop is rarely seen. Visual inspection of failures is still reliable for these experiments nonetheless. Generally, the repeated and consistent cracking occurring during experiments suggests the methodology can successfully generate useable fracture data, particularly for glass-silicon material systems.

Because a pressure drop reading is not noticeable at the same time as cracking and failure is observed visually, the sample devices are reengineered to increase the likelihood of measuring pressure drop. Samples are redesigned to have a single isolated instance of the chevron feature which allow for venting to ambient conditions immediately after failure in the zone past the chevron.

8.4 Redesign for Venting

The second design separates each chevron feature into its own sample with a vent to ambient conditions in the subsequent chamber. In this way, any compartmentalization (from the serpentine design), which may be limiting the drop in pressure at time of failure, is eliminated. Visualization is still one possible method for detecting failures, but is used in tandem with pressure drop. Figure 8.11 shows the full design of a CPC test sample with various dimensions. The inlet port etched into the silicon on the left side allows for fluid flow into the system as it is pressurized. An outlet vent hole is also etched into the silicon on the far side of the chevron feature to allow for a pressure release immediately after the chevron feature has cracked fully.

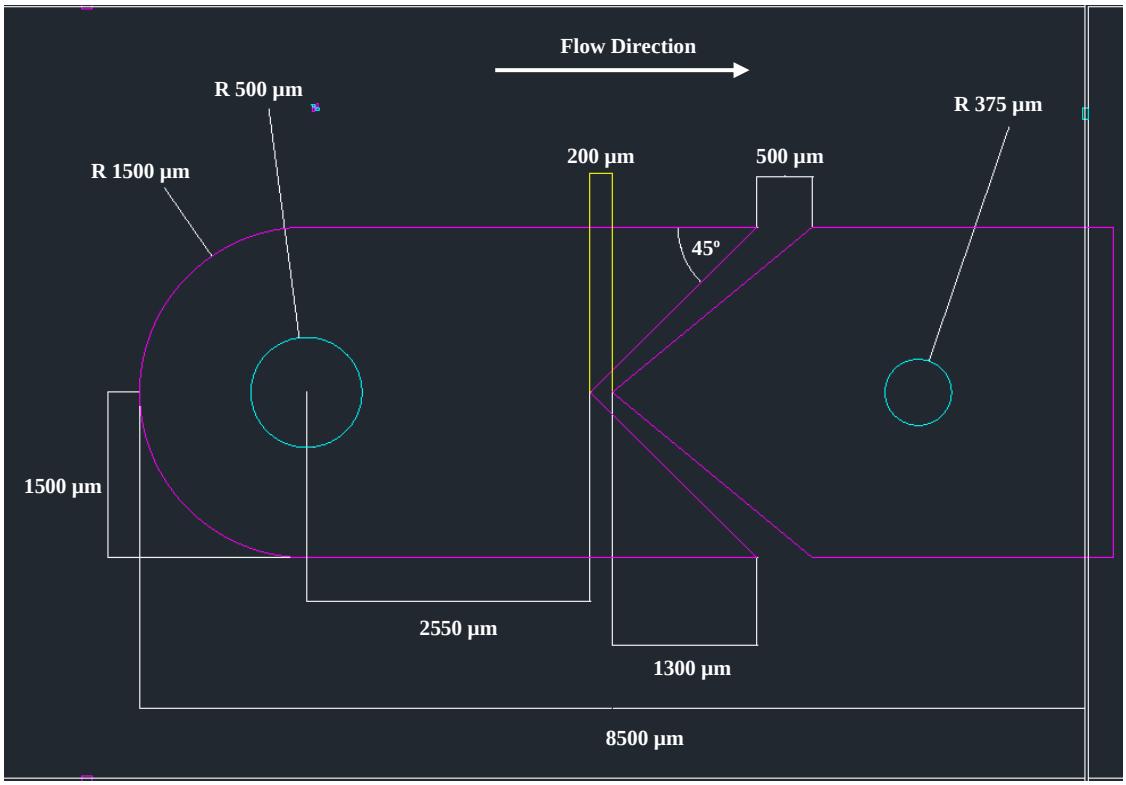

Figure 8.11 – Dimensioning for silicon etched geometry of CPC test samples

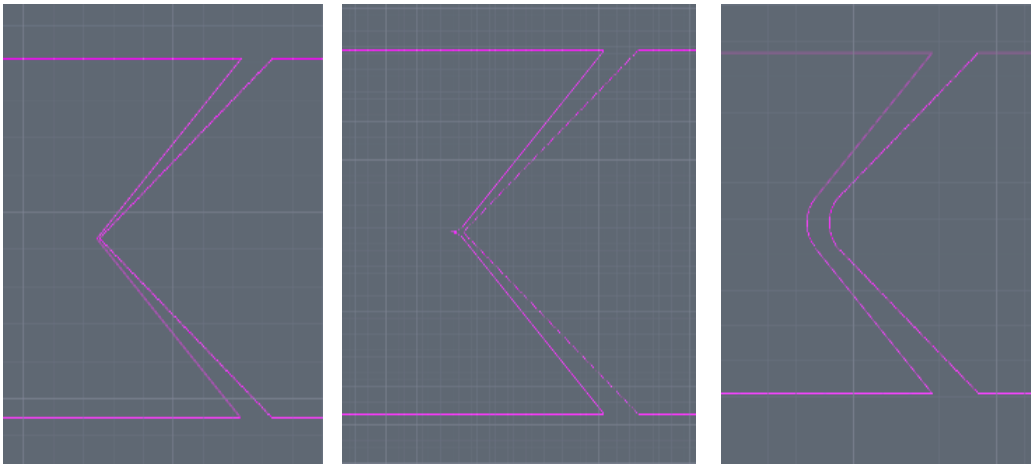

Figure 8.12 – Multiple designs for exploring the effects of changing chevron parameters and base geometry

Figure 8.12 includes various options for adjustments to the chevron shape that may produce different experimental results. Depending on the tip shape and thickness, there could be a lower or higher pressure required to initiate cracking and produce failure. There may also be geometries that arrest cracking better than others, i.e. a chevron which widens rapidly farther from the tip. With this design, initial 3-D modeling is also conducted. Figure 8.13 and Figure 8.14 illustrate the device prior to operation and a depiction of the course of fluid flow as the sample is pressurized with working fluid. In Figure 8.14, fluid first enters the port hole (top-left) and begins to compress any air that is trapped in the sample. Then (top-right), as pressure increases the fluid front moves forward into contact with the chevron tip and compresses air bubbles even further. Just after the point of cracking and fracture the fluid is observed to traverse beyond the chevron feature (bottom-left). Finally the pressure in the system begins to drop as the working fluid is allowed to vent rapidly to ambient conditions (bottom-right).

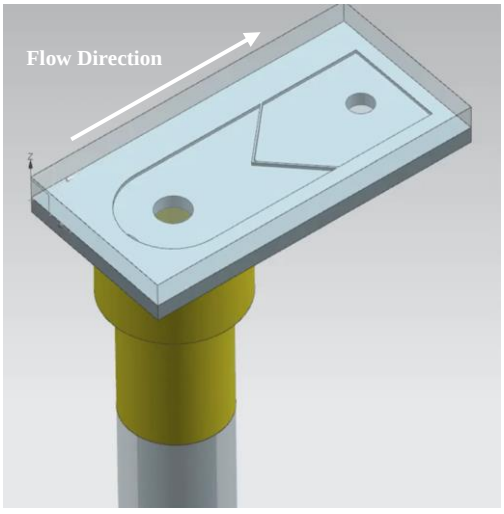

Figure 8.13 – Model of device setup during testing

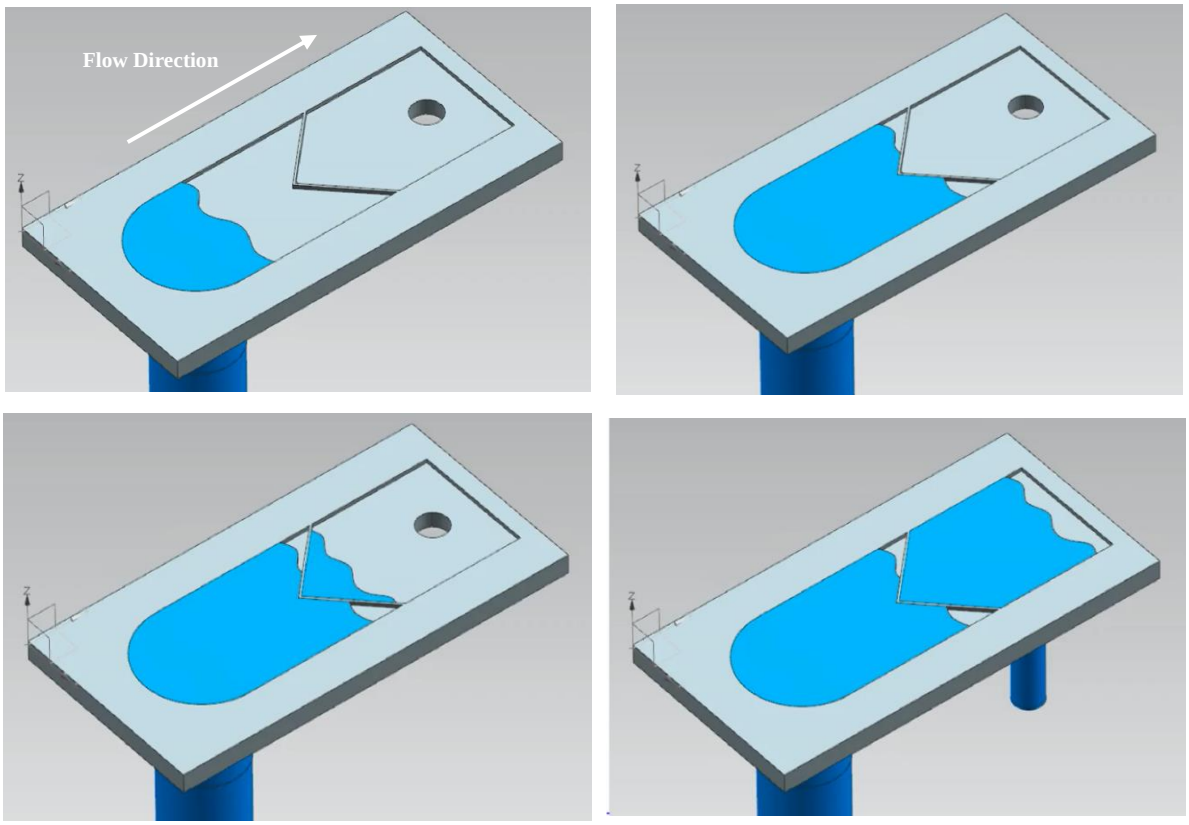

Figure 8.14 – Progression of fluid front from inlet (top-left), to chevron face (top-right), to beyond chevron after failure (bottom-left), and to vent (bottom-right)

CHAPTER 9. CHEVRON PRESSURE CAVITY TEST: EXPERIMENTAL TESTING AND MODELING TO DETERMINE CRITICAL MECHANICAL FAILURE CRITERION FOR SILICON-GLASS INTERFACE

The last objective (4b) of this work involves enhancing the innovative Chevron Pressure Cavity test setup, extracting experimental data for test samples, and correlating the data with models to determine a failure criterion for the silicon-glass interface. The successful demonstration of the proposed CPC test is illustrated through selected experimental data and modeling results in this chapter. The samples of interest are fabricated in the arrangement captured in Figure 9.1.

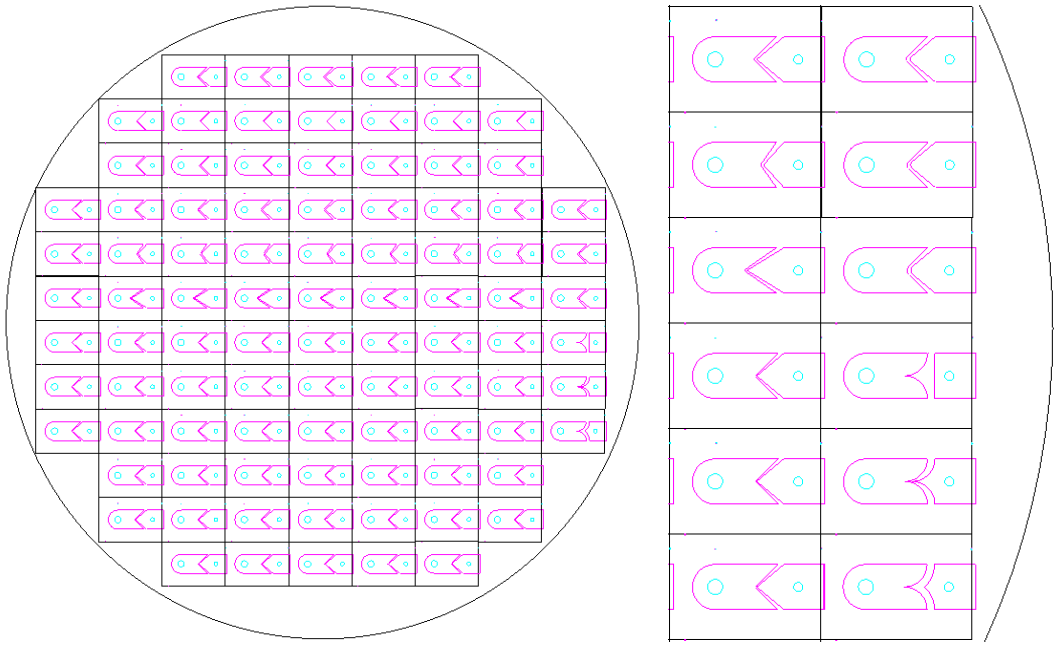

Figure 9.1 – Mask layout for Chevron Pressure Cavity test design (left) and enlarged section (right)

With the CPC test samples fabricated, the remainder of the test apparatus is setup. The full system involves a syringe and a pump for pressurizing the closed system. PEEK tubing is used with several valves, as shown in Figure 9.2, to connect the syringe with a pressure transducer and the sample device. As the system is slowly pressurized with the syringe pump, the pressure within the system can be carefully monitored via readout from the pressure transducer. Ideally a camera is setup to record the progress of the working fluid within the sample device (particularly for this case with a glass cap, since flow visualization is viable). Though expected failure pressures range from 1500 kPag to 4000 kPag, the flow loop is designed for higher pressures and is first tested with no sample attached to loop to ensure the system has no leaks up to 4000 kPag.

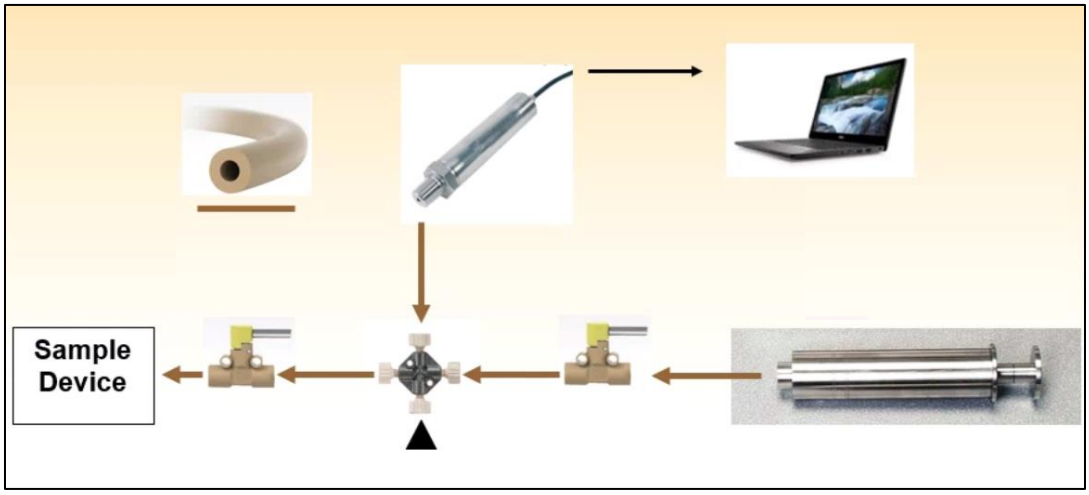

Figure 9.2 – Closed loop system for Chevron Pressure Cavity test

9.1 Chevron Pressure Cavity Test Experiments and Results

After completing the experimental flow loop setup, the system can be filled with working fluid (water as is the case for the following experiments). The sample can then be

attached to the system prior to pressurization and adjoined to the remainder of the closed loop via a valve.

The first sample, Sample 1, provides an illustrative example of the Chevron Pressure Cavity test. Figure 9.3 contains a series of images from a video recording of the sample during the CPC test. The actual pressure data is shown in Figure 9.4 for the test also. Through camera recording and logging of real-time pressure data, the silicon-glass sample can provide visual and pressure feedback simultaneously, which can later be compared side-by-side. In Figure 9.4, the pressure is slowly ramped up as the fluid in the system is gradually compressed from ambient conditions to approximately 2750 kPag pressure (A to B). During this ramp time, the fluid enters the first chamber and begins to compress the trapped air as seen in images 1-7 of Figure 9.3. At this pressure, cracking occurs and propagates through the chevron feature to the second cavity. This occurs at B in Figure 9.4 and image 8 of Figure 9.3. After this, the pressure begins to drop on the readout from the pressure transducer and the fluid is directly observed to progress toward the vent hole past the chevron feature. Since the maximum pressure obtained is 2750 kPag, this is considered the loading condition for which cracking occurs within this chevron feature. The drop in pressure is also simultaneously corroborated by the visual evidence through the glass capping layer. This maximum pressure is used in the model to determine the critical energy release rate.

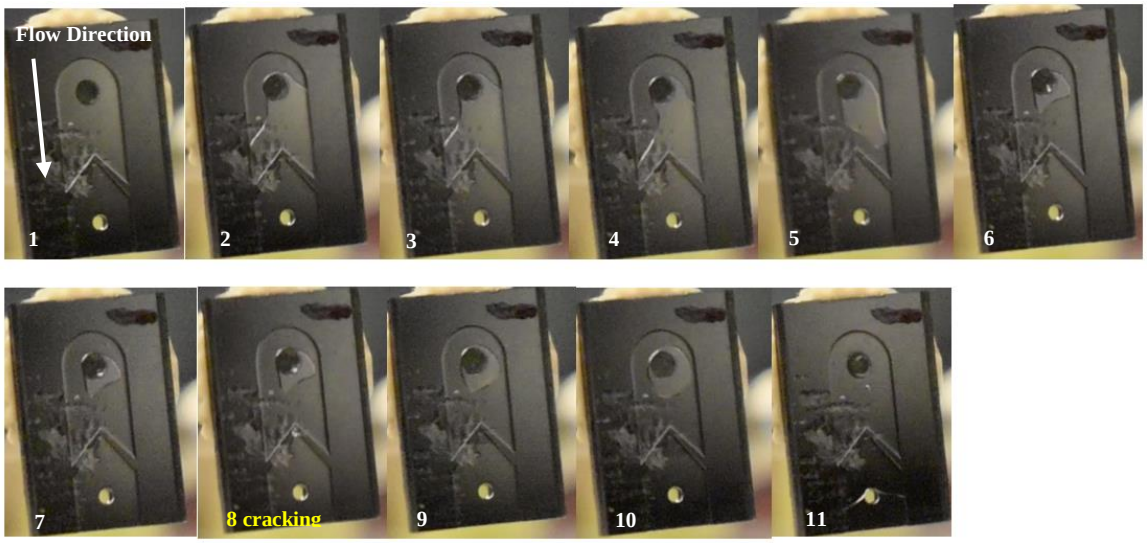

Figure 9.3 – Imaging series for CPC test of Sample 1

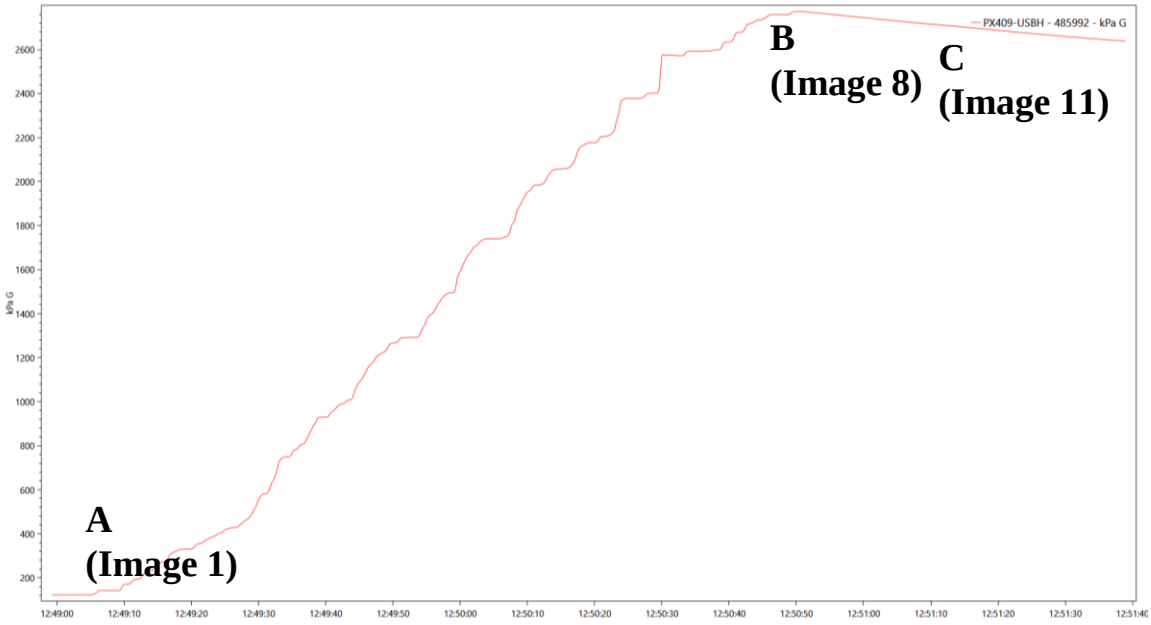

Figure 9.4 – Pressure vs. time for Sample 1 CPC test with slow venting

Additional failure pressure data are measured for different variations of chevron geometry, some of which are presented including Samples 2, 3, 4, and 5. Sample 2 provides other strong data for use in characterizing the silicon-glass interface, and the test clearly confirms that both visualization and pressure drop are viable methods for

confirming point of failure during the test. For this sample, a series of camera images are included in Figure 9.5. The pressure data versus time for Sample 2 is provided in Figure 9.6. Similar to Sample 1, the pressure is ramped up from A to B in Figure 9.6 which corresponds to images 1-3 in Figure 9.5. At this maximum pressure of around 2350 kPag, the measured pressure value begins to decrease as cracking occurs, and fluid is penetrates the chevron and passes into the next cavity. From B to C, water and air vent to ambient conditions and the pressure drops quickly compared to Sample 1. The onset of pressure drop lines up with the visual observation of fluid flow for this test as well.

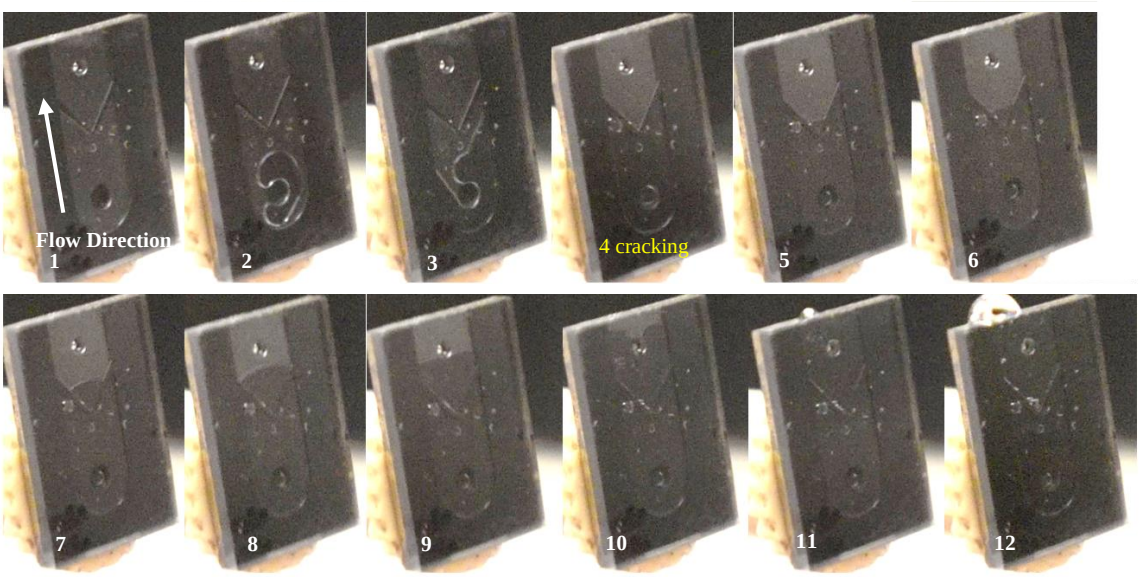

Figure 9.5 – Imaging series for CPC test of Sample 2

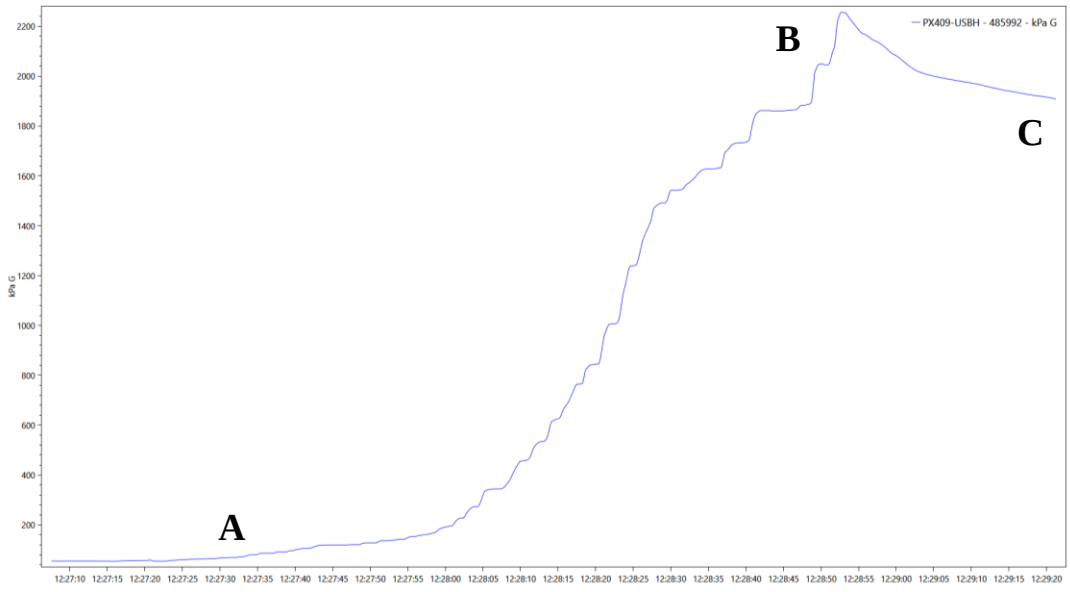

Figure 9.6 – Pressure vs. time for Sample 2 CPC test with slow venting

Samples 3 and 4 also yielded viable results for the Chevron Pressure Cavity test. The resulting plots of pressure versus time for Sample 3 and Sample 4 are shown in Figure 9.7 and Figure 9.8 respectively. The failure pressures for these samples are in excess of 3000 kPag.

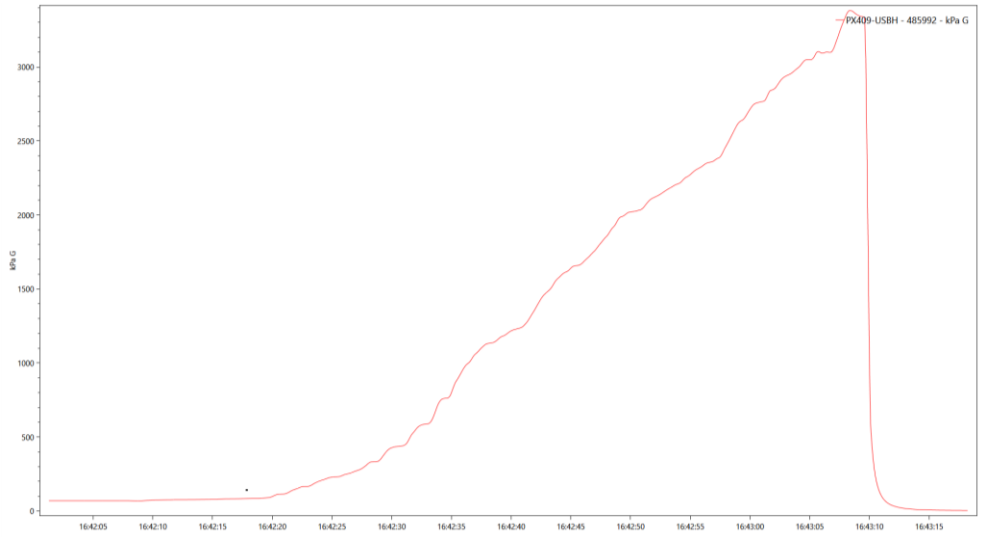

Figure 9.7 – Pressure vs. time for Sample 3 CPC test with rapid venting

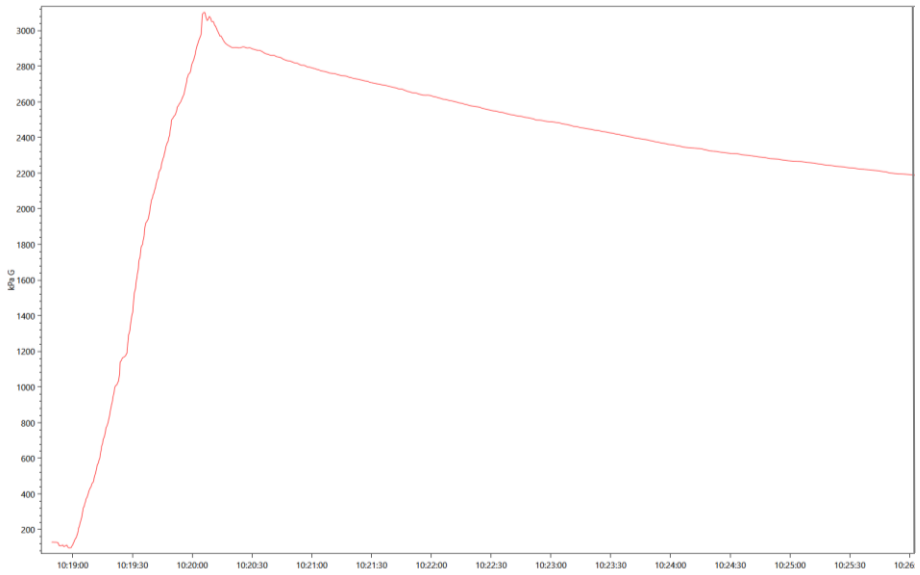

Figure 9.8 – Pressure vs. time for Sample 4 CPC test with slow venting

Sample 5 is a useful example test to examine a sudden catastrophic failure of the glass cap. The imaging and pressure measurement results for Sample 5 are shown in Figure 9.9 and Figure 9.10 respectively. For this sample the water front compresses the trapped air in images 1-4 of Figure 9.9 and A to B in Figure 9.10. Cracking occurs on a slower time scale for this sample and occurs at the chevron tip and then cracks upward into the glass cap. After the crack front reaches the glass cap, water temporarily leaks directly through the crack for a short time. The pressure is not alleviated quickly enough through this small crack compared to the increase in crack size, which increases stress intensity factor. After a short time of leaking as visible in image 8 of Figure 9.9, catastrophic failure occurs and a section of the glass cap cracks off and the pressure immediately drops to ambient conditions rapidly. Although the outcome for this test is slightly different, this test underscores the importance of considering the possibility that interfacial cracks can, in some cases, propagate into the glass and cause catastrophic failure as has been seen for other designs (generational devices of Design B).

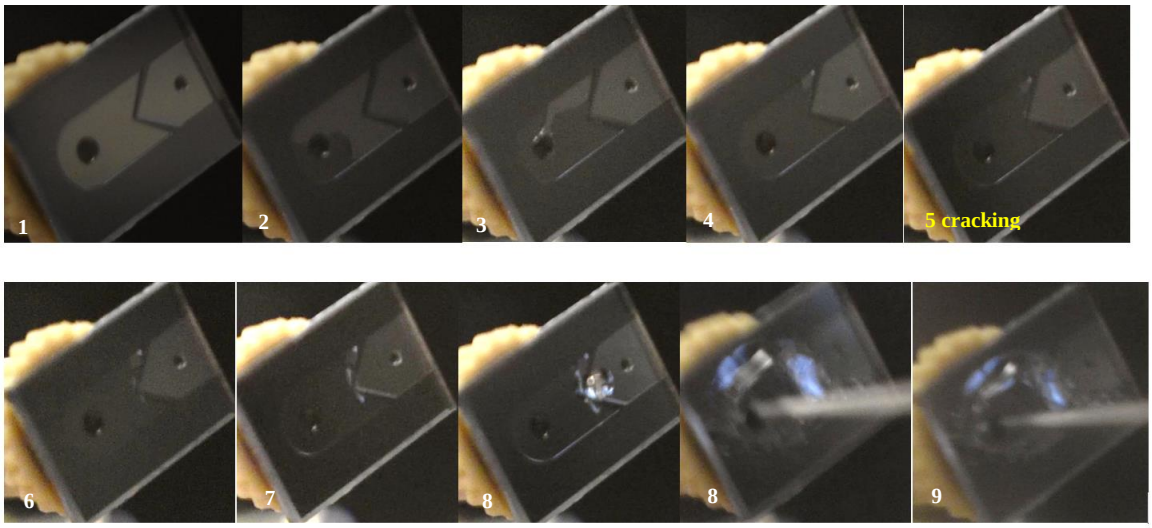

Figure 9.9 – Imaging series for CPC test of Sample 5 catastrophic failure of glass

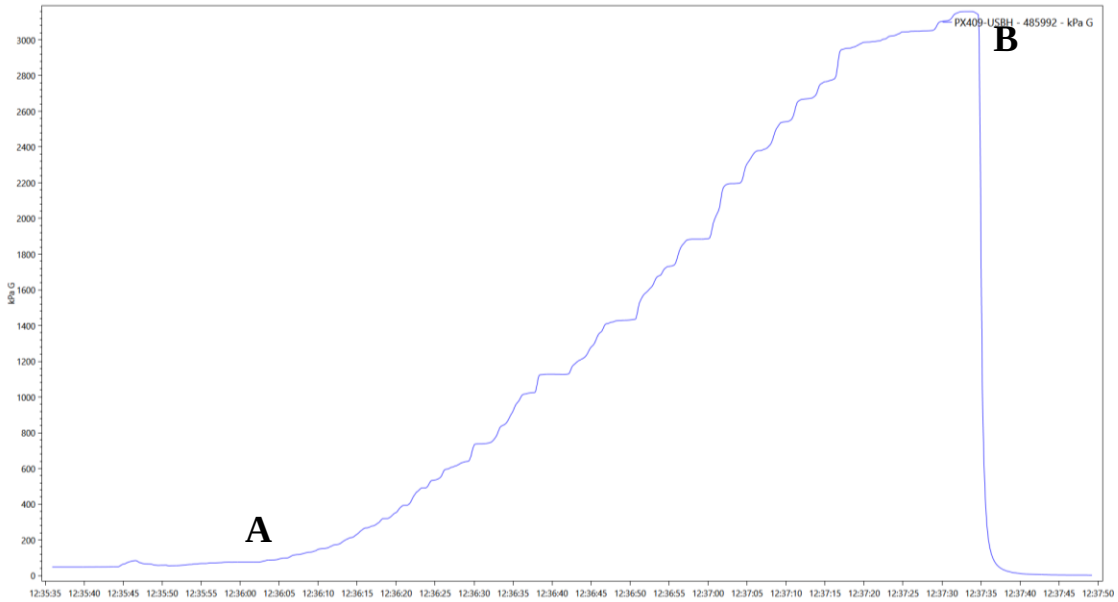

Figure 9.10 – Pressure vs. time for Sample 5 CPC test with catastrophic failure

9.2 Modeling and Analysis of CPC Test Results

From experimental results, the known failure pressures for the various cases can be used with finite element modeling to analytically explore the behavior of the devices under such loading conditions. Figure 9.11 is an isometric view of the model used to determine critical energy release rate for the experimentally observed failure condition.

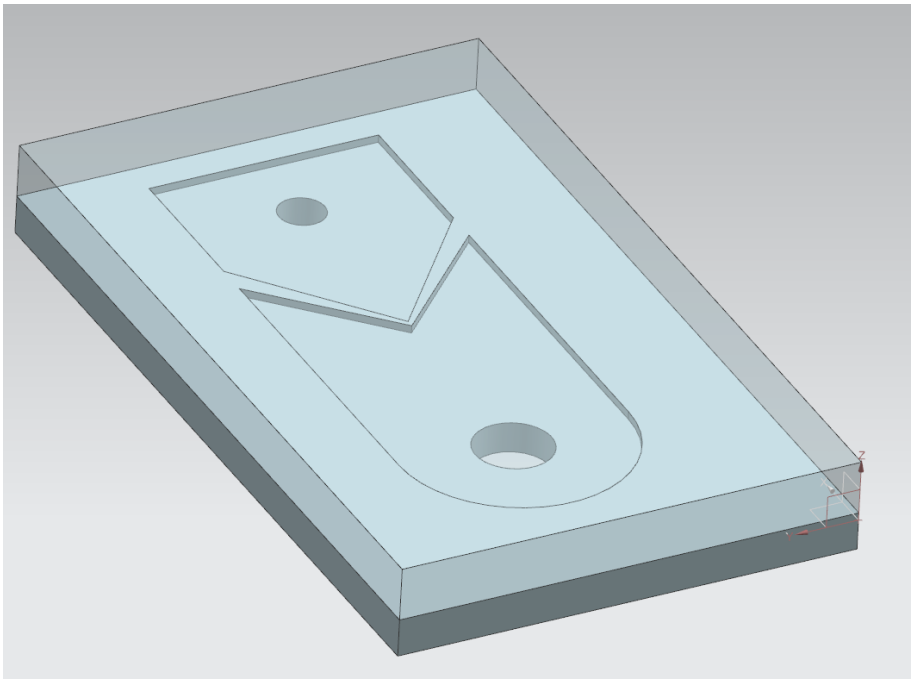

Figure 9.11 – Isometric view of full 3-D model

This sequential crack extension method requires solving a model for various cases having different crack lengths and recording resulting values for calculating strain energy and work energy done by the load on the system. In this way for various crack extension lengths, the theoretical energy released by extension of the crack can be calculated and related to the critical energy release rate, G_c. The procedure for combining experimental

pressure results with finite element modeling for sequential crack extension proceeds according to the following steps:

1. Obtain experimental failure pressure value for known sample geometry
2. Build finite-element model to mimic the known sample geometry, utilizing symmetry if possible
3. Assume elements at the silicon and glass interface to be perfectly bonded initially
4. Ensure that the finite-element mesh captures corners in geometry and appropriately constrained to prevent rigid body motion with known material properties assigned for silicon and glass
5. Apply the experimentally measured failure pressure value as a pressure load to the internal faces of the first cavity to mimic loading just prior to any cracking
6. Solve the model to obtain the displacement values (used to calculate volume change and then work done by the load) and total strain energy values of the system
7. Modify the geometry and boundary conditions to include a "cracked area" of a known crack length between glass and silicon of a specified geometry (triangular in this analysis)
8. Solve the model again and record the results for the new crack length; perform addition crack extension iterations up to the full crack length possible though the thickness of the chevron feature

To reduce calculation time the model is divided in half for symmetry down the midline as seen in Figure 9.12. The first cavity is loaded with an internal pressure equivalent to the CPC test pressure for a sample with this geometry. The exaggerated

displacement results (factor of 200) of Figure 9.13 indicate the first cavity bulges as expected.

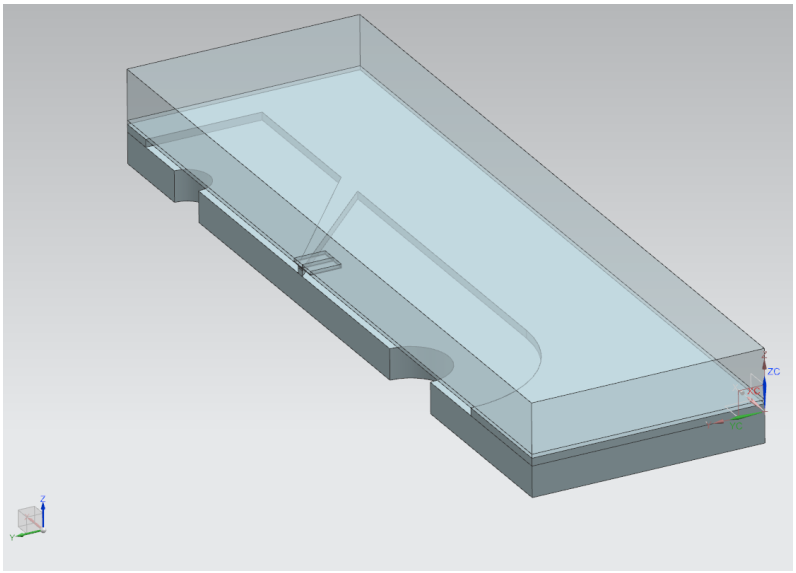

Figure 9.12 – Isometric view of half symmetry model

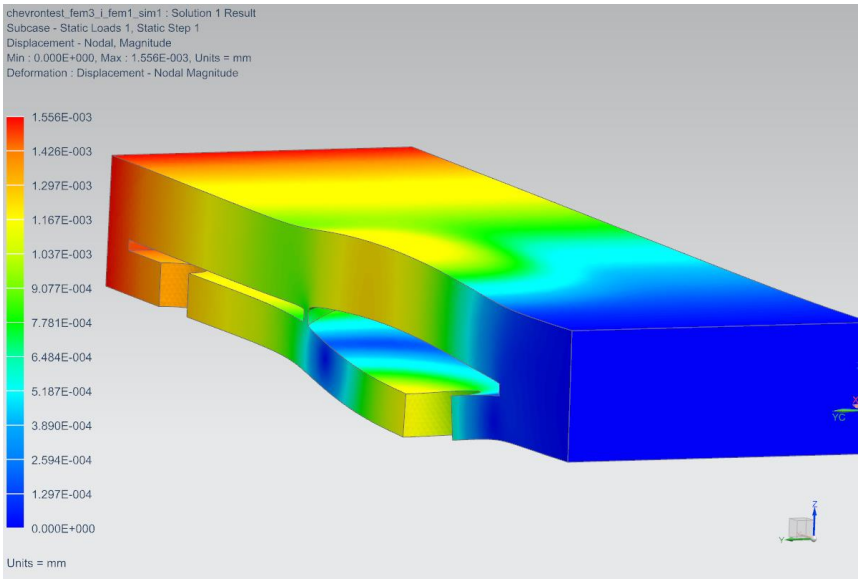

Figure 9.13 – Displacement (mm) results for half symmetry model

At the tip of the chevron, the first solution solve step assumes there is no crack whatsoever between silicon chevron and glass cap. The crack is iteratively extended further into the silicon glass interface, and a new solution is obtained. This cracking of the silicon-glass interface follows the diagram in Figure 9.14. Initially no crack is assumed, and the total strain energy of the system is obtained. In addition, the approximate internal volume of the first cavity is also recorded as the cavity expands due to pressure loading. This allows for calculation of the total external work done on the system.

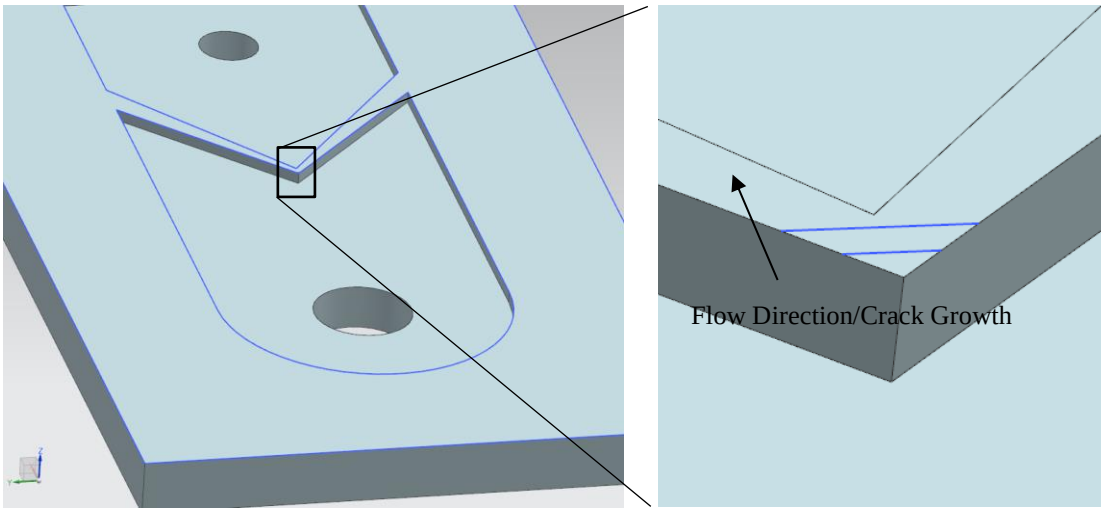

Figure 9.14 – Illustration of crack direction and crack iterations for sequential crack extension

According to Equation (9.1) for an incremental change in crack length or area, the incremental external work done on the system, dW_e, is equal to the sum of the incremental energy released from cracking, dW_s, and the incremental change in total strain energy, dU. Because there is no plasticity in this system of brittle materials, only the total elastic energy of the system must be obtained. For each iteration of crack length (0 µm, 40 µm, 80 µm), the requisite values are recorded for comparative calculation.

$$dW_s + dU = dW_e \tag{9.1}$$

$$dW_e = pdV \tag{9.2}$$

For this scenario, the pressure loading condition is kept constant during crack propagation and thus the incremental external work follows from Equation (9.2) based on pressure, p, and incremental volume expansion of the cavity, dV. With all this information, critical energy release rate, Gc, for this microfluidic loading scenario can be determined for the silicon-glass pairing. Table 9.1 and Table 9.2 include all the tabulated information from modeling and the subsequent calculated values associated with Sample 1.

Table 9.1 – Energy values for each crack length examined in model for Sample 1 (failure pressure 2750 kPag)

Case	Crack Length (µm)	Total Cracked Area (µm^2) 1/2 Model	Total Work Done by Pressure, "W_e" (J) 1/2 Model	Total Strain Energy, "U" (J) 1/2 Model
A	0	0	9.2955E-06	5.7968E-06
B	40	800	9.3072E-06	5.8017E-06
C	80	3200	9.3460E-06	5.8303E-06

Table 9.2 – Energy value and calculations for critical energy release rate for Sample 1 (failure pressure 2750 kPag)

Case	ΔArea (μm^2)	ΔU_e (J)	ΔW_e (J)	ΔW_s (J/m^2)	G_c (J/m^2)
A to B	800	4.9370E-09	1.1692E-08	6.7546E-09	8.4
B to C	2400	2.8533E-08	3.8785E-08	1.0252E-08	4.3

Based on this information, the approximate Gc value for Sample 1 is in the range of 4 to 9 J/m2. These values can be compared to the results for Sample 2 which are shown in Tables 9.3 and 9.4.

Table 9.3 – Energy values for each crack length examined in model for Sample 2 (failure pressure 2350 kPag)

Case	Crack Length (μm)	Total Cracked Area (μm^2) 1/2 Model	Total Work Done by Pressure, "W_e" (J) 1/2 Model	Total Strain Energy, "U" (J) 1/2 Model
A	0	0	6.3661E-06	3.9646E-06
B	40	800	6.3777E-06	3.9706E-06
C	80	3200	6.4043E-06	3.9901E-06

Table 9.4 – Energy value and calculations for critical energy release rate for Sample 2 (failure pressure 2350 kPag)

Case	ΔArea (μm^2)	ΔU_e (J)	ΔW_e (J)	ΔW_s (J/m^2)	G_c (J/m^2)
A to B	800	5.9831E-09	1.1603E-08	5.6197E-09	7.0
B to C	2400	1.9526E-08	2.6583E-08	7.0567E-09	2.9

The resulting critical energy release rate values for Sample 2 vary from approximately 3 to 7 J/m^2 versus the 4 to 9 J/m^2 of Sample 1. The value also varies depending upon the section of the sequential crack. There is expected to be some variation due to variance in defects and bonding effectiveness at the surface. Particularly at the edge when the crack initiates, this zone may not be as well bonded as the interior although the results suggest it has a higher critical energy release rate. This work does acknowledge the possibility that the assumed experimental failure pressure utilized throughout the modeling may not hold for initial, small cracks; i.e., initial cracking could occur for lower pressures which would lower the resulting G_c value for small crack lengths. Thus, the G_c values will be calculated using a starter crack length and propagate thereafter. Then, as the crack propagates towards the second cavity and the working fluid vents, the calculated G_c value may become more accurate for crack propagation. In addition to these calculated values for Sample 1 and Sample 2, the resulting values for Sample 3 are also presented in Table 9.5 and Table 9.6 for longer crack lengths.

Table 9.5 – Energy values for each crack length examined in model for Sample 3 (failure pressure 3480 kPag)

Case	Crack Length (μm)	Total Cracked Area (μm^2) 1/2 Model	Total Work Done by Pressure, "W_e" (J) 1/2 Model	Total Strain Energy, "U" (J) 1/2 Model
A	0	0	1.3397E-05	8.2299E-06
B	40	800	1.3422E-05	8.2419E-06
C	80	3200	1.3483E-05	8.2761E-06
D	120	7200	1.3571E-05	8.3286E-06
E	160	12800	1.3676E-05	8.4006E-06

Table 9.6 – Energy value and calculations for critical energy release rate for Sample 3 (failure pressure 3480 kPag)

Case	ΔArea (μm^2)	ΔU_e (J)	ΔW_e (J)	ΔW_s (J/m^2)	G (J/m^2)
A to B	800	1.205E-08	2.515E-08	1.31026E-08	16.4
B to C	2400	3.411E-08	6.079E-08	2.66796E-08	11.1
C to D	4000	5.259E-08	8.794E-08	3.53552E-08	8.8
D to E	5600	7.196E-08	1.051E-07	3.31568E-08	5.9

Again, for calculation cases involving smaller crack lengths (A to B), the calculated critical energy release rate is higher than others. These cases are removed from consideration for all 3 sample data sets and then combined to form a distribution of values for G_c. The sequential extension cases are included for the three samples including the values of 4.3, 2.9, 11.1, 8.8, and 5.9 J/m^2. The distribution of the various values is shown in Figure 9.15 with a box and whisker distribution. The lower quartile value of 3.8 J/m^2 is assumed to be a conservative estimate of the critical energy release rate for use in additional modeling.

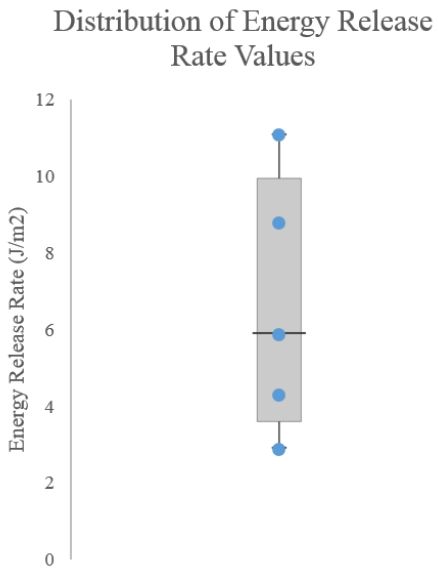

Figure 9.15 – Distribution, box and whisker plot for calculated critical energy release rate values

For future work, this modeling approach for critical energy release rate needs to be validated with additional samples and a secondary validation to evaluate the variance of G_c with crack length. Additionally, future work could shed light on any other sources of energy loss which could affect the final calculation for critical energy release rate. By designing the chevron feature with different apex angles and apex radii, it is possible to

manipulate the expected failure pressures for these devices and to influence direction of crack growth. In future work, the CPC test setup may also be used for several combinations of materials with no need for test fixtures. The greatest advantage of this setup may be that the loading conditions mimic the actual usage conditions of the device, which is critical for accurate understanding of the system performance in future designs.

9.3 Relating CPC Test to Co-Design Process

A co-design process for new microfluidic cooling designs should include characterizing prototype material set and determining if the prototype geometric design can sustain the target operating pressures. The Chevron Pressure Cavity experimental test and finite element modeling can be used to determine the failure criterion (critical energy release rate) of material pairs such as glass and silicon. The CPC test results indicate that the critical energy release rate is conservatively approximately 3.8 J/m^2 for silicon and glass anodic bond pairing. With this information, additional modeling can be conducted to evaluate whether the prototype geometry, which has pin fins and supports at a specific spacing, will be able to withstand the target pressures.

A simplified 2-D model is developed to solve for energy available for crack growth at the silicon and glass interface using a J-integral formulation. In this method a crack is assumed to exist at a known location with a known propagation direction. This model is used to verify the expected pressure limit for the generation 2 thermal test vehicle design

(observed failure pressure of 750 kPag and maximum support spacing of 5100 µm). The model is also used to determine the maximum support spacing allowed for a 3000 kPag pressure load, which is then compared against the results of the generation 3 design (failures did not occur for tests up to 2500 kPag with 1700 µm support spacing).

The geometric basis of this model is re-presented in Figure 9.16. This shows the case of an unconstrained simplified flow volume that experiences stress concentrations at the edges where the glass and silicon are bonded together.

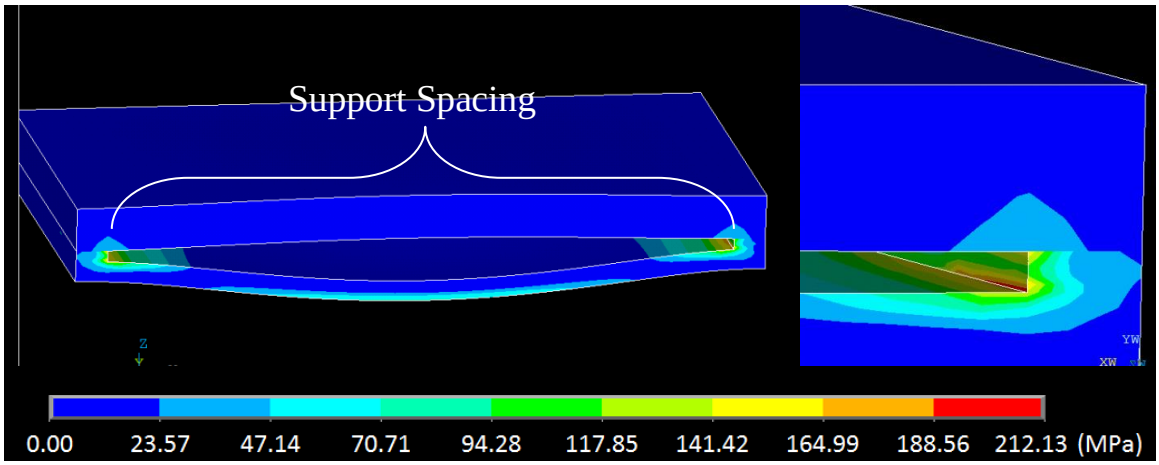

Figure 9.16 – 3-D simplified model for unrestricted pressurized microfluidic cavity

The model is setup with the expected loading conditions and separation distance to match the failures observed for the generation 2 design. A localized mesh of radial elements is also included as shown in Figure 9.17 for J-integral calculation. For a loading pressure of 750 kPag and support spacing of 5100 µm, the available energy release rate is 3.3 J/m^2 from this finite element model. When compared against the calculated limit of 3.8 J/m^2 from CPC testing and modeling, there is a good likelihood that the sample would fail at that pressure, and the experimental failure from the microcooler test samples validate

this prediction. By increasing the load pressure to match the target of 3000 kPag for the generation 2 test vehicle, the resulting calculated energy release rate is nearly a full order of magnitude higher at 31 J/m^2. This value indicates a significant likelihood for failure of this design for the high target pressure and would have been a major indicator suggesting redesign.

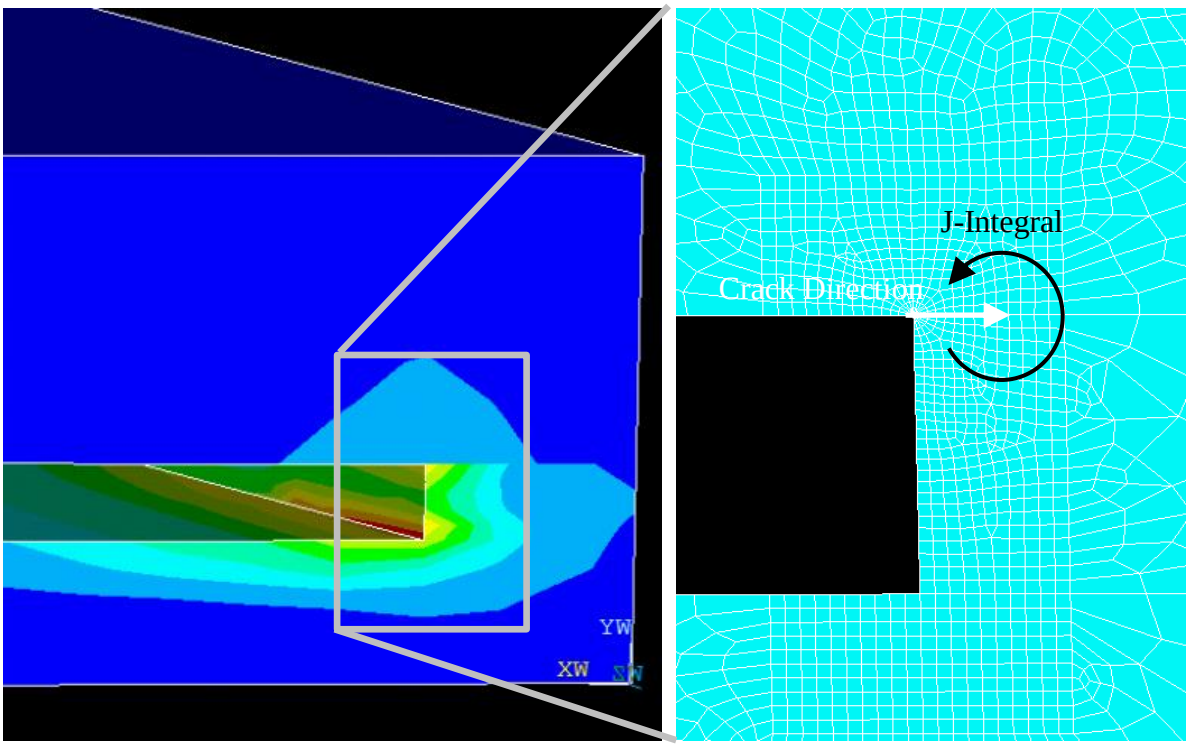

Figure 9.17 – Crack location and J-integral evaluation

Similarly, the success of the generation 3 design could have been predicted using the CPC test failure criterion result. When this J-intergral model is setup to match the generation 3 design setup for the target pressure (target pressure of 3000 kPag with 1700 µm support spacing), the resulting energy available for crack propagation is limited to 0.9 J/m^2. This would indicate that generation 3 test vehicles would be reliable up to the target pressure of 3000 kPag and possibly beyond.

Using experimentally-measured G_c from CPC testing in conjunction with predictive structural modeling for new prototypes, designs that will fail to meet the target pressures can be eliminated prior to any actual fabrication of prototypes or operating vehicles. Thus, successful test vehicles can be designed for reliable performance given the target high pressures for microfluidic cooler assemblies.

CHAPTER 10. CONCLUSION AND FUTURE WORK

4: SUMMARY OF THE THESIS AND PROPOSED CONTRIBUTIONS

This work identifies mechanical concerns in on-chip microfluidic coolers, provides a methodology for developing reliable high-pressure cooler designs, and presents a novel Chevron Pressure Cavity test technique for characterizing critical material interfaces in microfluidic architectures.

The first three main objectives for this work seek to provide insight into the mechanical behavior of novel microfluidic cooler designs from both modeling and experimental perspectives. This work developed 2-D and 3-D thermomechanical models of a theoretical design and provided insight into optimization studies for fabrication and geometric parameters of such a design. Also, the 3-D modeling and analysis for the second objective are part of a unique approach to iterative model and prototype for the thermal background test vehicle that can apply to future iterations of the hotspot cooler and FPGA liquid cooler. Objective three supports objective two and gives additional clarity to the tradeoffs associated with pin fins. Appropriate fin spacing is critical for mechanical performance along with thermal-fluidic enhancement.

The work of objective 4 (4a and 4b) concentrates on developing the novel Chevron Pressure Cavity test experiment and obtaining data for experimental failure pressures. The experimental results are utilized in finite-element models to evaluate critical energy release rate for the silicon-glass interface. This thesis makes the following intellectual contributions:

- This thesis is one of the first works to systematically study the mechanical integrity of multi-layer, pin-fin microfluidic architecture through various generations of design without compromising its thermal characteristics.
- This thesis has developed an innovative experimental technique for characterizing brittle interfaces as well as the associated data extraction techniques for developed test technique.
- The unique developed technique is fixtureless; utilizes pressure drop similar to force drop as in fixture-based techniques; can be adapted to several other interfaces beyond what was studied in this work.
- This thesis has developed guidelines for designing reliable microfluidic cooling architecture.
- This thesis has provided a test technique with experimental data and model results characterizing the interfacial strength of anodically bonded silicon-glass pair.

10.1 Future Work

In continuation of the work in this thesis, there is significant opportunity for expansion work related to the Chevron Pressure Cavity test. Other material systems can be tested such as silicon-silicon devices to verify pressure drop is a viable indicator of failure. This system can also be characterized using this test, if so. Other less brittle material pairs may also be tested.

Additional modeling of the CPC test and the results can be used to validate and enhance the calculations that are conducted. Potentially, new samples may be developed with more exotic chevron geometries to reduce variability in calculations of G_c.

Along with prior modeling of microfluidic test vehicles, there is reason to apply the same mechanical modeling approach to another microfluidic design to reduce prototyping time and iterations, particularly as it relates to pin-fin spacing and shaping. Further optimization of pin fins for balancing thermal-fluid and mechanical performance is also desirable. The Chevron Pressure Cavity test can be combined with structural modeling for co-design of next generation fluidically cooled microelectronic architectures to rapidly prototype novel and reliable high-performance devices.

APPENDIX A. SUPPLEMENTAL FIGURES

Figure A.1 illustrates the relative size of the CPC test devices having a length of 1 cm. This particular sample shows a case of the glass capping layer cracking and breaking off.

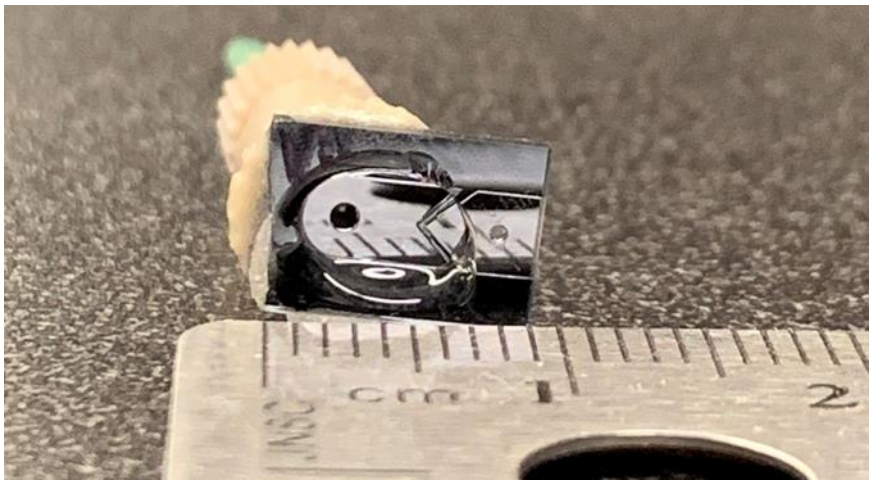

Figure A.1 – View of sample glass cap failure during CPC test

Figure A.2 and Figure A.3 illustrate the model setup for a correlated thermal model of the hotspot device design and also the results of this model. With heat generation and convection cooling conditions on the periphery of the device, the model yields a maximum temperature of 147 ^{o}C.

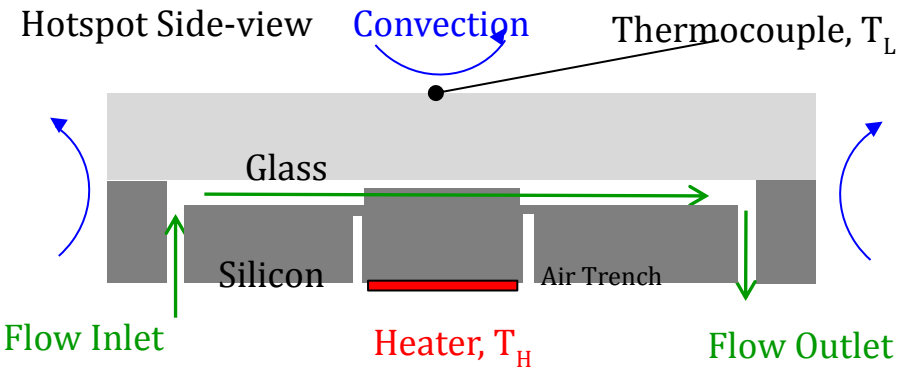

Figure A.2 – Mock thermal boundary conditions for Hotspot model

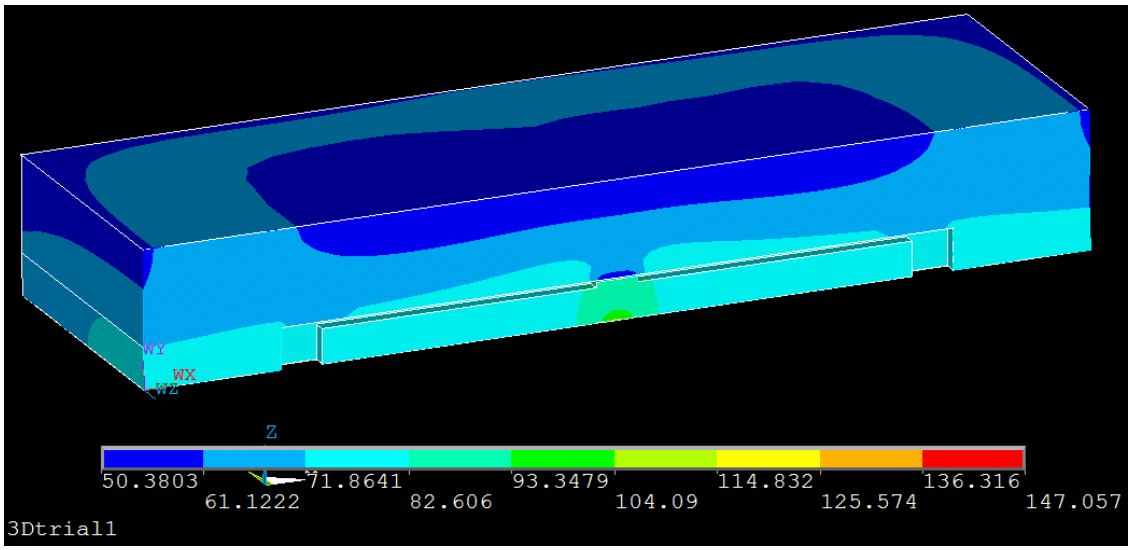

Figure A.3 – Mock thermal results for Hotspot model

Figure A.4 and Figure A.5 include stress results and displacements results for a one-quarter model of the FPGA liquid cooler device. This model is used for verification of experimentally measured warpage before and after the device has been etched.

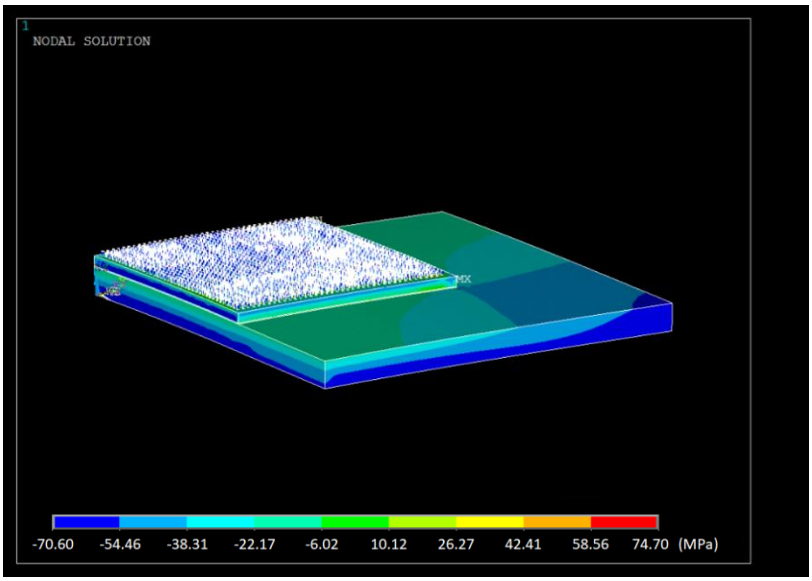

Figure A.4 – Stress results for FPGA warpage model

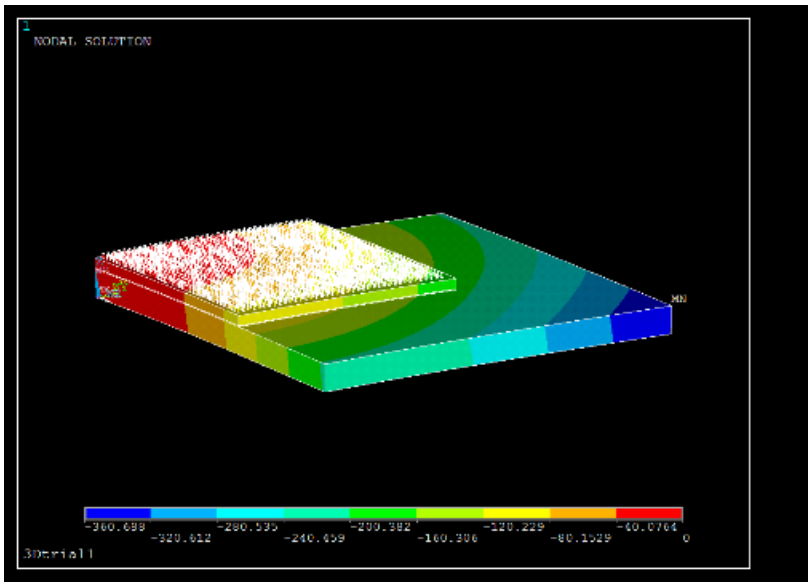

Figure A.5 – Displacement results for FPGA warpage model

REFERENCES

[1] Majumdar, A., 2009, “Helping Chips to Keep Their Cool,” Nature Nanotechnology Journal. Vol. 4, pp. 214.

[2] 2017, “International Roadmap for Devices and Systems,” Institute of Electrical and Electronics Engineers 2017 Edition.

[3] Rupp, K., Horowitz, M., Labonte, F., Shacham, O., Olukotun, K., Hammond, L., and Batten C., 2019, https://www.karlrupp.net/2019/09/42-yearsof-microprocessor-trend-data/

[4] Mahajan, R., Chiu, C., and Chrysler, G., 2006, “Cooling a Microprocessor Chip,” Proceedings of the IEEE, vol. 94, no. 8, pp. 1476-1486.

[5] Zhang, Y., Dembla, A., Joshi, Y., and Bakir, M. S., 2012, "3D Stacked Microfluidic Cooling for High-performance 3D ICs," 2012 IEEE 62nd Electronic Components and Technology Conference, San Diego, CA, pp. 1644-1650.

[6] Madhour, Y., d'Entremont, B.P., Braz Marcinichen, J., Michel, B., Richard, T.J., “Modeling of Two-Phase Evaporative Heat Transfer in Three-Dimensional Multicavity High Performance Microprocessor Chip Stacks.” ASME. Journal of Electronic Packaging. 2014.

[7] Oiu, L., Dubey, S., Choo, H. F., Duan, F., 2015, “Recent Developments of Jet Impingement Nucleate Boiling,” International Journal of Heat and Mass Transfer, Vol. 89, pp. 42-58.

[8] Ditri, J., McNulty, M. K., and Igoe, S., 2014, "Embedded Microfluidic Cooling of High Heat Flux Electronic Components," 2014 Lester Eastman Conference on High Performance Devices (LEC), Ithaca, NY, pp. 1-4.

[9] Chainer, T. J., Schultz, M. D., Parida, P. R., and Gaynes, M. A., 2017, "Improving Data Center Energy Efficiency With Advanced Thermal Management," in IEEE Transactions on Components, Packaging and Manufacturing Technology, vol. 7, no. 8, pp. 1228-1239.

[10] Peles, Y., Kuo, C. J., Koşar, A., Mishra, C., and Schneider, B., 2005, “Forced Convective Heat Transfer Across a Pin Fin Micro Heat Exchanger,” International Journal of Heat and Mass Transfer 0017-9310, 48(17), pp. 3615–3627.

[11] Sarvey, T. E., Zhang, Cheung, C., Gutala, R., Rahman, A., Dasu, A., and Bakir, M.S., 2017, "Monolithic Integration of a Micropin-Fin Heat Sink in a 28-nm FPGA," in IEEE Transactions on Components, Packaging and Manufacturing Technology, vol. 7, no. 10, pp. 1617-1624.

[12] Nasr, M. N., Green, E. C., Kottke, P. A., Zhang, H., Sarvey, T. E., Joshi, Y., Bakir, M. and Fedorov, A., “Flow Regimes and Convective Heat Transfer of Refrigerant Flow Boiling in Ultra-small Clearance Microgaps,” Int. J. Heat Mass Transf., 108, 1702-1713 (2017).

[13] Ostrowicki, G. T. and Sitaraman, S. K., “Cyclic Magnetic Actuation Technique for Thin Film Interfacial Fatigue Crack Propagation,” Engineering Fracture Mechanics, Volume 168, Part A, December 2016, Pages 1–10.

[14] Krieger, W. E. R., Raghavan, S., and Sitaraman, S. K., “Experiments for Obtaining Cohesive-Zone Parameters for Copper-Mold Compound Interfacial Delamination,” IEEE Transactions on Components, Packaging, and Manufacturing Technology, Vol. 6, No. 9, Sep. 2016, pp. 1389-1398.

[15] Raghavan, S., Schmadlak, I., Leal, G., and Sitaraman, S. K., “Mixed-Mode Cohesive Zone Parameters for Sub-Micron Scale Stacked Layers to Predict Microelectronic Device Reliability,” Engineering Fracture Mechanics, Vol. 153, March 2016, pp. 259-277.

[16] Raghavan, S., Schmadlak, I., Leal, G., and Sitaraman, S., “Study of Chip-Package Interaction Parameters on Interlayer Dielectric Crack Propagation,” IEEE Transactions on Device and Materials Reliability, Vol. 14, No. 1, March 2014, pp. 57-65.

[17] Ostrowicki, G. T. and Sitaraman, S. K., “Magnetically Actuated Peel Test for Thin Films,” Thin Solid Films, 520 (2012), pp. 3987–3993.

[18] Ginga, N. and Sitaraman, S. K., “New Method to Measure Tensile Strength of Low Modulus Thin Films,” Letters in Fracture and Micromechanics, International Journal of Fracture, Vol. 170, Issue 2, 2011, pp. 199-206.

[19] Zheng, J. and Sitaraman, S. K., “Fixtureless Superlayer-driven Delamination Test for Nanoscale Thin Film Interfaces,” Thin Solid Films, Volume 515, Issue 11, April 2007, pp. 4709-4716.

[20] Modi, M and Sitaraman, S. K., "Interfacial Fracture Toughness Measurement for Thin Film Interfaces," Engineering Fracture Mechanics, Vol. 71, 2004, pp. 1219-1234.

[21] Xie, W. and Sitaraman, S. K., “Investigation of Interfacial Delamination of a Copper-Epoxy Interface under Monotonic and Cyclic Loading: Experimental Characterization,” IEEE Transactions on Advanced Packaging, Vol. 26, No. 4, Nov. 2003, pp. 447-452.

[22] Doh, I., Cho, Y., "Design and Evaluation for Mechanical Strength of an Anodically Bonded Pressurized Cavity Array for Wafer-Level MEMS Packaging," in Sensors and Materials, 2006, vol. 18, no. 5, pp.231-240.

[23] Petzold, M., Knoll, H., Bagdahn, J., “Strength Assessment of Wafer-bonded Micromechanical Components using the Micro-chevron test”. Proc. SPIE 4558, Reliability, Testing, and Characterization of MEMS/MOEMS, 133 (October 2, 2001); doi:10.1117/12.442994.

[24] Kottke, P. A., Yun, T. M., Green, C., Joshi, Y. K. and Fedorov, A. G., “Two-phase Convective Cooling for Ultra-high Power Dissipation in Microprocessors,” ASME J. Heat Transfer, 138 (1), 011501-011507 (2015).

[25] Green, C., Kottke, P., Han, X., Woodrum, C., Sarvey, T., Asrar, P., Zhang, X., Joshi, Y., Fedorov, A., Sitaraman, S., and Bakir, M., 2015, “A Review of Two-Phase Forced Cooling in Three-Dimensional Stacked Electronics: Technology Integration,” Transactions of the ASME – Journal of Electronic Packaging, Vol. 137, pp. 0408021- 0408029.

[26] Wang, Y., Houshmand, F., Elcock, D., and Peles, Y., 2013, “Convective Heat Transfer and Mixing Enhancement in a Microchannel With a Pillar,” Int. J. Heat Mass Transfer, 62, pp. 553–561.

[27] Krishnamurthy, S., and Peles, Y., 2010, “Flow Boiling Heat Transfer on Micro Pin Fins Entrenched in a Microchannel,” J. Heat Transfer, 132, p. 041007.

[28] Zhang, X., Nasr, M. H., Woodrum, D. C., Green, C. E., Kottke, P. A., Sarvey, T. E., Joshi, Y. K., Sitaraman, S. K., Fedorov, A. G., Bakir, M., 2016, “Design, Microfabrication and Thermal Characterization of the Hotspot Cooler Testbed for Convective Boiling Experiments in Extreme-micro-gap with Integrated Micropin-fins and Great Loss Minimization,” The Intersociety Conference on Thermal and Thermomechanical Phenomena in Electronic Systems, Las Vegas, NV

[29] Han, X., Joshi, Y., and Fedorov, A., 2016, “Flow Boiling of Water at Subatmospheric Pressure in Staggered Micro Pin-fin Heat Sink,” in Proc. 15th IEEE Intersoc. Conf. Thermal Thermomech. Phenomena Electron. Syst. (ITherm), pp. 799–804.

[30] Asrar, P., Zhang, X., Woodrum, C., Green, C. E., Kottke, P. A., Sarvey, T. E., Sitaraman, S. K., Fedorov, A., Bakir, M., and Joshi, Y., 2016, “Flow Boiling of R245fa in a Microgap with Integrated Staggered Pin Fins,” ITHERM 2016 The Intersociety Conference on Thermal and Thermomechanical Phenomena in Electronic Systems, Las Vegas, NV.

[31] Hatty, V., Kahn, H., and Heuer, A.H., "Fracture toughness, fracture strength, and stress corrosion cracking of silicon dioxide thin films," Microelectromechanical Systems, Journal of , vol.17, no.4, pp.943,947, Aug. 2008

[32] Woodrum, D.C., Sarvey, T., Bakir, M.S., Sitaraman, S.K., 2015, "Reliability Study of Micro-pin Fin Array for On-chip Cooling," in Electronic Components and Technology Conference (ECTC) , 2015 IEEE 65th , vol., no., pp.2283-2287, 26-29

[33] Xiangzhao, Ye-Yuming, Sun-Fujiang, Tu-Yunhua, Liusang, "Crack growth analysis of ball grid array resistor's solder joint subjected to thermal cycling and 4 point cycling bending," *Electronic Packaging Technology & High Density Packaging, 2008. ICEPT-HDP 2008. International Conference on* , vol., no., pp.1,4, 28-31 July 2008.

[34] Chiu, C.C., Li, Y.T, Li, H.F., and Wang, C.T., "Fine pitch BGA solder joint split in SMT process," *Microsystems, Packaging, Assembly and Circuits Technology Conference, 2009. IMPACT 2009. 4th International*, vol., no., pp.602,605, 21-23 Oct. 2009.

[35] Woodrum, D. C., Zhang, X., Kottke, P. A., Joshi, Y. K., Fedorov, A. G., Bakir, M. S., and Sitaraman, S. K., "Reliability Assessment of Hydrofoil-Shaped Micro-Pin Fins," ITHERM 2016 The Intersociety Conference on Thermal and Thermomechanical Phenomena in Electronic Systems, May-June 2016, Las Vegas, NV.

[36] Oh, H., May, G. S., Bakir, M.S., 2017, "Heterogeneous Integrated Microsystems with Nontraditional Through-Silicon Via Ttechnologies," IEEE Trans. Compon., Packag. Manuf. Technol., vol. 7, no. 4, pp. 502–510.

[37] Nasr, M. N., Green, E. C., Kottke, P. A., Zhang, H., Sarvey, T. E., Joshi, Y., Bakir, M. and Fedorov, A., "Hotspot thermal management with flow boiling of refrigerant in ultrasmall microgaps," ASME J. Electronic Packaging, 139, 011006-011014 (2017).

[38] Ligrani, P. M., Oliveira, M. M., and Blaskovich, T., "Comparison of Heat Transfer Augmentation Techniques", AIAA Journal, Vol. 41, No. 3 (2003), pp. 337-362.

[39] Peles, Y., "Two-phase boiling flow in microchannels-instabilities issues and flow regime mapping", in: 1st International Conference on Microchannels and Minichannels, ASME, New York, NY, 2003, pp. 559–566.

[40] Bar-Cohen, A., Sheehan, J.R., and Rahim, E., "Two-phase thermal transport in microgap channels—theory, experimental results, and predictive relations," Microgravity Science and Technology vol. 24, no. 1, pp. 1-15, Jan. 2012.

[41] Abbaspour, R., Woodrum, D. C., Kottke, P. A., Sarvey, T. E., Green, C. E., Joshi, Y. K., Fedorov, A. G., Sitaraman, S. K., and Bakir, M. S., "Combined Finned Microgap with Dedicated Extreme-microgap Hotspot Flow for High Performance Thermal Management," ITHERM 2016 The Intersociety Conference on Thermal and Thermomechanical Phenomena in Electronic Systems, May-June 2016, Las Vegas, NV, pp. 1388-1392.